THE JOURNAL OF PHYSICAL CHEMISTRY C

Article

pubs.acs.org/JPCC

Selective Adsorption of Water from Mixtures with 1-Alcohols by Exploitation of Molecular Packing Effects in CuBTC

Juan José Gutiérrez-Sevillano,[†] Sofia Calero,[†] and Rajamani Krishna*[,‡]

[†]Department of Physical, Chemical and Natural Systems, University Pablo de Olavide Ctra., Utrera km. 1, 41013 Sevilla, Spain

[‡]Van't Hoff Institute for Molecular Sciences, University of Amsterdam, Science Park 904, 1098 XH Amsterdam, The Netherlands

Web-Enhanced Feature Supporting Information

ABSTRACT: The selective removal of water from mixtures with methanol, ethanol, and 1-propanol is an important task in the processing industries. With the aid of configurational-bias Monte Carlo simulations of unary and mixture adsorption, we establish the potential of CuBTC for this separation task. For operations close to pore saturation conditions, the adsorption is selective to water that has a significantly higher saturation capacity compared to that of 1-alcohols. The water-selective separation relies on subtle entropy effects that manifest near pore saturation conditions. A further distinguishing feature is that mixture adsorption is determined to be strongly nonideal, and the activity coefficients of the constituent components deviate strongly from unity as pore saturation is approached. The predictions of the ideal adsorbed solution theory (IAST), though qualitatively correct, do not predict the component loadings for mixture adsorption with adequate accuracy. Consequently, the activity coefficients, after appropriate parametrization, have been incorporated into the real adsorbed solution theory (RAST). Transient breakthrough simulations, using the RAST model as a basis, demonstrate the capability of CuBTC for selective adsorption of water in fixed-bed adsorption devices operating under ambient conditions.

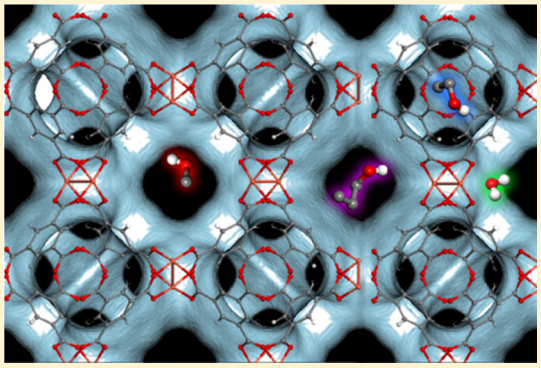

INTRODUCTION

In the processing industries, distillation is the most common technology for separation of mixtures containing water and alcohols.[1,2] The separation task is often rendered difficult because of azeotrope formation. The separation of azeotropic mixtures requires the addition of an additional component to the mixture, called entrainers, that alters the vapor/liquid equilibrium in a favorable manner in order to effect the desired separation in distillation columns. The recovery of the entrainer requires an additional distillation processing step, placing additional energy demands because of vapor/liquid phase transformations in condensers, reboilers, and solvent recovery sections.

Microporous materials such as zeolites, metal−organic frameworks (MOFs), and zeolitic imidazolate frameworks (ZIFs) offer the potential for separation of mixtures of water and alcohols.[3,4] A lot of the research work has been devoted to separation of dilute aqueous streams which require the selective adsorption of the desirable alcohols using hydrophobic adsorbents such as ZIF-8.[5,6] Our focus is on the selective adsorption of water from mixtures containing 1-alcohols. This task is relevant, for example, for separating water/ethanol and water/1-propanol mixtures that have the azeotropic compositions, respectively, of 11%/89% and 57%/43%. Water-selective separations are currently carried out using LTA-3A, LTA-4A, and LTA-5A zeolites; the separation principle is based primarily on the significantly larger diffusivity of water molecules across the narrow windows that are approximately 4 Å in size. Diffusion-selective separation of water/methanol mixtures is also the underlying mechanism for the separations using Ln-MOF with pyrazine-2,5-dicarboxylate ligands as linkers.[7] Uchida and Mizuno[8] report uptake data for water, methanol, and ethanol in zeotype polyoxometalate-macrocation ionic crystal, whose channels are not large enough to allow methanol and ethanol to enter. While diffusion-selective separations can be exploited in membrane constructs, its use in fixed-bed adsorbers results in distended breakthrough characteristics with attendant lowering in the productivity.[9] For these reasons, we direct our attention at water-stable, hydrophilic, MOF adsorbents with "open structures" that are suitable for use in fixed-bed units.

The novelty of the current investigation resides in the exploitation of the differences in the saturation capacities of water and 1-alcohols. Exploitation of differences in saturation capacities would necessarily require operation under conditions such that the pores of the adsorbent material are saturated; under such conditions, the separations of mixtures are dictated by molecular packing effects which are expected to favor the smaller water molecules.[10]

For mixtures of 1-alcohols, the adsorption of the smaller alcohol can be achieved at high selectivity by operating at pore

Received: December 24, 2014
Revised: January 27, 2015
Published: January 30, 2015

DOI: 10.1021/jp512853w
J. Phys. Chem. C 2015, 119, 3658−3666

saturation conditions in CHA,[11] SAPO-34,[12] ZIF-8,[5,6] and ZIF-68.[13] The molecular simulation data for water/methanol and water/ethanol mixtures in ZIF-71 indicate that water can be selectively adsorbed near pore saturation conditions.[14] However, subsequent experimental investigations[5,15] do not support the results anticipated from molecular simulations. In particular, the uptake of water is significantly lower than that of the alcohols, suggesting that ZIF-71 has hydrophobic characteristics similar to ZIF-8 and ZIF-68.[5]

In this work, we choose CuBTC (=$Cu_3(BTC)_2$ with BTC = 1,3,5-benzenetricarboxylate, also known as HKUST-1) as adsorbent primarily because of its high affinity for water.[16,17] The primary objective of our article is to demonstrate the significant potential of CuBTC for selective adsorption of water from mixtures containing methanol, ethanol, and 1-propanol. We use configurational-bias Monte Carlo (CBMC) simulations to generate the required information on unary and mixture isotherms in order to quantify their separation capability.

2. CBMC SIMULATION METHODOLOGY

The CuBTC framework is composed of copper atoms connected by BTC linkers, which form a characteristic paddle-wheel structure: two copper atoms bonded to the oxygen atoms of four BTC linkers. The framework consists of two types of large 9 Å cavities (L_2 and L_3) and small 5 Å tetrahedral pockets (T_1) (see Figure 1). The larger cavities (L_2 and L_3) are similar in size and

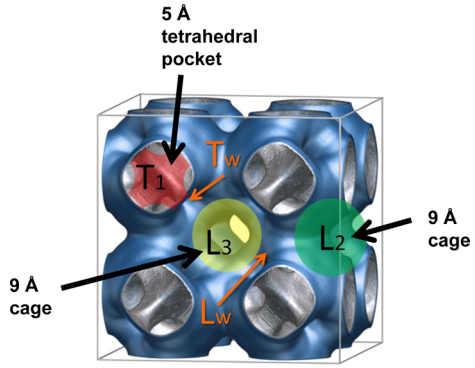

Figure 1. Pore landscape and cage connectivity of the CuBTC framework.

shape, but as a result of the paddle-wheel, the copper atoms are only accessible from the L_3 cages. L_2 and L_3 cavities are connected by windows. The small cavities (T_1) are tetrahedral pockets enclosed by the benzene rings. They are connected to L_3 cages by 4.6 Å triangular windows.

Water is modeled using TIP5P-E[18] which has proven to be the most suitable model for water in Cu-BTC.[19] Furthermore, recently, Peng et al.[20] have found that at least a four-site model is needed to reproduce the right orientation of the water molecules in metal organic frameworks containing open metal sites. The alcohol molecules are modeled using TraPPE.[21] The Cu-BTC framework is modeled as a rigid structure based on the crystal structure of Chui et al.[22] with the atoms fixed in their crystallographic position. We removed the axial oxygen atoms weakly bonded to the copper atoms that correspond to water ligands. Lenard-Jones parameters for the atoms were taken from the DREIDING[23] force field except those for copper atoms that were taken from the UFF[24] force field (see Table S2, Supporting Information). Additionally, partial charges obtained from

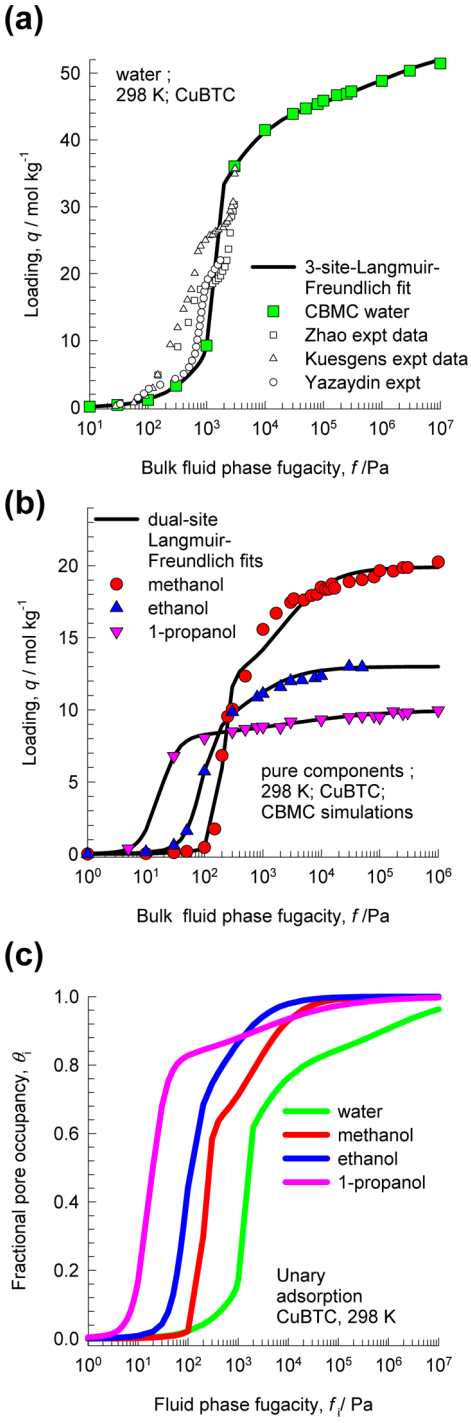

Figure 2. (a) Comparison of the CBMC simulations of water isotherm with experimental data.[16,28,29] (b) CBMC simulated isotherms for 1-alcohols. (c) The fractional occupancy within the pores, θ_i, for each of the four guest molecules as a function of the bulk fluid phase fugacity, f_i.

Castillo et al.[19] were added to the model. The unit cell of our model is a cubic cell of $a = b = c = 26.34$ Å. The computed void fraction is 0.76, the pore volume 0.85 cm^3/g, and the surface area 2100 m^2/g. The framework density is $\rho = 879$ kg m^{-3}.

Monte Carlo (MC) simulations were performed in the grand canonical (GC) ensemble, and the configurational bias Monte Carlo (CBMC) technique was used for the insertion and deletion of molecules in and from the system. We employed Lennard-Jones and electrostatic cutoffs at 12.0 Å. Coulombic interactions

DOI: 10.1021/jp512853w
J. Phys. Chem. C 2015, 119, 3658−3666

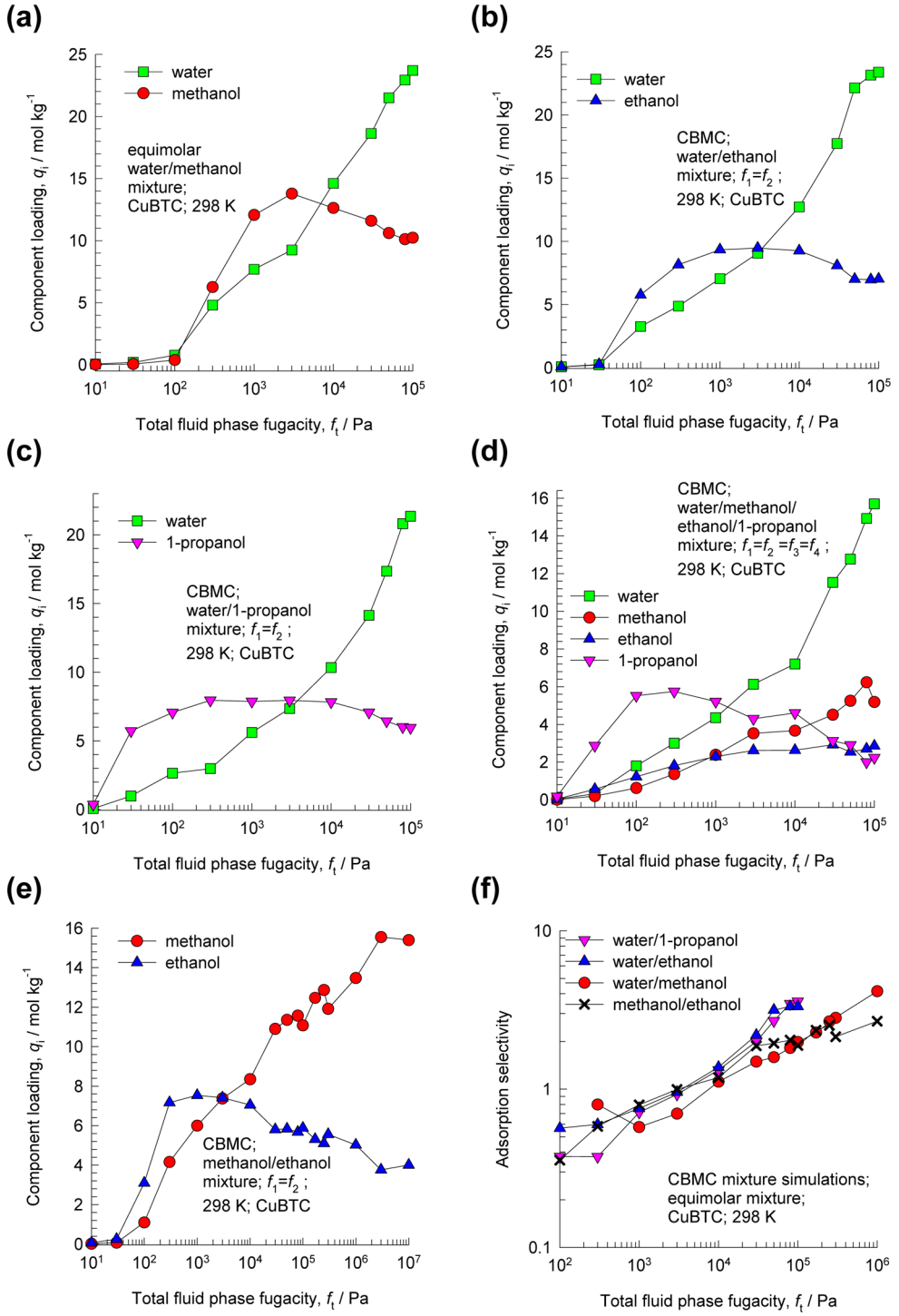

Figure 3. CBMC simulations for equimolar (a) water/methanol, (b) water/ethanol, (c) water/1-propanol, (d) water/methanol/ethanol/1-propanol, and (e) methanol/ethanol mixtures in CuBTC at 298 K. (f) Comparison of adsorption selectivities for binary mixtures.

were computed using the Ewald summation technique with a relative precision of 10^{-6}. The code and most of the force fields and models used in this work have been extensively tested and validated with a large number of experimental and simulation data.[25−27]

3. UNARY ISOTHERMS

The water isotherm shows marked inflections (see Figure 2a). The origin of these inflections can be traced to the location of water molecules within the tetrahedral pockets (about nine molecules can be accommodated in T_1) and within the larger cages (L_2 and L_3). The three-site Langmuir−Freundlich model is used to properly capture the inflections

$$q^0 = q_{A,sat}\frac{b_A f^{\nu_A}}{1 + b_A f^{\nu_A}} + q_{B,sat}\frac{b_B f^{\nu_B}}{1 + b_B f^{\nu_B}} + q_{c,sat}\frac{b_C f^{\nu_C}}{1 + b_C f^{\nu_C}} \quad (1)$$

The CBMC simulations are in reasonable agreement with published experimental data.[16,28,29] The steep portion of the

DOI: 10.1021/jp512853w
J. Phys. Chem. C 2015, 119, 3658−3666

water isotherm is correctly reproduced; this corresponds to the occupation of the larger cages of CuBTC.

The unary isotherms for methanol, ethanol, and 1-propanol are adequately described using the dual-Langmuir–Freundlich model (see Figure 2b). Particularly noteworthy are the differences in the saturation capacities of the various guest molecules: water = 54 mol kg^{-1}; methanol = 19.9 mol kg^{-1}; ethanol = 13 mol kg^{-1}; 1-propanol = 10 mol kg^{-1}. The experimental data of van Assche et al.[17] for unary isotherms of water and alcohols in CuBTC at 323 K indicate a similar hierarchy of saturation capacities.

Let us define the fractional pore occupancy within the pores, θ_i, for each of the four guest molecules

$$\theta_i = q^0/q_{sat} \tag{2}$$

where q^0 is the molar loading of species i that is determined from the Langmuir–Freundlich fits. The variation of the pore occupancies with bulk fluid phase fugacity, f_i, is shown in Figure 2c. We note that the pore occupancies are close to unity for operation at ambient conditions of 100 kPa and 298 K. The "driver" for mixture separations is the large differences in saturation capacities of water and partner 1-alcohols. It needs to be stressed that the interactions of the guest molecules with the unsaturated Cu atoms is not relevant to the achieved separations at pore saturation.

4. MIXTURE ADSORPTION AND NONIDEALITIES

Figure 3, panels a, b, c, d, and e, presents the CBMC data for adsorption of (a) water/methanol, (b) water/ethanol, (c) water/1-propanol, (d) water/methanol/ethanol/1-propanol, and (e) methanol/ethanol mixtures in CuBTC. In all five cases, we note a reversal in the hierarchy of component loadings as conditions approach pore saturation. For binary mixtures, adsorption selectivities are shown in Figure 3f. For water/1-alcohol mixtures, the selectivity is in favor of water at conditions close to 100 kPa (see Figure 3f). For methanol/ethanol mixtures, the adsorption is in favor of the shorter alcohol at $f_t = f_1 + f_2 > 10$ kPa; the preferential adsorption of shorter 1-alcohols has been observed also for CHA,[11] SAPO-34,[12] ZIF-8,[5,6] and ZIF-68.[13]

We now examine whether the ideal adsorbed solution theory (IAST) of Myers and Prausnitz[30] provides a quantitative representation of mixture adsorption. Briefly, the IAST is the analogue of Raoult's law for vapor–liquid equilibrium, i.e.

$$f_i = P_i^0 x_i; \qquad i = 1, 2, \ldots, n \tag{3}$$

where x_i is the mole fraction in the adsorbed phase

$$x_i = q_i/(q_1 + q_2 + \ldots q_n) \tag{4}$$

and P_i^0 is the pressure for sorption of every component i, which yields the same spreading pressure, π, for each of the pure components, as that for the mixture

$$\frac{\pi A}{RT} = \int_0^{P_1^0} \frac{q_1^0(f)}{f} df = \int_0^{P_2^0} \frac{q_2^0(f)}{f} df = \int_0^{P_3^0} \frac{q_3^0(f)}{f} df \tag{5}$$

where $q_i^0(f)$ is the *pure* component adsorption isotherm described by the Langmuir–Freundlich fit (eq 1). The units of the spreading pressure π are the same as that for surface tension, i.e., N m^{-1}; indeed the spreading pressure is the negative of the surface tension.[30] The quantity A is the surface area per kilogram of framework, with units of m^2 kg^{-1}; the units of $(\pi A/RT)$ are mol kg^{-1}. The values of P_1^0, P_2^0, and P_3^0 that satisfy each of the equalities in eq 5 can be determined using suitable numerical techniques. The adsorbed phase mole fractions x_i are then determined from

$$x_i = f_i/P_i^0; \qquad i = 1, 2, \ldots, n \tag{6}$$

The total amount adsorbed can be calculated

$$q_t \equiv q_1 + q_2 \ldots + q_n = \frac{1}{\frac{x_1}{q_1(P_1^0)} + \frac{x_2}{q_2(P_2^0)} + \ldots + \frac{x_n}{q_n(P_n^0)}} \tag{7}$$

Figure 4a compares the IAST calculations with CBMC data for water/methanol mixtures. The agreement between IAST and

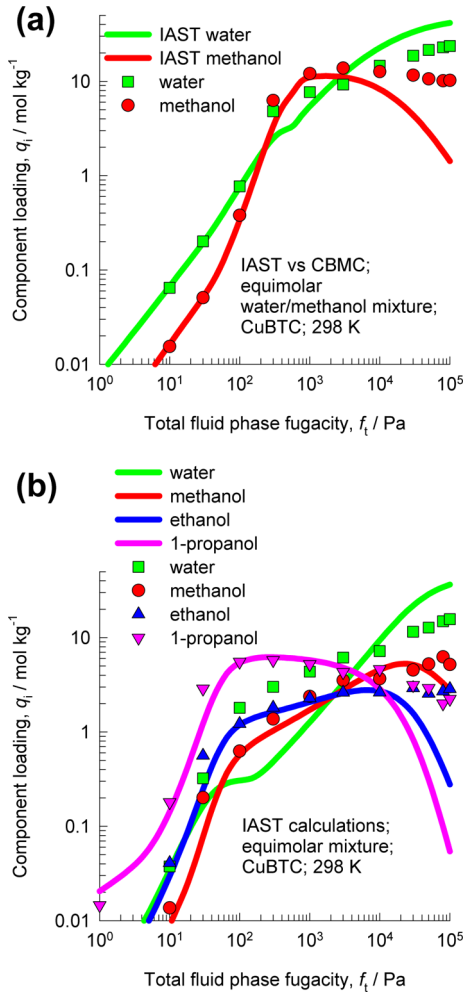

Figure 4. Comparison of CBMC simulations for (a) water/methanol and (b) water/methanol/ethanol/1-propanol mixtures with IAST predictions of component loadings.

CBMC is excellent for $f_t < 50$ Pa; this should be expected in the Henry regime of adsorption. For $f_t > 50$ Pa, there are significant quantitative departures between CBMC and IAST predictions. The reasons for the deviations can be attributed to the influence of hydrogen bonding between water and methanol and consequent clustering, as explained in earlier work.[31]

For water/methanol/ethanol/1-propanol mixtures, the hierarchy of component loadings near pore saturation is correctly anticipated by the IAST, but the quantitative agreement is poor (see Figure 4b). The inadequacy of IAST to accurately predict

DOI: 10.1021/jp512853w
J. Phys. Chem. C 2015, 119, 3658–3666

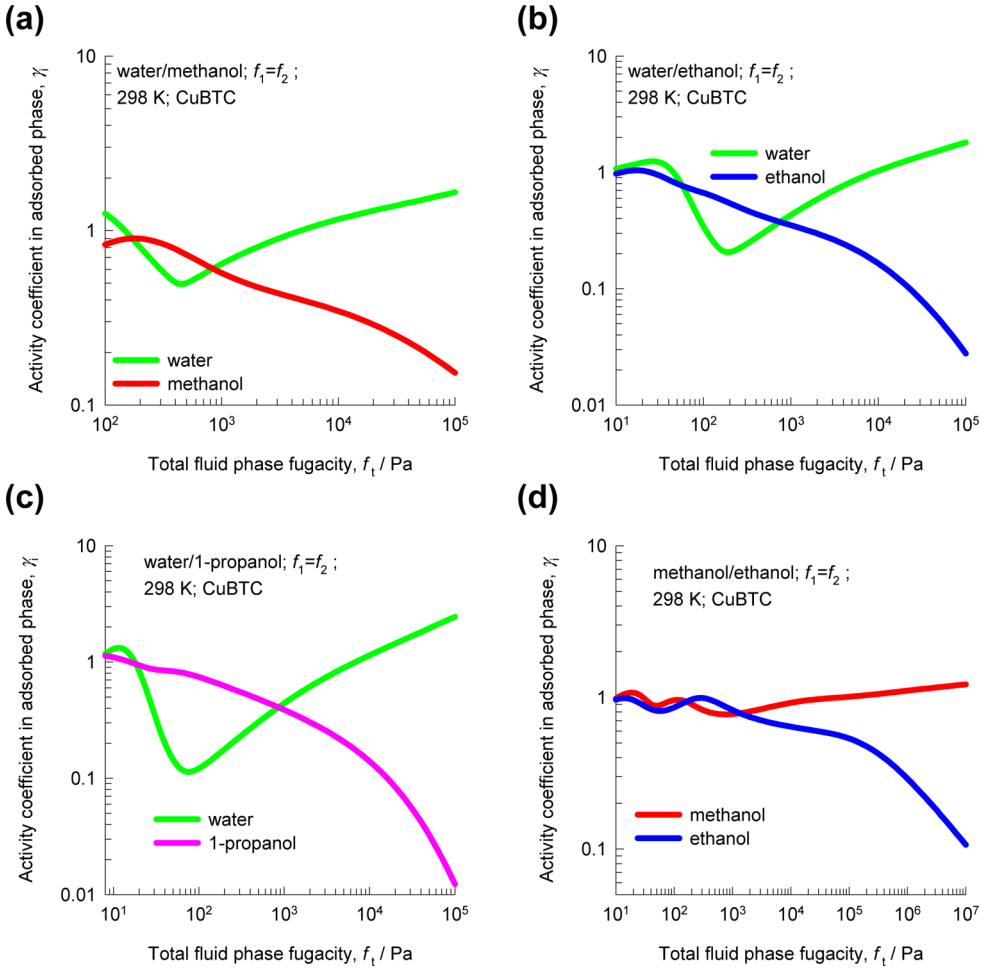

Figure 5. Activity coefficients of the components in the adsorbed phase for equimolar (a) water/methanol, (b) water/ethanol, (c) water/1-propanol, and (d) methanol/ethanol mixtures in CuBTC at 298 K.

the component loadings near pore saturation conditions holds for the other investigated mixtures (see Figures S9 and S10, Supporting Information).

For further analysis, we follow the approach of Myers and Prausnitz[30] and account for nonidealities by introducing activity coefficients γ_i into eq 3

$$f_i = P_i^0 x_i \gamma_i \tag{8}$$

The CBMC mixture simulations provide information on the mole fractions of the adsorbed phase, x_i, but the activity coefficients γ_i are not known *a priori*; these need to be backed out from the CBMC data. Using the Gibbs adsorption equation for mixture adsorption as starting point (cf. equation 3.52 of Ruthven[32]), we can write the differential of the spreading pressure as follows

$$\frac{Ad\pi}{RT} = q_1 d\ln f_1 + q_2 d\ln f_2 \tag{9}$$

Integrating eq 9 from 0 to f_1 and f_2

$$\frac{\pi A}{RT} = \int_0^{f_1, f_2} (q_1 \mathrm{d}\ln f_1 + q_2 \mathrm{d}\ln f_2) = \int_0^{f_t} (q_1 + q_2)\mathrm{d}\ln f_t \tag{10}$$

The integral in eq 10 can be determined using an appropriate quadrature formula. The approach we use here is to fit the water loadings q_1 and the total mixture loading $q_t = q_1 + q_2$ as functions, respectively, of the partial fugacities, f_1, and total mixture fugacity f_t. The P_i^0 can be determined for each of the two components by setting the equalities

$$\frac{\pi A}{RT} = \int_0^{f_t} (q_1 + q_2)\mathrm{d}\ln f_t = \int_0^{P_1^0} \frac{q_1^0(f)}{f}\mathrm{d}f = \int_0^{P_2^0} \frac{q_2^0(f)}{f}\mathrm{d}f \tag{11}$$

Equation 11 can be solved to determine P_1^0 and P_2^0 as a function of the total mixture fugacity f_t. Combining the obtained values of P_1^0 and P_2^0 with eq 8, we can determine the activity coefficients γ_i as a function of the total mixture fugacity f_t. The fitting procedure for CBMC mixture simulation data, along with a detailed step-by-step methodology for calculation of the activity coefficients, is provided in the Supporting Information.

Figure 5, panels a, b, c, and d, presents data on the activity coefficients γ_i for equimolar (a) water/methanol, (b) water/ethanol, (c) water/1-propanol, and (d) methanol/ethanol mixtures calculated in the manner detailed above. For water/methanol mixtures, we note that at a total bulk fluid phase fugacity $f_t = f_1 + f_2 < 200$ Pa the activity coefficients of each component are approximately unity. The small departures from unity at low pressures are a consequence of the numerical fitting procedure employed in the calculations of the activity coefficients; the fundamentally correct limiting value of the activity coefficient $\gamma_i \to 1$; $f_t \to 0$ cannot be prescribed in the adopted methodology. With increasing values of f_t, the activity coefficient

DOI: 10.1021/jp512853w
J. Phys. Chem. C 2015, 119, 3658−3666

of water increases, whereas that of methanol decreases. For water/ethanol and water/1-propanol mixtures, similar trends are observed, but the threshold values are lower, about 10 Pa in each case. For methanol/ethanol mixtures, the activity coefficients deviate significantly from unity only for $f_t = f_1 + f_2 > 10$ kPa. From the results presented in Figure 5, it appears that nonidealities are much more significant for water/alcohol mixtures than for methanol/ethanol mixtures. These deviations are most likely correlated with the hydrogen bonding effects that are stronger between water and alcohol molecules than between pairs of alcohol molecules; a quantitative justification is provided in our earlier work.[31]

The analysis of CBMC mixture simulation data for water/alcohol mixtures in FAU and DDR zeolites yield activity coefficients whose characteristics are quite similar to those witnessed in Figure 5; see Supporting Information for details.

Following the work of Calleja et al.[33] we use the Wilson model to describe the variation of the activity coefficients with the composition of the adsorbed mixtures

$$\ln(\gamma_1) = 1 - \ln(x_1 + x_2\Lambda_{12}) - \frac{x_1}{x_1 + x_2\Lambda_{12}} - \frac{x_2\Lambda_{21}}{x_2 + x_1\Lambda_{21}}$$

$$\ln(\gamma_2) = 1 - \ln(x_2 + x_1\Lambda_{21}) - \frac{x_2}{x_2 + x_1\Lambda_{21}} - \frac{x_1\Lambda_{12}}{x_1 + x_2\Lambda_{12}} \quad (12)$$

The choice of $\Lambda_{12} = \Lambda_{21} = 1$ in eq 12 reduces eq 8 to eq 3. The parameters Λ_{12} and Λ_{21} can be fitted to match the CBMC mixture simulations; Table S10 (Supporting Information) lists the Wilson parameters Λ_{12} and Λ_{21}. With this parametrization of the activity coefficients γ_i, the resulting real adsorbed solution theory (RAST) provides an adequate representation of the mixture adsorption characteristics under conditions near pore saturation (see Figures 6a and 6b for water/methanol and methanol/ethanol mixtures).

An important shortcoming of the RAST implementation of Calleja et al.[33] is that the correct limiting behavior of activity coefficients $\gamma_i \to 1; f_t \to 0$ is not prescribed. Consequently, RAST predictions of mixture adsorption are not accurate in the limit of low fugacities. One approach to redress this problem is to adopt the strategy suggested by Talu and Myers[34,35] and Siperstein and Myers.[36] Essentially, their strategy involves introducing the correction factor $(1 - \exp(-C\pi A/RT))$ into the right members of eq 12; this correction is dependent on the spreading pressure. The constant C, with the units kg mol^{-1}, needs to be determined from measured experimental data using the procedure described in Siperstein and Myers.[36] As pore saturation conditions are approached, this correction factor tends to unity, i.e., $(1 - \exp(-C\pi A/RT)) \to 1$; calculations to demonstrate this are provided in the Supporting Information. Since our primary focus is on separations under pore saturation conditions, we have not implemented this correction factor in the calculations reported in this article.

5. TRANSIENT BREAKTHROUGH SIMULATIONS

Fixed beds, packed with microporous adsorbent materials, are commonly operated in a transient mode. The compositions of the bulk fluid phase and component loadings within the crystals vary with both position and time. During the initial stages of the transience, the pores are loaded up gradually, and only toward the end of the adsorption cycle are conditions corresponding to pore saturation achieved. Consequently, separations in fixed-bed adsorbers are influenced by both the Henry regime of adsorption as well as the conditions corresponding to pore saturation. Separations in fixed-bed adsorbers reflect the "integral" of the component loading for the entire range of fugacities 0–f_t.[9] The foregoing arguments lead us to conclude that in order to properly demonstrate the potential of CuBTC to selectively adsorb water we cannot rely solely on RAST calculations. We therefore carried out transient breakthrough simulations using the methodology described in our earlier works;[9,10] the salient details are provided in the Supporting Information. For presenting the breakthrough simulation results, we use the dimensionless time $(\tau = tu/(L\varepsilon))$, obtained by dividing the actual time, t, by the characteristic time $(L\varepsilon/u)$, where L is the length of adsorber, u the superficial fluid velocity, and ε the bed voidage. For all the simulations reported in this article we choose $L = 0.3$ m, $u = 0.04$ m s^{-1}, and $\varepsilon = 0.4$.

Figure 7, panels a, b, c, and d, presents data on transient breakthroughs in a fixed-bed adsorber packed with CuBTC and fed with equimolar (a) water/methanol, (b) water/ethanol, (c) water/1-propanol, and (d) water/methanol/ethanol/1-propanol mixtures at f_t = 100 kPa and 298 K. In order to gain a proper appreciation of the transient nature of breakthroughs, video animations showing the time progression of the fluid-phase concentrations along the length of the adsorber are available as Web Enhanced Objects in the HTML version of the paper (see movie 1, movie 2, movie 3, movie 4, and movie 5). In all cases,

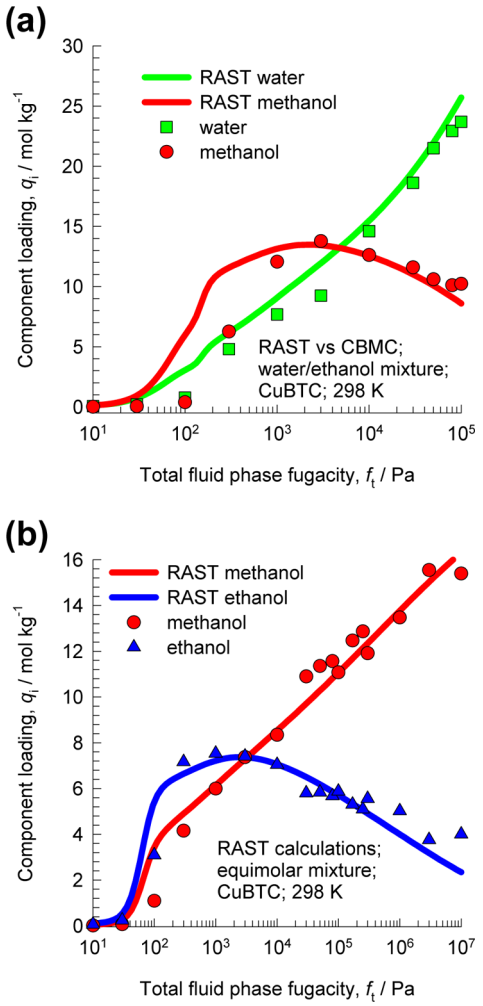

Figure 6. Comparison of CBMC simulations for equimolar (a) water/methanol and (b) methanol/ethanol mixtures in CuBTC at 298 K with RAST calculations.

DOI: 10.1021/jp512853w
J. Phys. Chem. C 2015, 119, 3658−3666

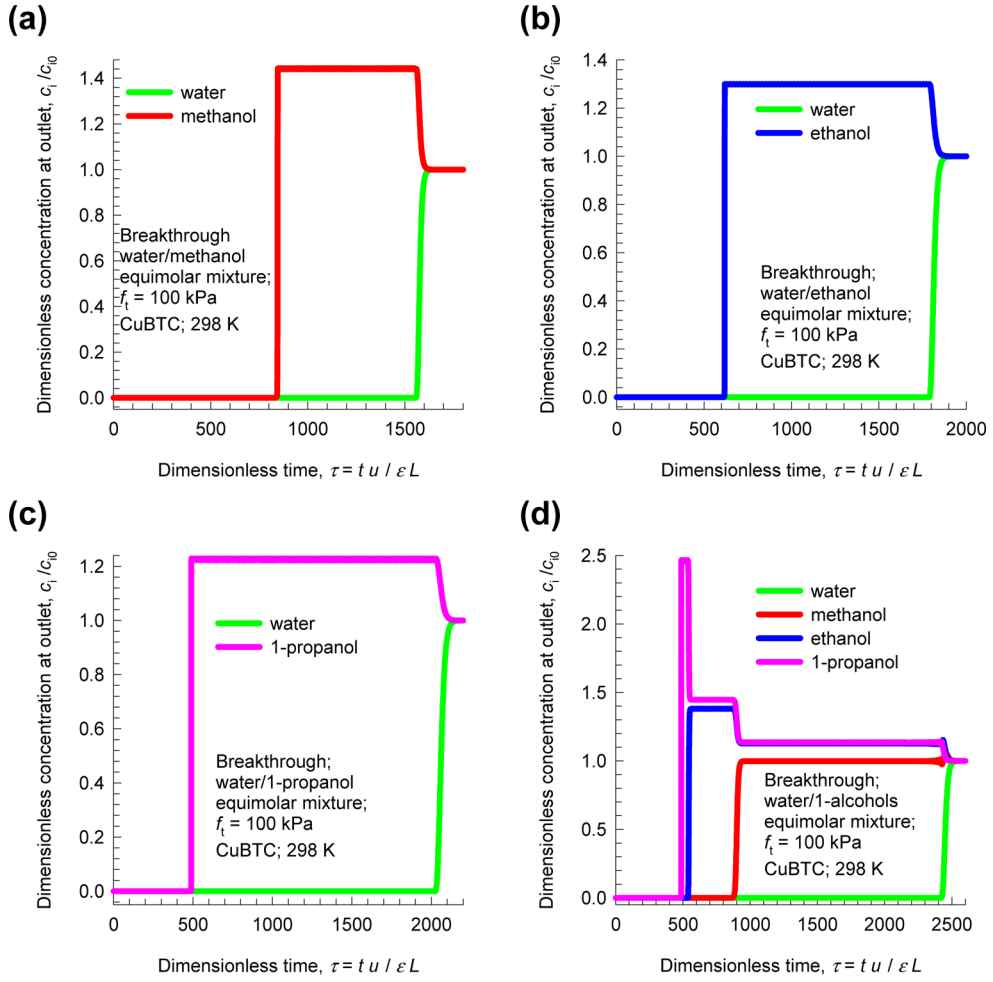

Figure 7. Transient breakthroughs in fixed-bed adsorber packed with CuBTC and fed with equimolar (a) water/methanol, (b) water/ethanol, (c) water/1-propanol, and (d) water/methanol/ethanol/1-propanol mixture at f_t = 100 kPa and 298 K. The *y*-axis represents the concentrations of each component in the exiting fluid phase, normalized with respect to the concentrations in the inlet feed stream.

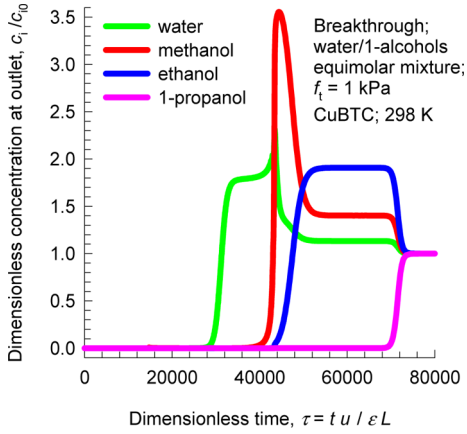

Figure 8. Transient breakthroughs for a four-component mixture in a fixed bed of equimolar water/methanol/ethanol/1-propanol mixture at f_t = 1 kPa and 298 K. These simulations use IAST for adsorption equilibrium.

water elutes the adsorber at the end of the cycle, and the partner alcohol species are rejected into the bulk fluid phase during the early stages of the transience. For the four-component mixture, the elution sequence is 1-propanol, ethanol, methanol, and water that follows the increasing hierarchy of saturation capacities. For this 4-component mixture, simulations using f_t = 1 kPa yield the sequence of breakthroughs, water, methanol, ethanol, and 1-propanol, that follows the hierarchy of adsorption strengths in the Henry regime (see Figure 8). This provides a clear demonstration of the potency of molecular packing effects to reverse the elution hierarchy with increasing pore occupancy.

6. CONCLUSIONS

The following major conclusions emerge from our investigations.

(1) Adsorption separations of mixtures at conditions close to pore saturation are significantly influenced by differences in saturation capacities. The saturation capacities are a direct reflection of the efficiencies by which molecules pack within the microporous channels. Higher packing efficiencies are obtained with smaller molecules.

(2) The CBMC mixture simulations underscore the limitations of the IAST to provide quantitative estimations of the component loadings. Activity coefficients need to be explicitly accounted for, and the RAST affords a pragmatic and practical approach to quantify mixture adsorption.

(3) Selective adsorption of water from water/alcohol mixtures can be achieved with CuBTC by choosing conditions close to pore saturation. Our data indicate that operating at ambient pressure and temperature conditions assures pore saturation.

DOI: 10.1021/jp512853w
J. Phys. Chem. C 2015, 119, 3658−3666

(4) For mixtures of 1-alcohols, molecular packing effects can be exploited in CuBTC to selectively adsorb the shorter alcohol.

In view of the promising results obtained on the basis of molecular simulations, breakthrough experiments need to be performed to confirm the potential of CuBTC use in practice.

■ ASSOCIATED CONTENT

Supporting Information

This material provides (a) structural details of CuBTC, (b) configurational-bias Monte Carlo (CBMC) simulation methodology with specification of force fields, (c) snapshots showing the location of adsorbed molecules within the CuBTC framework, (d) 2-site and 3-site Langmuir–Freundlich fit parameters for unary isotherms, (e) details of the methodology used to calculate activity coefficients from CBMC mixture simulations, (f) details of IAST and RAST calculation procedures, and (g) simulation methodology for transient breakthroughs. This material is available free of charge via the Internet at http://pubs.acs.org.

Web-Enhanced Features

Video animations of the breakthroughs for five difference mixtures containing water and alcohols are available in the HTML version of this paper.

■ AUTHOR INFORMATION

Corresponding Author

*E-mail: r.krishna@contact.uva.nl.

Notes

The authors declare no competing financial interest.

■ NOTATION

A surface area per kg of framework, $m^2\ kg^{-1}$
b_A Langmuir–Freundlich constant for adsorption site A, $Pa^{-\nu_A}$
b_B Langmuir–Freundlich constant for adsorption site B, $Pa^{-\nu_B}$
b_C Langmuir–Freundlich constant for adsorption site C, $Pa^{-\nu_C}$
C constant used in the correction factor, $kg\ mol^{-1}$
c_i molar concentration of species i in gas mixture, $mol\ m^{-3}$
c_{i0} molar concentration of species i in gas mixture at inlet to adsorber, $mol\ m^{-3}$
f_i partial fugacity of species i, Pa
f_t total fugacity of bulk fluid mixture, Pa
L length of packed bed adsorber, m
n number of species in the mixture, dimensionless
P_i^0 sorption pressure, Pa
q^0 pure component loading, $mol\ kg^{-1}$
q_i component molar loading of species i, $mol\ kg^{-1}$
q_t total molar loading for mixture adsorption, $mol\ kg^{-1}$
$q_{i,sat}$ molar loading of species i at saturation, $mol\ kg^{-1}$
R gas constant, 8.314 $J\ mol^{-1}\ K^{-1}$
t time, s
T absolute temperature, K
u superficial gas velocity in packed bed, $m\ s^{-1}$
v interstitial gas velocity in packed bed, $m\ s^{-1}$

Greek Letters

ε voidage of packed bed, dimensionless
γ_i activity coefficient of component i in adsorbed phase, dimensionless
ν exponent in multisite-Langmuir–Freundlich isotherm, dimensionless
π spreading pressure, $N\ m^{-1}$
Λ_{ij} Wilson parameters defined by eq 12, dimensionless
τ time, dimensionless

Subscripts

i referring to component i
t referring to total mixture

■ REFERENCES

(1) Doherty, M. F.; Malone, M. F. *Conceptual Design of Distillation Systems*; McGraw-Hill: New York, 2001.

(2) Taylor, R.; Krishna, R.; Kooijman, H. Real-World Modeling of Distillation. *Chem. Eng. Prog.* **2003**, *99* (7), 28–39.

(3) Jeong, J.-S.; Jeon, H.; Ko, K.-M.; Chung, B.; Choi, G.-W. Production of Anhydrous Ethanol using various PSA (Pressure Swing Adsorption) Processes in Pilot Plant. *Renewable Energy* **2012**, *42*, 41–45.

(4) Kumar, S.; Singh, N.; Prasad, R. Anhydrous Ethanol: A Renewable Source of Energy. *Renewable Sustainable Energy Rev.* **2010**, *14*, 1830–1834.

(5) Zhang, K.; Lively, R. P.; Dose, M. E.; Brown, A. J.; Zhang, C.; Chung, J.; Nair, S.; Koros, W. J.; Chance, R. R. Alcohol and Water Adsorption in Zeolitic Imidazolate Frameworks. *Chem. Commun.* **2013**, *49*, 3245–3247.

(6) Saint-Remi, J. C.; Rémy, T.; van Huskeren, V.; van de Perre, S.; Duerinck, T.; Maes, M.; De Vos, D. E.; Gobechiya, E.; Kirschhock, C. E. A.; Baron, G. V.; Denayer, J. F. M. Biobutanol Separation with the Metal–Organic Framework ZIF-8. *ChemSusChem* **2011**, *4*, 1074–1077.

(7) Plessius, R.; Kromhout, R.; Ramos, A. L. D.; Ferbinteanu, M.; Mittelmeijer-Hazeleger, M. C.; Krishna, R.; Rothenberg, G.; Tanase, S. Highly Selective Water Adsorption in a Lanthanum Metal-Organic Framework. *Chem.—Eur. J.* **2014**, *20*, 7922–7925.

(8) Uchida, S.; Mizuno, N. Zeotype Ionic Crystal of $Cs_5[Cr_3O(OOCH)_6(H_2O)_3][\alpha\text{-}CoW_{12}O_{40}]\text{-}7.5H_2O$ with Shape-Selective Adsorption of Water. *J. Am. Chem. Soc.* **2004**, *126*, 1602–1603.

(9) Krishna, R. The Maxwell-Stefan Description of Mixture Diffusion in Nanoporous Crystalline Materials. *Microporous Mesoporous Mater.* **2014**, *185*, 30–50.

(10) Krishna, R. Separating Mixtures by Exploiting Molecular Packing Effects in Microporous Materials. *Phys. Chem. Chem. Phys.* **2015**, *17*, 39–59.

(11) Krishna, R.; van Baten, J. M. Entropy-based Separation of Linear Chain Molecules by Exploiting Differences in the Saturation Capacities in Cage-type Zeolites. *Sep. Purif. Technol.* **2011**, *76*, 325–330.

(12) Remy, T.; Saint-Remi, J. C.; Singh, R.; Webley, P. A.; Baron, G. V.; Denayer, J. F. M. Adsorption and Separation of C1-C8 Alcohols on SAPO-34. *J. Phys. Chem. C* **2011**, *115*, 8117–8125.

(13) Van der Perre, S.; Van Assche, T.; Bozbiyik, B.; Lannoeye, J.; De Vos, D. E.; Baron, G. V.; Denayer, J. F. M. Adsorptive Characterization of the ZIF-68 Metal-Organic Framework: A Complex Structure with Amphiphilic Properties. *Langmuir* **2014**, *30*, 8416–8424.

(14) Nalaparaju, A.; Zhao, X. S.; Jiang, J. W. Molecular Understanding for the Adsorption of Water and Alcohols in Hydrophilic and Hydrophobic Zeolitic Metal-Organic Frameworks. *J. Phys. Chem. C* **2010**, *114*, 11542–11550.

(15) Lively, R. P.; Dose, M. E.; Thompson, J. A.; McCool, B. A.; Chance, R. R.; Koros, W. J. Ethanol and Water Adsorption in Methanol-derived ZIF-71. *Chem. Commun.* **2011**, *47*, 8667–8669.

(16) Küsgens, P.; Rose, M.; Senkovska, I.; Fröde, H.; Henschel, A.; Siegle, S. Characterization of Metal-Organic Frameworks by Water Adsorption. *Microporous Mesoporous Mater.* **2009**, *120*, 325–330.

(17) Van Assche, T. R. C.; Duerinck, T.; Gutiérrez Sevillano, J. J.; Calero, S.; Baron, G. V.; Denayer, J. F. M. High Adsorption Capacities and Two-Step Adsorption of Polar Adsorbates on Copper- Benzene-1,3,5-tricarboxylate Metal-Organic Framework. *J. Phys. Chem. C* **2013**, *117*, 18100–18111.

(18) Rick, S. W. A Reoptimization of the Five-site Water Potential (TIP5P) for use with Ewald Sums. *J. Chem. Phys.* **2004**, *120*, 6085–6093.

(19) Castillo, J. M.; Vlugt, T. J. H.; Calero, S. Understanding Water Adsorption in Cu-BTC Metal-Organic Frameworks. *J. Phys. Chem. C* **2008**, *112*, 15934–15939.

DOI: 10.1021/jp512853w
J. Phys. Chem. C 2015, 119, 3658–3666

(20) Peng, X.; Lin, L.-C.; Sun, W.; Smit, B. Water Adsorption in Metal−Organic Frameworks with Open-Metal Sites. *AIChE J.* **2015**, *61*, 677−687.
(21) Chen, B.; Potoff, J. J.; Siepmann, J. I. Monte Carlo Calculations for Alcohols and Their Mixtures with Alkanes. Transferable Potentials for Phase Equilibria. 5. United-Atom Description of Primary, Secondary, and Tertiary Alcohols. *J. Phys. Chem. B* **2001**, *105*, 3093−3104.
(22) Chui, S. S. Y.; Lo, S. M. F.; Charmant, J. P. H.; Orpen, A. G.; Williams, I. D. A Chemically Functionalizable Nanoporous Material $[Cu_3(TMA)_2(H2O)_3]_n$. *Science* **1999**, *283*, 1148−1150.
(23) Mayo, S. L.; Olafson, B. D.; Goddard, W. A. DREIDING: A Generic Force Field for Molecular Simulations. *J. Phys. Chem.* **1990**, *94*, 8897−8909.
(24) Rappé, A. K.; Casewit, C. J.; Colwel, K. S.; Goddard, W. A.; Skiff, W. M. UFF, A Full Periodic Table Force Field for Molecular Mechanics and Molecular Dynamics Simulations. *J. Am. Chem. Soc.* **1992**, *114*, 10024−10035.
(25) Gutierrez-Sevillano, J. J.; Dubbeldam, D.; Bellarosa, L.; Lopez, N.; Liu, X.; Calero, S. Strategies to Simultaneously Enhance the Hydrostability and the Alcohol-Water Separation Behavior of Cu-BTC. *J. Phys. Chem. C* **2013**, *117*, 20706−20714.
(26) Gutierrez-Sevillano, J. J.; Vincent-Luna, J. M.; Dubbeldam, D.; Calero, S. Molecular Mechanisms for Adsorption in Cu-BTC Metal Organic Framework. *J. Phys. Chem. C* **2013**, *117*, 11357−11366.
(27) Calero, S.; Gómez-Álvarez, P. Insights into the Adsorption of Water and Small Alcohols on the Open-Metal Sites of Cu-BTC via molecular simulation. *J. Phys. Chem. C* **2015**, *119*, 467−472.
(28) Zhao, Z.; Wang, S.; Yang, Y.; Li, X.; Li, J.; Li, Z. Competitive Adsorption and Selectivity of Benzene and Water Vapor on the Microporous Metal Organic Frameworks (HKUST-1). *Chem. Eng. J.* **2015**, *259*, 79−89.
(29) Yazaydın, A. Ö.; Benin, A. I.; Faheem, S. A.; Jakubczak, P.; Low, J. J.; Willis, R. R.; Snurr, R. Q. Enhanced CO_2 Adsorption in Metal-Organic Frameworks via Occupation of Open-Metal Sites by Coordinated Water Molecules. *Chem. Mater.* **2009**, *21*, 1425−1430.
(30) Myers, A. L.; Prausnitz, J. M. Thermodynamics of Mixed Gas Adsorption. *AIChE J.* **1965**, *11*, 121−130.
(31) Krishna, R.; van Baten, J. M. Hydrogen Bonding Effects in Adsorption of Water-alcohol Mixtures in Zeolites and the Consequences for the Characteristics of the Maxwell-Stefan Diffusivities. *Langmuir* **2010**, *26*, 10854−10867.
(32) Ruthven, D. M. *Principles of Adsorption and Adsorption Processes*; John Wiley: New York, 1984.
(33) Calleja, G.; Jimenez, A.; Pau, J.; Domínguez, L.; Pérez, P. Multicomponent Adsorption Equilibrium of Ethylene, Propane, Propylene and CO_2 on 13X Zeolite. *Gas Sep. Purif.* **1994**, *8*, 247−256.
(34) Talu, O.; Myers, A. L. Rigorous Thermodynamic Treatment of Gas-Adsorption. *AIChE J.* **1988**, *34*, 1887−1893.
(35) Talu, O.; Myers, A. L. Multicomponent Adsorption Equilibria of Nonideal Mixtures. *AIChE J.* **1986**, *32*, 1263−1276.
(36) Siperstein, F. R.; Myers, A. L. Mixed-Gas Adsorption. *AIChE J.* **2001**, *47*, 1141−1159.

DOI: 10.1021/jp512853w
J. Phys. Chem. C 2015, 119, 3658−3666

Supplementary Information (SI) to accompany:

Selective Adsorption of Water from Mixtures with 1-Alcohols by Exploitation of Molecular Packing Effects in CuBTC

Juan José Gutiérrez-Sevillano,[†] Sofia Calero,[†] and Rajamani Krishna[‡]

[†]Department of Physical, Chemical and Natural Systems

University Pablo de Olavide

Ctra. Utrera km. 1, 41013 Sevilla, Spain

[‡] Van 't Hoff Institute for Molecular Sciences, University of Amsterdam, Science Park 904,

1098 XH Amsterdam, The Netherlands

Table of Contents

1. Preamble

This ESI accompanying our manuscript *Selective Adsorption of Water from Mixtures with 1-Alcohols by Exploitation of Molecular Packing Effects in CuBTC* provides (a) structural details of CuBTC, (b) Configurational-Bias Monte Carlo (CBMC) simulation methodology with specification of force fields, (c) snapshots showing the location of adsorbed molecules within CuBTC framework, (d) 2-site and 3-site Langmuir-Freundlich fit parameters for unary isotherms, (e) details of the methodology used to calculate activity coefficients from CBMC mixture simulations, (f) details of IAST and RAST calculation procedures, and (g) simulation methodology for transient breakthroughs.

For ease of reading, this ESI is written as a stand-alone document; as a consequence, there is some overlap of material with the main manuscript. Researchers who are interested in specific sections can use the Table of Contents to skip to that specific section, without the need to wade through the entire material that is presented here.

2. Introduction

In the processing industries, distillation is the most common technology for separation of mixtures containing water and alcohols.[1, 2] The separation task is often rendered difficult because of azeotrope formation. The separation of azeotropic mixtures requires the addition of an additional component to the mixture, called entrainers, that alter the vapor/liquid equilibrium in a favorable manner in order to effect the desired separation in distillation columns.[3, 4] The recovery of entrainer requires an additional distillation processing step, placing additional energy demands because of vapor/liquid phase transformations in condensers, reboilers and solvent recovery sections. The energy consumption for distillation accounts for about 50% of the total energy consumption for all separations. The largest opportunities for energy reduction are offered by replacing distillation with (a) low-energy demanding separation systems such as adsorbers or membranes, or (b) hybrid systems that combine distillation with adsorption or membranes.[5] In many cases, the hybrid processing option is easier to implement

technically because adsorption and membrane separations often cannot produce products with the purity levels that are achievable with distillation. The success of such replacement strategies is crucially dependent on development of suitable microporous materials that can be used in fixed bed adsorption devices or as thin layers in membrane permeation units.

Microporous materials such as zeolites, metal-organic frameworks (MOFs) and zeolitic imidazolate frameworks (ZIFs) offer the potential for separation of mixtures of water and alcohols.[6, 7] A lot of the research work has been devoted to separation of dilute aqueous streams which require the selective adsorption of the desirable alcohols using hydrophobic adsorbents such as ZIF-8. [8, 9]

Our focus is on the problem of the selective adsorption of water from mixtures containing 1-alcohols. For example, this task is relevant for separating water/ethanol mixtures with the azeotropic composition 11%/89%. Water-selective separations are currently carried out using LTA-3A, LTA-4A, and LTA-5A zeolites; the separation principle is based primarily on the significantly larger diffusivity of water molecules across the narrow windows that are approximately 4 Å in size. Williams and Lawton[10] have evaluated a variety of desiccants, such as LTA-3A, silica, and alumina for the drying of a wide variety of organic solvents such as tetrahydrofuran (THF), toluene, dichloromethane (DCM), acetonitrile, methanol, and ethanol. Diffusion–selective separation of water/methanol mixtures is the underlying mechanism with Ln-MOF with pyrazine-2,5-dicarboxylate ligands as linkers.[11] Uchida and Mizuno[12] report uptake data for water, methanol, and ethanol in zeotype polyoxometalate-macro-cation ionic crystal, whose channels are not large enough to allow methanol and ethanol to enter. While diffusion-selective separations can be exploited in membrane constructs, its use in fixed bed adsorbers results in distended breakthrough characteristics with attendant lowering in the productivity.[13] For these reasons, we direct our attention at water-stable, hydrophilic, MOF adsorbents with "open structures" that are suitable for use in fixed bed units.

The novelty of the current investigation resides in the exploitation of the differences in the saturation capacities of water and 1-alcohols. Exploitation of differences in saturation capacities would necessarily require operation under conditions such that the pores of the adsorbent material are saturated; under

such conditions, the separations of mixtures are dictated by molecular packing effects which are expected to favor the smaller water molecules.[5]

Several recent investigations have demonstrated the exploitation of molecular packing effects for a wide variety of separations, as discussed below. For mixtures of 1-alcohols, the adsorption of the shorter alcohol can be achieved at high selectivity by operating at pore saturation conditions in CHA,[14] SAPO-34,[15] ZIF-8,[9] ZIF-68,[16] and UCY-5.[17] For mixtures of 1-alkanes, molecular packing effects at pore saturation can be exploited using CHA, ERI, LTA, and TSC to selectively adsorb the shorter 1-alkane component.[14, 18] For the separation of hexane isomers, necessary for octane enhancement of gasoline, molecular packing effects dictate the separations in AFI, ATS, CFI, and MFI zeolites.[19-24] The adsorption characteristics of xylene isomer mixtures within one-dimensional (1D) channels of AFI, MIL-47, MIL-53, MAF-X8, CAU-13, and MOF-CJ3 are primarily dictated by the efficiencies with which each isomer can be "stacked".[5, 25-33] The separation of chlorofluorocarbons with MFI zeolite relies on exploiting subtle configurational differences that lead to significantly different packing efficiencies.[34]

The molecular simulations of Nalaparaju et al.[35] for water/methanol and water/ethanol mixtures in ZIF-71 indicate that water can be selectively adsorbed near pore saturation conditions. However, subsequent experimental investigations[8, 36] do not support the results from the molecular simulations. In particular the uptake of water is significantly lower than that of the alcohols, suggesting that ZIF-71 has similar hydrophobic characteristics as ZIF-8, and ZIF-68.[8]

The approach we adopt here is to select the hydrophilic CuBTC (=$Cu_3(BTC)_2$ with BTC = 1,3,5-benzenetricarboxylate, also known as HKUST-1) as adsorbent. The primary objective of our article is to demonstrate the significant potential of CuBTC for selective adsorption of water from mixtures containing methanol, ethanol, and 1-propanol. We use Configurational-Bias Monte Carlo (CBMC) simulations to generate the required information on unary and mixture isotherms. The separation performance of CuBTC in fixed bed adsorbers is demonstrated by use of transient breakthrough simulations.

3. Vapor and liquid phase transitions

It is essential to gain an understanding of vapor/liquid phase transitions for water, and 1-alcohols. Figure 1a presents calculations of the molar densities of water, methanol, ethanol, and 1-propanol as a function of the bulk fluid phase fugacity using the Peng-Robinson equation of state. For fugacities below about 100 kPa, each of the components is in the gaseous phase. For fugacities in excess of 2 MPa, each of the substances water, methanol and ethanol is predominantly in the liquid state with molar densities in the range of 20 – 55 mol L^{-1}. For fugacities in the range of 700 kPa to 2 MPa, both vapor and liquid phases co-exist. A similar scenario holds for equimolar water/ethanol mixtures; see Figure 1b.

The important message we wish to draw from the calculations in Figure 1 is that care needs to be taken when interpreting unary isotherms of water and 1-alcohols, to be presented later. In our molecular simulations, we consistently use fugacities rather than "pressures" when plotting unary adsorption isotherms. This is vital because the bulk fluid phase could be either in the vapor phase, in the liquid phase, or a mixture of vapor and liquid phases.

4. CBMC simulation methodology

The structural information for CuBTC have been taken from Chui et al. [37] and Yang and Zhong.[38] The crystal structure of Chui et al.[37] includes axial oxygen atoms weakly bonded to the Cu atoms, which correspond to water ligands.

The CuBTC framework is composed of copper atoms connected by benzene-1,3,5-tricarboxylate (BTC) linkers, which form a characteristic paddle-wheel structure: two copper atoms bonded to the oxygen atoms of four BTC linkers, generating four-connected square-planar vertexes. The framework contains two types of large cavities (9 Å diameter) and small cavities (of 5 Å diameter). The larger cavities (L_2 and L_3) are similar in size and shape but as a result of the paddle-wheel, the copper atoms are only accessible from the L_3 cages. L_2 and L_3 cavities are connected by windows. The small cavities (T_1) are tetrahedral pockets enclosed by the benzene rings. They are connected to L_3 cages by small triangular windows as shown in Figure 2.

The tetrahedral pockets can accommodate about 9 molecules of water, but only about 1 molecule of 1-propanol; see Table 1.

Water is modeled using TIP5P-E[39] which has proven to be the most suitable model for water in Cu-BTC.[40] Furthermore, recently, Peng *et al*.[41] have found that at least a four sites model is needed to reproduce the right orientation of the water molecules in metal organic frameworks containing open metal sites. The alcohol molecules are modeled using TraPPE.[42] The Cu-BTC framework is modeled as a rigid structure based on the crystal structure of Chui *et al*.[37] with the atoms fixed in their crystallographic position. We removed the axial oxygen atoms weakly bonded to the copper atoms that correspond to water ligands. Lenard Jones parameters for the atoms were taken from DREIDING[43] force field except these for copper atoms that were taken from UFF[44] force field (Table 2). Additionally partial charges from Castillo *et al*.[40] were added to the model. The unit cell of our model is a cubic cell of $a = b = c = 26.34$ Å. The computed helium void fraction is of 0.76, the pore volume 0.85 cm^3/g and the surface area 2100 m^2/g. The framework density, $\rho = 879$ kg m^{-3}.

Water adsorption in CuBTC has also been investigated by Zang et al.[45] with the aid of molecular simulations.

Monte Carlo (MC) simulations were performed in the Grand Canonical (GC) Ensemble and Configurational Bias Monte Carlo (CBMC) technique was used for the insertion and deletion of molecules in and from the system. We used Lennard-Jones and electrostatic cutoffs of 12.0 Å. Coulombic interactions were computed using the Ewald summation technique with a relative precision of 10^{-6}.

Simulations were performed using the RASPA code developed by D. Dubbeldam, S. Calero, D. E. Ellis, and R.Q. Snurr. The code and most of the force fields and models used in this work have been extensively tested and validated with a large number of experimental and simulation data.[46-48]

5. Fitting of unary isotherms of water and 1-alcohols in CuBTC

Let us first consider the adsorption isotherms for water, plotted as a function of the fluid phase fugacity ranging to 10 MPa; see Figure 3.

The pure component isotherm data for water show marked inflections. The reason for these inflections can be traced to the location of water molecules within the tetrahedral pockets, and within the larger cages. In order to correctly capture these inflections the unary isotherm data of water were fitted with the 3-site Langmuir-Freundlich model:

$$q^0 = q_{A,sat}\frac{b_A f^{\nu_A}}{1+b_A f^{\nu_A}} + q_{B,sat}\frac{b_B f^{\nu_B}}{1+b_B f^{\nu_B}} + q_{c,sat}\frac{b_C f^{\nu_C}}{1+b_C f^{\nu_C}} \quad (1)$$

The saturation capacities q_{sat}, Langmuir constants b, and the Freundlich exponents ν, are provided in Table 3. The superscript 0 emphasizes that the loadings are for pure component water.

Figure 3 presents a comparison of the CBMC simulations for water adsorption in CuBTC with 3-site Langmuir-Freundlich model. Also shown are the experimental isotherm data of Zhao et al.,[49] Yazaydin et al.,[50] and Küsgens et al.[51] measured at 298 K. Our CBMC simulations are in reasonable agreement with the experimental data; in particular, the steep portion of the isotherm is correctly reproduced. This corresponds to the filling up of the larger cages of CuBTC.

The unary isotherms for methanol, ethanol, 1-propanol were fitted with good accuracy with the dual-Langmuir-Freundlich model

$$q^0 = q_{A,sat}\frac{b_A f^{\nu_A}}{1+b_A f^{\nu_A}} + q_{B,sat}\frac{b_B f^{\nu_B}}{1+b_B f^{\nu_B}} \quad (2)$$

with the fits parameters as specified in Table 4.

Figure 4a provides a comparison of the CBMC simulated isotherms for water, methanol, ethanol, and 1-propanol with 3-site, and 2-site Langmuir-Freundlich fits. The accuracy of the fits is excellent for all four guest molecules. Particularly noteworthy are the differences in the saturation capacities, $q_{sat} = q_{A,sat} + q_{B,sat} + q_{C,sat}$, of the various guest molecules: water = 54 mol kg^{-1}; methanol = 19.9 mol kg^{-1}; ethanol = 13 mol kg^{-1}; 1-propanol = 10 mol kg^{-1}.

The experimental data of van Assche et al.[52] for unary isotherms of water, and alcohols in CuBTC at 323 K are shown in Figure 4b. The experimental data also show a similar hierarchy of component loadings as observed in the CBMC data.

We will see later that the "driver" for mixture separations is the large differences in saturation capacities of water and other 1-alcohols.

Let us define the fractional pore occupancy within the pores, θ_i, for each of the four guest molecules

$$\theta_i = \frac{q^0}{q_{sat}} \tag{3}$$

where q^0 is the molar loading of species i that is determined from the mult-site Langmuir-Freundlich fits. The variation of the pore occupancies with bulk fluid phase fugacity, f_i, are shown in Figure 5. We note that the pore occupancies are close to unity for operation at ambient conditions of 100 kPa and 298 K.

Most commonly, industrial separations are anticipated to operate with bulk liquid mixtures; this ensures that pore saturation conditions are reached.[5] This is an important aspect of this work, because the separations are dictated by molecular packing effects that manifest at pore saturation conditions.

6. CBMC simulations of mixture adsorption

Figure 6 shows the average occupation profiles (AOP) of alcohols and water in the Cu-BTC. The data correspond to the quaternary water/methanol/ethanol/1-propanol mixture at 50 kPa. The AOP are superposed on to the iso-contour picture of energy landscape of the Cu-BTC framework.

Figure 7 presents the results for CBMC simulations of the component loadings for adsorption of equimolar (a) water/methanol, (b) water/ethanol, (c) water/1-propanol, (d) water/methanol/ethanol/1-propanol, and (e) methanol/ethanol mixtures in CuBTC at 298 K.

Figure 8 presents the calculations of the adsorption selectivties for equimolar (a) water/methanol, (b) water/ethanol, (c) water/1-propanol, (d) water/methanol/ethanol/1-propanol, and (e) methanol/ethanol mixtures in CuBTC at 298 K.

In all cases, we note a reversal in the hierarchy of component loadings as conditions approach pore saturation. In all five cases, we note that at conditions close to pore saturation, the adsorption is in favor of the component with the higher saturation capacity. For water-bearing mixtures, the selectivity is in favor of water at conditions close to 100 kPa. For methanol/ethanol mixtures, the adsorption is in favor of the shorter alcohol as pore saturation is approached.

We now examine whether the IAST theory provides a quantitative representation of mixture adsorption.

7. Summary of IAST calculation methodology

Briefly, the basic equation of Ideal Adsorbed Solution Theory (IAST) theory of Myers and Prausnitz[53] is the analogue of Raoult's law for vapor-liquid equilibrium, i.e.

$$f_i = P_i^0 x_i; \quad i = 1,2,...n \tag{4}$$

where x_i is the mole fraction in the adsorbed phase

$$x_i = \frac{q_i}{q_1 + q_2 + ...q_n} \tag{5}$$

and P_i^0 is the pressure for sorption of every component *i*, which yields the same spreading pressure, π for each of the pure components, as that for the mixture:

$$\frac{\pi A}{RT} = \int_0^{P_1^0} \frac{q_1^0(f)}{f} df = \int_0^{P_2^0} \frac{q_2^0(f)}{f} df = \int_0^{P_3^0} \frac{q_3^0(f)}{f} df = ... \tag{6}$$

where *R* is the gas constant (= 8.314 J mol^{-1} K^{-1}), and $q_i^0(f)$ is the *pure* component adsorption isotherm given by Equations (1) or Equation (2). The molar loadings $q_i^0(f)$ are expressed in the units of moles adsorbed per kg of framework, i.e. mol kg^{-1}. The units of the spreading pressure π is the same as that for surface tension, i.e. N m^{-1}; indeed the spreading pressure is the negative of the surface tension.[53] The quantity *A* on the left side of Equation (6) is the surface area per kg of framework, with units of m^2 kg^{-1}. The units of $\frac{\pi A}{RT}$ are mol kg^{-1}.

Each of the integrals in Equation (6) can be evaluated analytically. For the 3-site Langmuir-Freundlich isotherm, the integration yields

$$\int_{f=0}^{P} \frac{q^0(f)}{f} df = \frac{q_{A,sat}}{\nu_A} \ln\left(1 + b_A P^{\nu_A}\right) + \frac{q_{B,sat}}{\nu_B} \ln\left(1 + b_B P^{\nu_B}\right) + \frac{q_{c,sat}}{\nu_C} \ln\left(1 + b_C P^{\nu_C}\right) \quad (7)$$

The right hand side of equation (7) is a function of P. For multicomponent mixture adsorption, each of the equalities on the right hand side of Equation (6) must satisfied. These constraints may be solved using a suitable root-finder, to yield the set of values of P_1^0, P_2^0, P_3^0,.. P_n^0, all of which satisfy Equation (6). The corresponding values of the integrals using these as upper limits of integration must yield the same value of $\frac{\pi A}{RT}$ for each component; this ensures that the obtained solution is the correct one.

The adsorbed phase mole fractions x_i are then determined from

$$x_i = \frac{f_i}{P_i^0}; \quad i = 1,2,...n \quad (8)$$

The total amount adsorbed is calculated from

$$q_t \equiv q_1 + q_2 ... + q_n = \frac{1}{\frac{x_1}{q_1(P_1^0)} + \frac{x_2}{q_2(P_2^0)} + ... + \frac{x_n}{q_n(P_n^0)}} \quad (9)$$

The set of equations (1), (2), (4), (5), (6) (7), and (9) need to be solved numerically to obtain the loadings, q_i of the individual components in the mixture.

8. Mixture adsorption equilibrium: CBMC vs IAST

Figures 9 and 10 compares the IAST calculations with CBMC simulations of component loadings of equimolar (a) water/methanol, (b) water/ethanol, (c) water/1-propanol, (d) water/methanol/ethanol/1-propanol, and (e) methanol/ethanol mixtures. The same data is plotted in Figures 9 and 10, using linear y-axes, and logarithmic y-axes, respectively. For methanol/ethanol mixtures, the agreement between the IAST and CBMC simulations is excellent for $f_t < 10$ kPa. For water/methanol mixtures, the agreement

between the IAST and CBMC simulations is excellent for f_t < 100 Pa. For water/ethanol mixtures, the agreement between the IAST and CBMC simulations is excellent for f_t < 50 Pa. For water/1-propanol mixtures, the agreement between the IAST and CBMC simulations is excellent for f_t < 10 Pa. For water/methanol/ethanol/1-propanol mixtures, the agreement between the IAST and CBMC simulations is excellent for f_t < 15 Pa. For f_t higher than the values indicated in the foregoing, there are significant quantitative departures between CBMC simulations and IAST predictions. The reasons for the deviations can be attributed to the influence of hydrogen bonding, as explained in our earlier work.[54] However, the IAST correctly anticipates that the adsorption is favorable to water as saturation conditions are approached. However, the quantitative agreement between the CBMC mixtures simulations and IAST is not of sufficient accuracy near saturation conditions to be used in the transient breakthrough calculations presented later.

The failure of the IAST to accurately represent the component loadings at pore saturation conditions has been underscored also for DDR zeolite. [54]

9. Calculation of activity coefficients using CBMC mixture simulations

It is clear from the results presented in Figures 9 and 10 that the assumption of an *ideal* adsorbed phase breaks down as saturation conditions are approached. Let us quantify these deviations by introducing activity coefficients following Myers and Prausnitz.[53]

To account for non-ideality effects in mixture adsorption, we introduce activity coefficients γ_i into Equation (4).

$$f_i = P_i^0 x_i \gamma_i \qquad (10)$$

The CBMC mixture simulations provide information on the mole fractions of the adsorbed phase, x_i, but the activity coefficients γ_i are not known *a priori*.

We discuss a procedure by which the activity coefficients γ_i can be determined using as data inputs, the CBMC simulated component loadings in the mixture as a function of the partial fugacities, f_i, in the bulk fluid phase. We illustrate this procedure for a binary mixture.

Using the Gibbs adsorption equation for mixture adsorption as starting point (cf. Equations (3.52) of Ruthven[55]), we can write the differential of the spreading pressure as

$$\frac{Ad\pi}{RT} = q_1 d\ln f_1 + q_2 d\ln f_2 \tag{11}$$

Integrating equation (11) from 0 to f_1, and f_2

$$\frac{\pi A}{RT} = \int_0^{f_1,f_2} \left(q_1 d\ln f_1 + q_2 d\ln f_2\right) = \int_0^{f_t} \left(q_1 + q_2\right) d\ln f_t \tag{12}$$

The integral in equation (12) can be determined using an appropriate quadrature formula. The approach we use here is to fit the water loadings q_1, and the total mixture loading $q_t = q_1 + q_2$ as functions, respectively, of the partial fugacities, f_1, and total mixture fugacity f_t.

The P_i^0 can be determined for each of the two components by setting the equalities:

$$\frac{\pi A}{RT} = \int_0^{f_t} \left(q_1 + q_2\right) d\ln f_t = \int_0^{P_1^0} \frac{q_1^0(f)}{f} df = \int_0^{P_2^0} \frac{q_2^0(f)}{f} df \tag{13}$$

Equation (13) can be solved to determine P_1^0, and P_2^0 as a function of f_1, and f_2. Combining the obtained values of P_1^0, and P_2^0 with Equation (10), we can determine the activity coefficients γ_i as a function of the partial fugacities f_1, and f_2, For this purpose, the CBMC mixture simulations in combination with Equation (5) allow calculations of the adsorbed phase, x_i, as function of $f_t = f_1 + f_2$.

The adopted procedure is illustrated, step-by-step, for the CBMC water/ethanol mixture data reported in Figure 7b.

Step 1. We first fit the component water loadings q_1, and the total mixture loading $q_t = q_1 + q_2$ as functions, respectively, of the partial fugacities, f_1, and total fugacity f_t using the Dual-Langmuir-Freundlich model. The fit parameters are specified in Table 5. To demonstrate the goodness of the fits, Figure 11 compares the CBMC mixture simulation data with the fits for water loadings q_1, and the total mixture loading $q_t = q_1 + q_2$ with fitted model. The fits are of excellent accuracy.

From these fits, we can determine the mole fraction of water in the adsorbed phase, x_1. The mole fraction of ethanol in the adsorbed phase, $x_2 = 1 - x_1$.

Step 2. We determine the value of $\frac{\pi A}{RT}$ by analytic integration of the first right member of Equation (13). The formula for analytic integration is as follows

$$\frac{\pi A}{RT} = \int_0^{f_t} (q_1 + q_2) d \ln f_t = \frac{q_{A,sat}}{\nu_A} \ln\left(1 + b_A f_t^{\nu_A}\right) + \frac{q_{B,sat}}{\nu_B} \ln\left(1 + b_B f_t^{\nu_B}\right) \tag{14}$$

In determining the right member of equation (14) we use the DLF fit parameters for the mixture loadings as specified in Table 5.

Step 3. We determine $P_1^0(\pi)$, and $P_2^0(\pi)$ as a function of f_t by using an appropriate root-finder routine.

Step 4. The activity coefficient of water in the adsorbed phase is calculated from

$$\gamma_1 = \frac{f_1}{P_i^0 x_1} \tag{15}$$

In evaluation of equation (15), we calculate x_1 from the DLF fits of CBMC data:

$$x_1 = \frac{q_1}{q_t} \tag{16}$$

The activity coefficient of water in the adsorbed phase is calculated from

$$\gamma_2 = \frac{f_2}{P_2^0 (1 - x_1)} \tag{17}$$

Figure 12 presents the activity coefficients γ_i for equimolar (a) water/methanol, (b) water/ethanol, (c) water/1-propanol, and (d) methanol/ethanol mixtures.

For water/methanol mixtures, we note that at a total bulk fluid phase fugacity $f_t = f_1 + f_2 < 200$ Pa, the activity coefficients of each component is approximately unity. The small departures from unity at low pressures is a consequence of the numerical fitting procedure employed in the calculations of the

activity coefficients; the fundamentally correct limiting value of the activity coefficient $\gamma_i \to 1; \quad f_t \to 0$ cannot be prescribed. With increasing values of f_t, the activity coefficient of water increases whereas that of methanol decreases. For water/ethanol and water/1-propanol mixtures, similar trends are observed but the threshold values are lower, about 10 Pa in each case.

For methanol/ethanol mixtures, the activity coefficients deviate significantly from unity only for $f_t = f_1 + f_2 > 10$ kPa.

From the results presented in Figure 12 and Figure 13, using linear, and logarithmic y-axies, it appears that non-idealities are much more significant for water/alcohol mixtures than for methanol/ethanol mixtures. These deviations are most likely correlated with the hydrogen bonding effects that are stronger between water and alcohol molecules than between pairs of alcohol molecules; a quantitative justification is provided in our earlier work.[54]

10. Non-ideality effects for mixture adsorption in FAU, DDR, MFI, and LTA-4A zeolites

Using published data on CBMC mixture simulations we shall examine the non-ideality effects for mixture adsorption in thre different zeolites, FAU, DDR, and MFI. Also included in this analysis are the experimental data of Pera-Titus et al.[56] for water/ethanol adsorption in LTA-4A.

Let us consider the adsorption of water/methanol, and water/ethanol mixtures in all-silica FAU zeolite that consists of 786 $Å^3$ cages, that are separated by 7.3 Å size windows. Figure 14 shows CBMC simulations of Krishna and van Baten[54] for pure component adsorption isotherms for water, methanol, and ethanol in all-silica FAU zeolite at 300 K. Above fluid phase fugacities of 10^4 Pa, pore saturation is reached and the hierarchy of saturation capacities water >> methanol > ethanol is a reflection of the size of the molecules.

Figures 15a, and 15b present CBMC simulations for adsorption of equimolar (f_1=f_2) (a) water/methanol, and (b) water/ethanol in FAU zeolite at 300 K. In the Henry regime of adsorption, the water loading is significantly below that of the alcohol. However, we note that at total bulk fluid phase fugacities, $f_t = f_1+f_2 > 2\times10^4$ Pa, the adsorption is in favor of water, a consequence of entropy effects.

IAST calculations are able to provide a reasonably good description of mixture adsorption equilibrium for both water/methanol and water/ethanol mixtures for $f_1+f_2 < 1\times10^3$ Pa. For $f_1+f_2 > 1\times10^4$ Pa, there are significant quantitative deviations between IAST calculations and CBMC mixture simulations.

Figures 15c, and 15d presents the calculations of the activity coefficients γ_i, of individual components in the mixture as a function of the total fluid phase fugacity, f_1+f_2. The trends in the values of activity coefficients γ_i are similar to that observed for the corresponding mixtures in CuBTC.

Figure 16a presents CBMC simulations for adsorption of water/methanol mixtures in FAU zeolite at 300 K at a constant total fugacity of 1000 Pa. The continuous solid lines are the IAST calculations using the pure component fits in Table **6**. The agreement between the IAST calculations and CBMC mixture simulations is not perfect; this is reflected also in the departures in the values of the activity coefficients γ_i from unity; see Figure 16b.

Consider the adsorption of water/methanol, and water/ethanol mixtures in all-silica DDR zeolite that consists of 278 Å^3 cages, that are separated by 3.65 Å × 4.37 Å size windows. Figure 17 shows CBMC simulations of Krishna and van Baten[54] for pure component adsorption isotherms for water, methanol, and ethanol in DDR at 300 K. Above fluid phase fugacities of 10^5 Pa, pore saturation is reached and the hierarchy of saturation capacities water >> methanol > ethanol is a reflection of the size of the molecules.

Figures 18a, and 18b present CBMC simulations for adsorption of equimolar ($f_1=f_2$) (a) water/methanol, and (b) water/ethanol mixtures in DDR zeolite. In the Henry regime of adsorption, the water loading is significantly below that of the alcohol. However, we note that at total bulk fluid phase fugacities, $f_t = f_1+f_2 > 10^5$ Pa, the adsorption is in favor of water. The predictions of IAST are not quantitatively adequate and this is reflected also in the departures in the values of the activity coefficients γ_i from unity; see Figures 18c, and18d.

Consider the adsorption of water/methanol, and water/ethanol mixtures in all-silica MFI zeolite that consists of intersecting channels of 5.5 Å. Figure 19 shows CBMC simulations of Krishna and van Baten[54] for pure component adsorption isotherms for water, methanol, and ethanol in MFI at 300 K.

Above fluid phase fugacities of 10^5 Pa, pore saturation is reached and the hierarchy of saturation capacities water >> methanol > ethanol is a reflection of the size of the molecules.

Figures 20a, and 20b present CBMC simulations for adsorption of equimolar (f_1=f_2) (a) water/methanol, and (b) water/ethanol mixtures in MFI zeolite. In the Henry regime of adsorption, the water loading is significantly below that of the alcohol. However, we note that at total bulk fluid phase fugacities, $f_t = f_1+f_2 > 10^5$ Pa, the adsorption is in favor of water. This is due to entropy effects. IAST calculations are able to provide a reasonably adequate description of mixture adsorption equilibrium for both water/methanol and water/ethanol mixtures.

Let us consider the LTA zeolite for which the all-silica form (i.e. without cations, also called ZK-4) consists of 743 $Å^3$ cages that are separated by windows of approximately 4.1 Å × 4.7 Å. Figure 21 presents snapshots showing the location of cations in the industrially important LTA-4A (96 Si, 96 Al, 96 Na^+, Si/Al=1), and LTA-5A (96 Si, 96 Al, 32 Na^+, 32 Ca^{++}, Si/Al=1) zeolites. In LTA-4A, some of the Na^+ cations partially block the window regions,[57-61] thereby effectively reducing the aperture size that is available for inter-cage hopping of molecules. The Na^+ and Ca^{++} cations in LTA-5A, on the other hand, do not locate near the window regions and there is no blocking. This implies that diffusional influences are much stronger in LTA-4A than in LTA-5A zeolite. The presence of bulkier K^+ cations in LTA-3A (96 Si, 96 Al, 96 K^+, Si/Al=1) causes the window blocking effect to be significantly enhanced, when compared to LTA-4A. For this reason, LTA-3A zeolite is used for selective removal of water from gaseous streams (dehumidification) and water/alcohol mixtures (dehydration) mixtures.[62] It has to be mentioned that it is common to find information in the published literature that suggest that 3A, 4A, and 5A zeolites have window apertures, respectively, of 3 Å, 4 Å, and 5; this is not precisely correct. The degree of blocking (by the cations Na^+ or K^+) of the window apertures of the pristine framework with 4.1 Å × 4.7 Å decreases in the order as we progress from 3A, and 4A, to 5A.

Let us examine the experimental data on the pure component isotherms for water and ethanol in LTA-4A published by Pera-Titus et al;[56] see Figure 22. We note that the saturation capacity of water is considerable higher than that of ethanol. The experimental data for adsorbed phase component loadings

from vapor phase water/ethanol mixtures at 2.1 kPa are shown in Figure 23. The experimental data for adsorbed phase component loadings from vapor phase water/ethanol mixtures are in reasonably good agreement with IAST calculations.

11. CBMC mixture simulations vs RAST calculations

Following the work of Calleja et al.,[63] we have used the Wilson model to describe the variation of the activity coefficients with the composition of the adsorbed mixtures

$$\ln(\gamma_1) = 1 - \ln(x_1 + x_2\Lambda_{12}) - \frac{x_1}{x_1 + x_2\Lambda_{12}} - \frac{x_2\Lambda_{21}}{x_2 + x_1\Lambda_{21}}$$
$$\ln(\gamma_2) = 1 - \ln(x_2 + x_1\Lambda_{21}) - \frac{x_2}{x_2 + x_1\Lambda_{21}} - \frac{x_1\Lambda_{12}}{x_1 + x_2\Lambda_{12}} \qquad (18)$$

The choice of $\Lambda_{12} = \Lambda_{21} = 1$ in Equation (18) reduces equation (10) to equation (4). The parameters Λ_{12} and Λ_{21} can be fitted to match the CBMC mixture simulations. Table 10 lists the Wilson non-ideality parameters Λ_{12} and Λ_{21} fitted in this manner for mixtures of water and 1-alcohols.

Figure 24a,b,c,d,e compare the RAST estimations with CBMC simulations of component loadings of the five different mixtures. We observe a reasonably good agreement between CBMC simulation data and RAST calculations for conditions nearer pore saturation.

For mixture adsorption, let us define the fractional occupancy within the pores, θ_t

$$\theta_t = \sum_{i=1}^{n} \frac{q_i}{q_{i,sat}} \qquad (19)$$

where q_i is the molar loading of species i in the mixture, and $q_{i,sat}$ is its saturation capacity. Figure 25 shows the fractional pore occupancy θ_t for adsorption of equimolar water/methanol/ethanol/1-propanol mixtures as a function of the bulk fluid phase fugacity, f_t. We note that the pores are saturated when the bulk fluid phase fugacity exceeds about 10 kPa.

12. Comments on the shortcomings of the Calleja implementation of the RAST model

An important shortcoming of the RAST implementation of Calleja et al.[63] is that the correct limiting behavior of activity coefficients $\gamma_i \to 1; \quad f_t \to 0$ is not prescribed. Consequently, RAST predictions of mixture adsorption are not accurate in the limit of low fugacities. One approach to redress this problem, is to adopt the strategy suggested by Talu and Myers[64, 65] and Siperstein and Myers.[66] Essentially, their strategy involves introducing the correction factor $\left(1-\exp\left(-C\frac{\pi A}{RT}\right)\right)$ into the right members of Equation (18) as follows

$$\begin{aligned}\ln(\gamma_1) &= \left(1-\ln(x_1+x_2\Lambda_{12})-\frac{x_1}{x_1+x_2\Lambda_{12}}-\frac{x_2\Lambda_{21}}{x_2+x_1\Lambda_{21}}\right)\left(1-\exp\left(-C\frac{\pi A}{RT}\right)\right)\\ \ln(\gamma_2) &= \left(1-\ln(x_2+x_1\Lambda_{21})-\frac{x_2}{x_2+x_1\Lambda_{21}}-\frac{x_1\Lambda_{12}}{x_1+x_2\Lambda_{12}}\right)\left(1-\exp\left(-C\frac{\pi A}{RT}\right)\right)\end{aligned} \qquad (20)$$

The constant *C*, with the units kg mol^{-1}, needs to be determined from measured experimental data using the procedure described in Siperstein and Myers.[66] Alternatively, the constant *C* can be determined from the CBMC mixture simulation data by attempting to match RAST predictions using equation (20) with CBMC simulated data. The introduction of $\left(1-\exp\left(-C\frac{\pi A}{RT}\right)\right)$ imparts the correct limiting behaviors $\gamma_i \to 1; \quad f_t \to 0$ for the activity coefficient in the Henry regime. As pore saturation conditions are approached, this correction factor tends to unity $\left(1-\exp\left(-C\frac{\pi A}{RT}\right)\right)\to 1$. To illustrate this, we present calculations of the correction factor for water/1-propanol mixtures using the fits of CBMC mixture simulations that were used to determine the activity coefficients; see Figure 26. These calculations are based on the equation (20) taking Λ_{12} = 2; Λ_{21}= 300; C = 0.1 kg mol^{-1}. These values were obtained by matching the RAST calculations of component loadings with CBMC mixture simulations.

In the work presented here we have not implemented the correction $\left(1-\exp\left(-C\frac{\pi A}{RT}\right)\right)$ because this factor impacts the characteristics of the Henry regime, but its influence on the RAST predictions near pore saturation is of lesser importance.

13. Simulation methodology for transient breakthrough in fixed bed adsorbers

What we have established so far is that for operations close to pore saturation conditions, CuBTC favors the adsorption of the species with the highest saturation capacity. For example, at f_t = 100 kPa for water/methanol/ethanol/1-propanol mixtures, the results presented in Figures 9 and 10 indicate the adsorption hierarchy water > methanol > ethanol > 1-propanol. Whereas for operations at low pore occupancies, at say f_t = 10 Pa the adsorption is strongly in favor of 1-propanol.

However, IAST or RAST calculations on their own cannot be used as indicators of the separations achievable in fixed bed adsorbers, as we explain below.

Fixed bed, packed with crystals of microporous materials, are commonly used for separation of mixtures (see schematic in Figure **27**). Such adsorbers are commonly operated in a transient mode, and the compositions of the gas phase, and component loadings within the crystals, vary with position and time. During the initial stages of the transience, the pores are loaded up gradually, and only towards the end of the adsorption cycle are conditions corresponding to pore saturation achieved. Put another way, separations in fixed bed adsorbers are influenced by both the Henry regime of adsorption as well as the conditions corresponding to pore saturation. In essence the history of component loadings within the crystals follows the entire trajectory, from left to right, of the data presented in Figures 9 and 10. Put another way, the separations in fixed bed adsorbers reflect the "integral" of the component loading for the range 0 - f_t. [13, 67]

We describe below the simulation methodology used to perform transient breakthrough calculations that are presented in this work. This simulation methodology is the same as that used in our previous published work;[13] a brief summary is provided here for completeness.

Assuming plug flow of an *n*-component gas mixture through a fixed bed maintained under isothermal conditions, the partial pressures in the gas phase at any position and instant of time are obtained by solving the following set of partial differential equations for each of the species *i* in the gas mixture.[68]

$$\frac{1}{RT}\frac{\partial p_i(t,z)}{\partial t} = -\frac{1}{RT}\frac{\partial\left(v(t,z)p_i(t,z)\right)}{\partial z} - \frac{(1-\varepsilon)}{\varepsilon}\rho\frac{\partial \bar{q}_i(t,z)}{\partial t}; \quad i = 1,2,...n \tag{21}$$

In equation (21), t is the time, z is the distance along the adsorber, ρ is the framework density, ε is the bed voidage, v is the interstitial gas velocity, and $\bar{q}_i(t,z)$ is the *spatially averaged* molar loading within the crystallites of radius r_c, monitored at position z, and at time t. The framework density of CuBTC ρ is = 878.83 kg m^{-3} has been used in the simulations.

At any time t, during the transient approach to thermodynamic equilibrium, the spatially averaged molar loading within the crystallite r_c is obtained by integration of the radial loading profile

$$\bar{q}_i(t) = \frac{3}{r_c^3}\int_0^{r_c} q_i(r,t)r^2 dr \tag{22}$$

For transient unary uptake within a crystal at any position and time with the fixed bed, the radial distribution of molar loadings, q_i, within a spherical crystallite, of radius r_c, is obtained from a solution of a set of differential equations describing the uptake

$$\frac{\partial q_i(r,t)}{\partial t} = -\frac{1}{\rho}\frac{1}{r^2}\frac{\partial}{\partial r}\left(r^2 N_i\right) \tag{23}$$

The molar flux N_i of component i is described by the simplified version of the Maxwell-Stefan equations in which both correlation effects and thermodynamic coupling effects are considered to be of negligible importance[13]

$$N_i = -\rho Đ_i\frac{\partial q_i}{\partial r} \tag{24}$$

Summing equation (**22**) over all n species in the mixture allows calculation of the *total average* molar loading of the mixture within the crystallite

$$\bar{q}_t(t,z) = \sum_{i=1}^{n} \bar{q}_i(t,z) \tag{25}$$

The *interstitial* gas velocity is related to the *superficial* gas velocity by

$$v = \frac{u}{\varepsilon} \tag{26}$$

In industrial practice, the most common operation is with to use a step-wise input of mixtures to be separation into an adsorber bed that is initially free of adsorbates, i.e. we have the initial condition

$$t = 0; \quad q_i(0,z) = 0 \tag{27}$$

At time, t = 0, the inlet to the adsorber, z = 0, is subjected to a step input of the n-component gas mixture and this step input is maintained till the end of the adsorption cycle when steady-state conditions are reached.

$$t \geq 0; \quad p_i(0,t) = p_{i0}; \quad u(0,t) = u \tag{28}$$

where u is the superficial gas velocity at the inlet to the adsorber.

If the value of $\frac{Đ_i}{r_c^2}$ is large enough to ensure that intra-crystalline gradients are absent and the entire crystallite particle can be considered to be in thermodynamic equilibrium with the surrounding bulk gas phase at that time t, and position z of the adsorber

$$\bar{q}_i(t,z) = q_i(t,z) \tag{29}$$

The molar loadings at the *outer surface* of the crystallites, i.e. at $r = r_c$, are calculated on the basis of adsorption equilibrium with the bulk gas phase partial pressures p_i at that position z and time t. For CuBTC, we do not expect intra-crystalline diffusion resistances to be significant, and therefor equation (29) is invoked in all the transient breakthroughs presented here. Validation of this conclusion is provided in earlier works.[69, 70] For inlet fugacities f_t = 100 kPa, the adsorption equilibrium can be calculated on the basis of the Real Adsorbed Solution Theory (RAST) of Myers and Prausnitz with the Wilson parameters specified in Table 10.

For presenting the breakthrough simulation results, we use the dimensionless time, $\tau = tu/(L\varepsilon)$, obtained by dividing the actual time, t, by the characteristic time, $L\varepsilon/u$, where L is the length of adsorber, u is the superficial fluid velocity, ε is the bed voidage.[67] For all the simulations reported in this article we choose L = 0.3 m; u = 0.04 m s^{-1}; ε = 0.4.

14. Transient breakthrough simulation results

Figure 28 presents transient breakthroughs for equimolar (a) water/methanol, (b) water/ethanol, (c) water/1-propanol, (d) water/methanol/ethanol/1-propanol, and (e) methanol/ethanol mixtures in CuBTC at 298 K and total fugacity of 100 kPa. In the four cases (a), (b), (c) and (d), we note that water elutes the adsorber at the end of the cycle and the partner alcohol species are rejected into the bulk fluid phase during the early stages of the transient breakthroughs. For breakthroughs with the 4-component mixture, the elution sequence is 1-propanol, ethanol, methanol, and water; this sequence is primarily dictated by the hierarchy of saturation capacities. For methanol/ethanol mixtures (cf. Figure 28e), the shorter alcohol is adsorbed preferentially, and the longer alcohol elutes first. Similar characteristics for ethanol/1-propanol and ethanol/1-hexanol mixtures in a fixed bed adsorber packed with SAPO-34, have been experimentally observed in the breakthrough experiments reported by Remy et al;[15] their experiments confirm that the shorter 1-alcohol is preferentially adsorbed and elutes last in the sequence.

In order to underscore the phenomenon of selectivity reversal, Figure 30a presents transient breakthroughs for equimolar water/ethanol mixtures in CuBTC at 298 K, and total fluid phase fugacity of 1 kPa. At the total fugacity, the adsorption is in favor of ethanol that elutes last.

Figure 31a presents a comparison of the transient breakthroughs for equimolar water/methanol/ethanol/1-propanol mixtures in CuBTC at 298 K, and total fluid phase fugacity of (a) 1 kPa, and (b) 100 kPa. For f_t = 1 kPa, the sequence of breakthroughs is water, methanol, ethanol, and 1-propanol; this sequence reflects the hierarchy of adsorption strengths in the Henry regime. However, for f_t = 100 kPa the elution sequence is 1-propanol, ethanol, methanol, and water that is dictated by saturation capacities.

The simulation data presented in Figure 31 demonstrate that it is possible to selectively adsorb water from *equimolar* mixtures with alcohols. The question arises whether the selective water adsorption would also manifest for mixtures with only small amounts of water. In order to address this question we carried out transient breakthrough simulations for binary (a) water/methanol, (b) water/ethanol, and (c) water/1-propanol mixtures with 8% water in the feed; the results are presented in Figure 29. We note that CuBTC is also effective in adsorbing small quantities of water from alcohol-rich feed mixtures.

Let us compare water/ethanol separations using CuBTC with those realized with LTA-4A zeolite. Figure 32a shows the transient breakthroughs for equimolar water/ethanol mixtures in LTA-4A zeolite at 298 K. The breakthrough calculations for LTA-4A are performed using fitted pure component experimental data of Pera-Titus[56] as reported in Table 9. The breakthrough calculations for LTA-4A are performed using IAST, in view of the results presented in Figure 23. For a fair comparison of the two MOFs, we also ignore intra-crystalline diffusion influences in LTA-4A zeolite. Comparison of the results in Figure 32a with those in Figure 32b shows that the breakthrough times with CuBTC are significantly longer; this is because of higher saturation loadings of all guest molecules. Longer breakthrough times are desirable because it leads to longer cycle times and higher productivities. For separations in fixed bed adsorbers, CuBTC appears to be superior to LTA-4A.

15. Notation

A	surface area per kg of framework, $m^2\ kg^{-1}$
b_A	Langmuir-Freundlich constant for adsorption site A, $Pa^{-\nu_A}$
b_B	Langmuir-Freundlich constant for adsorption site B, $Pa^{-\nu_B}$
b_C	Langmuir-Freundlich constant for adsorption site C, $Pa^{-\nu_C}$
C	constant used in equation (20), $kg\ mol^{-1}$
c_i	molar concentration of species i in gas mixture, $mol\ m^{-3}$
c_{i0}	molar concentration of species i in gas mixture at inlet to adsorber, $mol\ m^{-3}$
$Đ_i$	Maxwell-Stefan diffusivity, $m^2\ s^{-1}$
f_i	partial fugacity of species i, Pa
f_t	total fugacity of bulk fluid mixture, Pa
L	length of packed bed adsorber, m
n	number of species in the mixture, dimensionless
N_i	molar flux of species i, $mol\ m^{-2}\ s^{-1}$
P_i^0	sorption pressure, Pa
q_i	component molar loading of species i, $mol\ kg^{-1}$
q_t	total molar loading for mixture adsorption, $mol\ kg^{-1}$
$q_{i,sat}$	molar loading of species i at saturation, $mol\ kg^{-1}$
r_c	radius of crystallite, m
R	gas constant, 8.314 $J\ mol^{-1}\ K^{-1}$
t	time, s
T	absolute temperature, K
u	superficial gas velocity in packed bed, $m\ s^{-1}$
v	interstitial gas velocity in packed bed, $m\ s^{-1}$

Greek letters

ε	voidage of packed bed, dimensionless
γ_i	activity coefficient of component i in adsorbed phase, dimensionless

ν	exponent in multi-site-Langmuir-Freundlich isotherm, dimensionless
π	spreading pressure, N m^{-1}
Λ_{ij}	Wilson parameters defined by Equation (18), dimensionless
θ_t	fractional occupancy for mixture adsorption, dimensionless
τ	time, dimensionless

Subscripts

i	referring to component *i*
t	referring to total mixture

Table 1. Number of molecules that can be located in the tetrahedral pockets.

	f kPa	Loading /molec uc^{-1}	Loading in T1 cages/ molec uc^{-1}	Tetrahedral cages molec/T1 cage
Methanol	10000	202	29	3-4
Ethanol	50	125	21	2-3
1-Propanol	30000	98	8	1
Water	30000	512	72	9

Table 2. Lennard Jones parameters and point charges for the Cu-BTC and adsorbates.

Atom types	**Epsilon/k_B (K)**	**Sigma (Å)**	**Charge (*e*)**
Adsorbates			
CH_3_C_ol	98.0	3.75	-
CH_3_O_ol	98.0	3.75	0.265
CH_2_C_ol	46.0	3.95	-
CH_2_O_ol	46.0	3.95	0.265
O_ol	93.0	3.02	-0.7
H_ol	-	-	0.435
O_water	89.516	3.097	-
H_water	-	-	0.241
Dummy_water	-	-	-0.241
Cu-BTC			
MOF-Cu	2.518	3.114	1.248
MOF-O	48.19	3.03	-0.624
MOF-C1	47.86	3,47	0.494
MOF-C2	47.86	3.47	0.13
MOF-C3	47.86	3.47	-0.156
MOF-H	7.65	2.85	0.156

Table 3. 3-site Langmuir-Freundlich isotherm fits for adsorption of water in CuBTC at 298 K.

	Site A			Site B			Site C		
	$q_{A,sat}$ / mol kg^{-1}	b_A / Pa$^{-\nu_{iA}}$	ν_A	$q_{B,sat}$ / mol kg^{-1}	b_B / Pa$^{-\nu_{iB}}$	ν_B	$q_{C,sat}$ / mol kg^{-1}	b_C / Pa$^{-\nu_C}$	ν_C
water	22	5.48×10^{-4}	1	22	6.24×10^{-32}	10	10	2.51×10^{-4}	0.6

Table 4. Dual-site Langmuir-Freundlich parameters for adsorption of methanol, ethanol, and 1-propanol, at 298 K in CuBTC.

Adsorbate	Site A			Site B		
	$q_{A,sat}$ mol kg^{-1}	b_{A0} Pa$^{-\nu_A}$	ν_A dimensionless	$q_{B,sat}$ mol kg^{-1}	b_{B0} Pa$^{-\nu_B}$	ν_B dimensionless
methanol	8.4	3.82×10^{-4}	1.03	11.5	9.3×10^{-16}	6.5
ethanol	5	2.29×10^{-3}	0.97	8	6.41×10^{-7}	3.2
1-propanol	8	4.83×10^{-4}	2.7	2	2.07×10^{-2}	0.5

Table 5. Dual-site Langmuir-Freundlich parameters for water/ethanol mixture adsorption at 298 K in CuBTC.

Adsorbate	Site A			Site B		
	$q_{A,sat}$ mol kg^{-1}	b_{A0} $Pa^{-\nu_A}$	ν_A dimensionless	$q_{B,sat}$ mol kg^{-1}	b_{B0} $Pa^{-\nu_B}$	ν_B dimensionless
water	25	5.39×10^{-4}	0.8	5	9.3×10^{-16}	3.5
Total loading of water and ethanol	21	7.55×10^{-4}	0.76	13	1.16×10^{-7}	3.6

Table 6. Dual-site Langmuir-Freundlich parameters for adsorption of water, methanol, and ethanol at 300 K in all-silica FAU zeolite. The fit parameters are based on the CBMC simulations of pure component isotherms presented in earlier work.[54]

Adsorbate	Site A			Site B		
	$q_{A,sat}$ mol kg^{-1}	b_{A0} Pa$^{-\nu_A}$	ν_A dimensionless	$q_{B,sat}$ mol kg^{-1}	b_{B0} Pa$^{-\nu_B}$	ν_B dimensionless
water	16	1.54×10^{-121}	33	4.6	624×10^{-5}	1
methanol	3.4	6.36×10^{-16}	4.6	5.8	1.68×10^{-4}	1
ethanol	2.5	3.19×10^{-13}	4.9	2.9	1×10^{-3}	1.05

Table 7. Dual-site Langmuir-Freundlich parameters for pure component water, methanol, and ethanol at 300 K in all-silica DDR zeolite. The fit parameters are based on the CBMC simulations of pure component isotherms presented in earlier work.[54] Note that the saturation capacities are specified in molecules per cage; multiply these by 0.832157 to obtain the values in mol per kg framework.

	Site A			Site B		
	$\Theta_{i,A,sat}$ Molecules cage^{-1}	$b_{i,A}$ $Pa^{-\nu_i}$	$\nu_{i,A}$ dimensionless	$\Theta_{i,B,sat}$ molecules cage^{-1}	$b_{i,B}$ $Pa^{-\nu_i}$	$\nu_{i,B}$ dimensionless
water	8.083	3.85×10^{-16}	4	2.667	1.73×10^{-5}	1
methanol	2.1667	1.49×10^{-4}	1.25	1.9167	6×10^{-4}	0.77
ethanol	1.8167	7.66×10^{-3}	1	0.775	8.59×10^{-6}	1

Table 8. Dual-site Langmuir-Freundlich parameters for adsorption of water, methanol, and ethanol at 300 K in all-silica MFI zeolite. The fit parameters are based on CBMC simulations of Krishna and van Baten.[54]

Adsorbate	Site A			Site B		
	$q_{A,sat}$ mol kg^{-1}	b_{A0} Pa$^{-\nu_A}$	ν_A dimensionless	$q_{B,sat}$ mol kg^{-1}	b_{B0} Pa$^{-\nu_B}$	ν_B dimensionless
water	6.7	6.37×10^{-24}	6.2	3.6	1.09×10^{-5}	1.04
methanol	2.4	1×10^{-4}	1.64	1.4	1.92×10^{-3}	0.7
ethanol	1.1	2.82×10^{-4}	2.7	1.7	1.91×10^{-2}	0.9

Table 9. Dual-Langmuir-Freundlich fits of the isotherms of water, and ethanol in LTA-4A zeolite. The isotherm fits are based on the experimental data of Pera-Titus et al.[56]

$$q = q_{A,sat}\frac{b_A p_i^{\nu_A}}{1+b_A p_i^{\nu_A}} + q_{B,sat}\frac{b_B p_i^{\nu_B}}{1+b_B p_i^{\nu_B}}$$ with T-dependent parameters b_A, and b_B

$$b_A = b_{A0}\exp\left(\frac{E_A}{RT}\right); \quad b_B = b_{B0}\exp\left(\frac{E_B}{RT}\right)$$

The isotherm fitting details are provided in our earlier work. [71]

	Site A				Site B			
	$q_{A,sat}$ mol kg^{-1}	b_{A0} Pa$^{-\nu_i}$	E_A kJ mol^{-1}	ν_A dimensionless	$q_{B,sat}$ mol kg^{-1}	b_{B0} Pa$^{-\nu_i}$	E_B kJ mol^{-1}	ν_B dimensionless
water	2.1	2.1×10^{-60}	269	7.26	9.7	5.81×10^{-8}	33	0.83
ethanol	1.85	5.24×10^{-13}	43.3	1.9	1.4	2.65×10^{-10}	40	1.7

Table 10. Wilson non-ideality parameters for mixtures of water and 1-alcohols in CuBTC at 298 K.

	Λ_{12}	Λ_{21}
water/methanol	2	20
water/ethanol	3	60
water/1-propanol	4	80
methanol/ethanol	2	4
methanol/1-propanol	2	6
ethanol/1-propanol	4	6

16. References

(1) Doherty, M. F.; Malone, M. F. Conceptual Design of Distillation Systems; McGraw-Hill: New York, 2001.

(2) Taylor, R.; Krishna, R.; Kooijman, H. Real-World Modeling of Distillation, *Chem. Eng. Prog.* **2003**, *99 (7)*, 28-39.

(3) Springer, P. A. M.; Baur, R.; Krishna, R. Composition trajectories for heterogeneous azeotropic distillation in a bubble-cap tray column: Influence of mass transfer, *Chem. Eng. Res. Des.* **2003**, *81*, 413-426.

(4) Springer, P. A. M.; Buttinger, B.; Baur, R.; Krishna, R. Crossing of the distillation boundary in homogeneous azeotropic distillation: Influence of interphase mass transfer, *Ind. Eng. Chem. Res.* **2002**, *41*, 1621-1631.

(5) Krishna, R. Separating Mixtures by Exploiting Molecular Packing Effects in Microporous Materials, *Phys. Chem. Chem. Phys.* **2015**, *17*, 39-59.

(6) Jeong, J.-S.; Jeon, H.; Ko, K.-M.; Chung, B.; Choi, G.-W. Production of Anhydrous Ethanol using various PSA (Pressure Swing Adsorption) Processes in Pilot Plant, *Renewable Energy* **2012**, *42*, 41-45.

(7) Kumar, S.; Singh, N.; Prasad, R. Anhydrous Ethanol: A Renewable Source of Energy, *Renewable Sustainable Energy Rev.* **2010**, *14*, 1830-1834.

(8) Zhang, K.; Lively, R. P.; Dose, M. E.; Brown, A. J.; Zhang, C.; Chung, J.; Nair, S.; Koros, W. J.; Chance, R. R. Alcohol and Water Adsorption in Zeolitic Imidazolate Frameworks, *Chem. Commun.* **2013**, *49*, 3245-3247.

(9) Saint-Remi, J. C.; Rémy, T.; van Huskeren, V.; van de Perre, S.; Duerinck, T.; Maes, M.; De Vos, D. E.; Gobechiya, E.; Kirschhock, C. E. A.; Baron, G. V.; Denayer, J. F. M. Biobutanol Separation with the Metal–Organic Framework ZIF-8, *ChemSusChem* **2011**, *4*, 1074-1077.

(10) Williams, D. B. G.; Lawton, M. Drying of Organic Solvents: Quantitative Evaluation of the Efficiency of Several Desiccants, *J. Org. Chem.* **2010**, *75*, 8351-8354.

(11) Plessius, R.; Kromhout, R.; Ramos, A. L. D.; Ferbinteanu, M.; Mittelmeijer-Hazeleger, M. C.; Krishna, R.; Rothenberg, G.; Tanase, S. Highly Selective Water Adsorption in a Lanthanum Metal-Organic Framework, *Chem. Eur. J.* **2014**, *20*, 7922-7925.

(12) Uchida, S.; Mizuno, N. Zeotype Ionic Crystal of $Cs_5[Cr_3O(OOCH)_6(H_2O)_3][\alpha\text{-}CoW_{12}O_{40}]\text{-}7.5H_2O$ with Shape-Selective Adsorption of Water, *J. Am. Chem. Soc.* **2004**, *126*, 1602-1603.

(13) Krishna, R. The Maxwell-Stefan Description of Mixture Diffusion in Nanoporous Crystalline Materials, *Microporous Mesoporous Mater.* **2014**, *185*, 30-50.

(14) Krishna, R.; van Baten, J. M. Entropy-based Separation of Linear Chain Molecules by Exploiting Differences in the Saturation Capacities in Cage-type Zeolites, *Sep. Purif. Technol.* **2011**, *76*, 325-330.

(15) Remy, T.; Saint-Remi, J. C.; Singh, R.; Webley, P. A.; Baron, G. V.; Denayer, J. F. M. Adsorption and Separation of C1-C8 Alcohols on SAPO-34, *J. Phys. Chem. C* **2011**, *115*, 8117-8125.

(16) Van der Perre, S.; Van Assche, T.; Bozbiyik, B.; Lannoeye, J.; De Vos, D. E.; Baron, G. V.; Denayer, J. F. M. Adsorptive Characterization of the ZIF-68 Metal-Organic Framework: A Complex Structure with Amphiphilic Properties., *Langmuir* **2014**, *30*, 8416-8424.

(17) Efthymiou, C. G.; Kyprianidou, E. J.; Milios, C. J.; Manos, M. J.; Tasiopoulos, A. J. Flexible lanthanide MOFs as highly selective and reusable liquid MeOH sorbents, *J. Mater. Chem. A* **2013**, *1*, 5061-5069.

(18) Krishna, R.; van Baten, J. M. Separating n-alkane mixtures by exploiting differences in the adsorption capacity within cages of CHA, AFX and ERI zeolites, *Sep. Purif. Technol.* **2008**, *60*, 315-320.

(19) Titze, T.; Chmelik, C.; Kärger, J.; van Baten, J. M.; Krishna, R. Uncommon Synergy Between Adsorption and Diffusion of Hexane Isomer Mixtures in MFI Zeolite Induced by Configurational Entropy Effects *J. Phys. Chem. C* **2014**, *118*, 2660-2665.

(20) Krishna, R.; van Baten, J. M. In silico screening of metal-organic frameworks in separation applications, *Phys. Chem. Chem. Phys.* **2011**, *13*, 10593-10616.

(21) Krishna, R.; Smit, B.; Vlugt, T. J. H. Sorption-induced Diffusion-selective Separation of Hydrocarbon Isomers Using Silicalite, *J. Phys. Chem. A* **1998**, *102*, 7727-7730.

(22) Vlugt, T. J. H.; Krishna, R.; Smit, B. Molecular Simulations of Adsorption Isotherms for Linear and Branched Alkanes and Their Mixtures in Silicalite, *J. Phys. Chem. B* **1999**, *103*, 1102-1118.

(23) Krishna, R. Exploiting Configurational Entropy Effects for Separation of Hexane Isomers Using Silicalite-1, *Chem. Eng. Res. Des.* **2001**, *79*, 182-194.

(24) Herm, Z. R.; Wiers, B. M.; Van Baten, J. M.; Hudson, M. R.; Zajdel, P.; Brown, C. M.; Maschiocchi, N.; Krishna, R.; Long, J. R. Separation of Hexane Isomers in a Metal-Organic Framework with Triangular Channels *Science* **2013**, *340*, 960-964.

(25) Torres-Knoop, A.; Balestra, S. R. G.; Krishna, R.; Calero, S.; Dubbeldam, D. Entropic Separations of Mixtures of Aromatics by Selective Face-to-Face Molecular Stacking in One-Dimensional Channels of Metal–Organic Frameworks and Zeolites, *ChemPhysChem* **2015**, *16*, 532-535.

(26) Torres-Knoop, A.; Krishna, R.; Dubbeldam, D. Separating Xylene Isomers by Commensurate Stacking of p-Xylene within Channels of MAF-X8, *Angew. Chem. Int. Ed.* **2014**, *53*, 7774-7778.

(27) Alaerts, L.; Kirschhock, C. E. A.; Maes, M.; van der Veen, M.; Finsy, V.; Depla, A.; Martens, J. A.; Baron, G. V.; Jacobs, P. A.; Denayer, J. F. M.; De Vos, D. Selective Adsorption and Separation of Xylene Isomers and Ethylbenzene with the Microporous Vanadium(IV) Terephthalate MIL-47, *Angew. Chem. Int. Ed.* **2007**, *46*, 4293-4297.

(28) El Osta, R.; Carlin-Sinclair, A.; Guillou, N.; Walton, R. I.; Vermoortele, F.; Maes, M.; De Vos, D.; Millange, F. Liquid-Phase Adsorption and Separation of Xylene Isomers by the Flexible Porous Metal−Organic Framework MIL-53(Fe), *Chem. Mater.* **2012**, *24*, 2781-2791.

(29) Finsy, V.; Verelst, H.; Alaerts, L.; De Vos, D.; Jacobs, P. A.; Baron, G. V.; Denayer, J. F. M. Pore-Filling-Dependent Selectivity Effects in the Vapor-Phase Separation of Xylene Isomers on the Metal-Organic Framework MIL-47, *J. Am. Chem. Soc.* **2008**, *130*, 7110-7118.

(30) Remy, T.; Baron, G. V.; Denayer, J. F. M. Modeling the Effect of Structural Changes during Dynamic Separation Processes on MOFs, *Langmuir* **2011**, *27*, 13064-13071.

(31) Niekiel, F.; Lannoeye, J.; Reinsch, H.; Munn, A. S.; Heerwig, A.; Zizak, I.; Kaskel, S.; Walton, R. I.; de Vos, D.; Llewellyn, P.; Lieb, A.; Maurin, G.; Stock, N. Conformation-Controlled Sorption Properties and Breathing of the Aliphatic Al-MOF [Al(OH)(CDC)], *Inorg. Chem.* **2012**, *53*, 4610-4620.

(32) Chiang, A. S. T.; Lee, C.-K.; Chang, Z.-H. Adsorption and diffusion of aromatics in $AlPO_4$-5, *Zeolites* **1991**, *11*, 380-386.

(33) Mukherjee, S.; Joarder, B.; Manna, B.; Desai, A. V.; Chaudhari, A. K.; Ghosh, S. K. Framework-Flexibility Driven Selective Sorption of p-Xylene over Other Isomers by a Dynamic Metal-Organic Framework, *Sci. Rep.* **2014**, *4*, 5761. http://dx.doi.org/10.1038/srep05761

(34) Peng, Y.; Zhang, Z.; Zheng, X.; Wang, H.; Xu, C.; Xiao, Q.; Zhong, Y.; Zhu, W. Comparison Study on the Adsorption of CFC-115 and HFC-125 on Activated Carbon and Silicalite-1, *Ind. Eng. Chem. Res.* **2010**, *49*, 10009-10015.

(35) Nalaparaju, A.; Zhao, X. S.; Jiang, J. W. Molecular Understanding for the Adsorption of Water and Alcohols in Hydrophilic and Hydrophobic Zeolitic Metal-Organic Frameworks, *J. Phys. Chem. C* **2010**, *114*, 11542-11550.

(36) Lively, R. P.; Dose, M. E.; Thompson, J. A.; McCool, B. A.; Chance, R. R.; Koros, W. J. Ethanol and Water Adsorption in Methanol-derived ZIF-71, *Chem. Commun.* **2011**, *47*, 8667-8669.

(37) Chui, S. S. Y.; Lo, S. M. F.; Charmant, J. P. H.; Orpen, A. G.; Williams, I. D. A Chemically Functionalizable Nanoporous Material $[Cu_3(TMA)_2(H2O)_3]_n$, *Science* **1999**, *283*, 1148-1150.

(38) Yang, Q.; Zhong, C. Electrostatic-Field-Induced Enhancement of Gas Mixture Separation in Metal-Organic Frameworks: A Computational Study, *ChemPhysChem* **2006**, *7*, 1417-1421.

(39) Rick, S. W. A Reoptimization of the Five-site Water Potential (TIP5P) for use with Ewald Sums, *J. Chem. Phys.* **2004**, *120*, 6085-6093.

(40) Castillo, J. M.; Vlugt, T. J. H.; Calero, S. Understanding Water Adsorption in Cu-BTC Metal-Organic Frameworks, *J. Phys. Chem. C* **2008**, *112*, 15934-15939.

(41) Peng, X.; Lin, L.-C.; Sun, W.; Smit, B. Water Adsorption in Metal–Organic Frameworks with Open-Metal Sites, *A.I.Ch.E.J.* **2015**, *61*, 677-687.

(42) Chen, B.; Potoff, J. J.; Siepmann, J. I. Monte Carlo Calculations for Alcohols and Their Mixtures with Alkanes. Transferable Potentials for Phase Equilibria. 5. United-Atom Description of Primary, Secondary, and Tertiary Alcohols, *J. Phys. Chem. B* **2001**, *105*, 3093-3104.

(43) Mayo, S. L.; Olafson, B. D.; Goddard, W. A. DREIDING: A Generic Force Field for Molecular Simulations, *J. Phys. Chem.* **1990**, *94*, 8897-8909.

(44) Rappé, A. K.; Casewit, C. J.; Colwel, K. S.; Goddard, W. A.; Skiff, W. M. UFF, A Full Periodic Table Force Field for Molecular Mechanics and Molecular Dynamics Simulations, *J. Am. Chem. Soc.* **1992**, *114*, 10024-10035.

(45) Zang, J.; Nair, S.; Sholl, D. S. Prediction of Water Adsorption in Copper-Based Metal−Organic Frameworks Using Force Fields Derived from Dispersion-Corrected DFT Calculations, *J. Phys. Chem. C* **2013**, *117*, 7519-7525.

(46) Gutierrez-Sevillano, J. J.; Dubbeldam, D.; Bellarosa, L.; Lopez, N.; Liu, X.; Calero, S. Strategies to Simultaneously Enhance the Hydrostability and the Alcohol-Water Separation Behavior of Cu-BTC, *J. Phys. Chem. C* **2013**, *117*, 20706-20714.

(47) Gutierrez-Sevillano, J. J.; Vincent-Luna, J. M.; Dubbeldam, D.; Calero, S. Molecular Mechanisms for Adsorption in Cu-BTC Metal Organic Framework, *J. Phys. Chem. C* **2013**, *117*, 11357-11366.

(48) Calero, S.; Gómez-Álvarez, P. Insights into the Adsorption of Water and Small Alcohols on the Open-Metal Sites of Cu-BTC via molecular simulation, *J. Phys. Chem. C* **2015**, *119*, 467-472.

(49) Zhao, Z.; Wang, S.; Yang, Y.; Li, X.; Li, J.; Li, Z. Competitive Adsorption and Selectivity of Benzene and Water Vapor on the Microporous Metal Organic Frameworks (HKUST-1), *Chem. Eng. J.* **2015**, *259*, 79-89.

(50) Yazaydın, A. Ö.; Benin, A. I.; Faheem, S. A.; Jakubczak, P.; Low, J. J.; Willis, R. R.; Snurr, R. Q. Enhanced CO_2 Adsorption in Metal-Organic Frameworks via Occupation of Open-Metal Sites by Coordinated Water Molecules, *Chem. Mater.* **2009**, *21*, 1425-1430.

(51) Küsgens, P.; Rose, M.; Senkovska, I.; Fröde, H.; Henschel, A.; Siegle, S. Characterization of Metal-Organic Frameworks by Water Adsorption, *Microporous Mesoporous Mater.* **2009**, *120*, 325-330.

(52) Van Assche, T. R. C.; Duerinck, T.; Gutiérrez Sevillano, J. J.; Calero, S.; Baron, G. V.; Denayer, J. F. M. High Adsorption Capacities and Two-Step Adsorption of Polar Adsorbates on Copper- Benzene-1,3,5-tricarboxylate Metal-Organic Framework, *J. Phys. Chem. C* **2013**, *117*, 18100-18111.

(53) Myers, A. L.; Prausnitz, J. M. Thermodynamics of Mixed Gas Adsorption, *A.I.Ch.E.J.* **1965**, *11*, 121-130.

(54) Krishna, R.; van Baten, J. M. Hydrogen Bonding Effects in Adsorption of Water-alcohol Mixtures in Zeolites and the Consequences for the Characteristics of the Maxwell-Stefan Diffusivities, *Langmuir* **2010**, *26*, 10854-10867.

(55) Ruthven, D. M. Principles of Adsorption and Adsorption Processes; John Wiley: New York, 1984.

(56) Pera-Titus, M.; Fité, C.; Sebastián, V.; Lorente, E.; Llorens, J.; Cunill, F. Modeling Pervaporation of Ethanol/Water Mixtures within 'Real' Zeolite NaA Membranes, *Ind. Eng. Chem. Res.* **2008**, *47*, 3213-3224.

(57) Pluth, J. J.; Smith, J. V. Accurate redetermination of crystal structure of dehydrated zeolite A. Absence of near zero coordination of sodium. Refinement of silicon,aluminum-ordered superstructure, *J. Am. Chem. Soc.* **1980**, *102*, 4704-4708.

(58) García-Sánchez, A.; García-Pérez, E.; Dubbeldam, D.; Krishna, R.; Calero, S. A Simulation Study of Alkanes in Linde Type A Zeolites, *Adsorpt. Sci. Technol.* **2007**, *25*, 417-427.

(59) Hedin, N.; DeMartin, G. J.; Roth, W. J.; Strohmaier, K. G.; Reyes, S. C. PFG NMR self-diffusion of small hydrocarbons in high silica DDR, CHA and LTA structures, *Microporous Mesoporous Mater.* **2008**, *109*, 327-334.

(60) Hedin, N.; DeMartin, G. J.; Strohmaier, K. G.; Reyes, S. C. PFG NMR self-diffusion of propylene in ITQ-29, CaA and NaCaA: Window size and cation effects, *Microporous Mesoporous Mater.* **2007**, *98*, 182-188.

(61) Fritzsche, S.; Haberlandt, R.; Kärger, J.; Pfeifer, H.; Heinzinger, K.; Wolfsberg, M. Influence of Exchangeable Cations on the Diffusion of Neutral Diffusants in Zeolites of Type LTA - an MD Study, *Chem. Phys. Lett.* **1995**, *242*, 361-366.

(62) Simo, M.; Sivashanmugam, S.; Brown, C. J.; Hlavacek, V. Adsorption/Desorption of Water and Ethanol on 3A Zeolite in Near-Adiabatic Fixed Bed, *Ind Eng Chem Res* **2009**, *48*, 9257-9260.

(63) Calleja, G.; Jimenez, A.; Pau, J.; Domínguez, L.; Pérez, P. Multicomponent Adsorption Equilibrium of Ethylene, Propane, Propylene and CO_2 on 13X Zeolite, *Gas Sep. Purif.* **1994**, *8*, 247-256.

(64) Talu, O.; Myers, A. L. Rigorous Thermodynamic Treatment of Gas-Adsorption, *A.I.Ch.E.J.* **1988**, *34*, 1887-1893.

(65) Talu, O.; Myers, A. L. Multicomponent Adsorption Equilibria of Nonideal Mixtures, *A.I.Ch.E.J.* **1986**, *32*, 1263-1276.

(66) Siperstein, F. R.; Myers, A. L. Mixed-Gas Adsorption, *A.I.Ch.E.J.* **2001**, *47*, 1141-1159.

(67) Krishna, R.; Long, J. R. Screening metal-organic frameworks by analysis of transient breakthrough of gas mixtures in a fixed bed adsorber, *J. Phys. Chem. C* **2011**, *115*, 12941-12950.

(68) Krishna, R.; Baur, R. Modelling issues in zeolite based separation processes, *Sep. Purif. Technol.* **2003**, *33*, 213-254.

(69) Wu, H.; Yao, K.; Zhu, Y.; Li, B.; Shi, Z.; Krishna, R.; Li, J. Cu-TDPAT, an *rht*-type Dual-Functional Metal–Organic Framework Offering Significant Potential for Use in H_2 and Natural Gas Purification Processes Operating at High Pressures, *J. Phys. Chem. C* **2012**, *116*, 16609-16618.

(70) He, Y.; Krishna, R.; Chen, B. Metal-Organic Frameworks with Potential for Energy-Efficient Adsorptive Separation of Light Hydrocarbons, *Energy Environ. Sci.* **2012**, *5*, 9107-9120.

(71) Krishna, R. Evaluation of Procedures for Estimation of the Isosteric Heat of Adsorption in Microporous Materials, *Chem. Eng. Sci.* **2015**, *123*, 191-196.

17. Caption for Figures

Figure 1. (a) Molar densities of pure water, methanol, ethanol, and 1-propanol as a function of the bulk fluid phase fugacities. (b) Molar densities of equimolar water/ethanol mixtures as a function of the bulk fluid phase fugacity, f_t. These calculations are based on the Peng-Robinson equation of state.

Figure 2. Cage connectivity of CuBTC framework.

Figure 3. Comparison of the CBMC simulations for water adsorption in CuBTC with 3-site Langmuir-Freundlich model. Also shown are the experimental isotherm data of Zhao et al.,[49] Yazaydin et al.,[50] and Küsgens et al.[51] measured at 298 K.

Figure 4. (a) Comparison of the CBMC simulations for adsorption of water, methanol, ethanol, and 1-propanol in CuBTC with multi-site-Langmuir-Freundlich model. (b) Experimental data of van Assche et al.[52] for unary isotherms of water, and alcohols in CuBTC at 323 K.

Figure 5. The fractional occupancy within the pores, θ_i, for each of the four guest molecules as a function of the bulk fluid phase fugacity, f_i.

Figure 6. Average occupation profiles (AOP) of alcohols and water in the Cu-BTC. The data correspond to the quaternary water/methanol/ethanol/1-propanol mixture at 50 kPa. The AOP are superposed to the iso-contour picture of energy landscape of the Cu-BTC framework.

Figure 7. CBMC simulations for equimolar (a) water/methanol, (b) water/ethanol, (c) water/1-propanol, (d) water/methanol/ethanol/1-propanol, and (e) methanol/ethanol mixtures in CuBTC at 298 K.

Figure 8. Adsorption selectivties for equimolar binary mixtures in CuBTC at 298 K.

Figure 9. Comparison of CBMC simulations for equimolar (a) water/methanol, (b) water/ethanol, (c) water/1-propanol, (d) water/methanol/ethanol/1-propanol, and (e) methanol/ethanol mixtures in CuBTC at 298 K with IAST calculations. In these plots the component loadings are represented on the linear *y*-axes.

Figure 10. Comparison of CBMC simulations for equimolar (a) water/methanol, (b) water/ethanol, (c) water/1-propanol, (d) water/methanol/ethanol/1-propanol, and (e) methanol/ethanol mixtures in CuBTC at 298 K with IAST calculations. In these plots the component loadings are represented on the logarthmic *y*-axes.

Figure 11. (a) Comparison of the CBMC simulation data for component loading, q_1, of water in water/ethanol mixture with dual-Langmuir fits using the parameters specified in Table 5. (b)

Comparison of the CBMC simulation data for total mixture loading, q_t, with dual-Langmuir fits using the parameters specified in Table 5.

Figure 12. Activity coefficients of the components in the adsorbed phase for equimolar (a) water/methanol, (b) water/ethanol, (c) water/1-propanol, and (d) methanol/ethanol mixtures in CuBTC at 298 K. Plotted on linear *y*-axis.

Figure 13. Activity coefficients of the components in the adsorbed phase for equimolar (a) water/methanol, (b) water/ethanol, (c) water/1-propanol, and (d) methanol/ethanol mixtures in CuBTC at 298 K. The plots using logarithmic *y*-axis.

Figure 14. CBMC simulations of pure component adsorption isotherms for water, methanol, and ethanol in all-silica FAU zeolite at 300 K. The CBMC data are from Krishna and van Baten.[54] The continuous solid lines are the Dual-Langmuir-Freundlich fits using the parameters specified in Table **6**.

Figure 15. (a, b) CBMC simulations for adsorption of equimolar (f_1=f_2) (a) water/methanol, and (b) water/ethanol in FAU zeolite at 300 K. The continuous solid lines are the IAST calculations using the pure component fits in Table **6**. (c, d) Activity coefficients γ_i, for (c) water/methanol and (d) water/ethanol mixtures.

Figure 16. (a) CBMC simulations for adsorption of water/methanol mixtures in FAU zeolite at 300 K at a constant total fugacity of 1000 Pa. The continuous solid lines are the IAST calculations using the pure component fits in Table **6**. (b) Activity coefficients γ_i, in the mixture.

Figure 17. CBMC simulations of pure component adsorption isotherms for water, methanol, and ethanol in all-silica DDR zeolite at 300 K. The CBMC data are from Krishna and van Baten.[54] The continuous solid lines are the Dual-Langmuir-Freundlich fits using the parameters specified in Table **7**.

Figure 18. (a, b) CBMC simulations for adsorption of equimolar (f_1=f_2) (a) water/methanol, and (b) water/ethanol in DDR zeolite at 300 K. The continuous solid lines are the IAST calculations using the pure component fits in Table **6**. (c, d) Activity coefficients γ_i, for (c) water/methanol and (d) water/ethanol mixtures.

Figure 19. CBMC simulations of pure component adsorption isotherms for water, methanol, and ethanol in all-silica MFI zeolite at 300 K. The CBMC data are from Krishna and van Baten.[54] The continuous solid lines are the Dual-Langmuir-Freundlich fits using the parameters specified in Table **8**.

Figure 20. (a, b) CBMC simulations for adsorption of equimolar (f_1=f_2) (a) water/methanol, and (b) water/ethanol in MFI zeolite at 300 K. The continuous solid lines are the IAST calculations using the pure component fits in Table **8**.

Figure 21. Snapshots showing the location of cations in LTA-5A, and LTA-4A.

Figure 22. (a,b) Experimental data of Pera-Titus et al. [56] for pure component isotherms of (a) water, and (b) ethanol in LTA-4A zeolite at various temperatures. The continuous solid lines are the dual-Langmuir-Freundlich fits of the isotherms using the parameters reported in Table 9.

Figure 23. Comparison of the experimental data of Pera-Titus et al. [56] for component loadings in water/ethanol mixtures in LTA-4A zeolite at 333 K as a function of the vapor phase mole fraction of water. The total pressure in the experiments is 2.1 kPa. The continuous solids lines are IAST calculations using the parameters reported in Table 9.

Figure 24. Comparison of CBMC simulations for equimolar (a) water/methanol, (b) water/ethanol, (c) water/1-propanol, (d) water/methanol/ethanol/1-propanol, and (e) methanol/ethanol mixtures in CuBTC at 298 K with RAST calculations.

Figure 25. RAST calculations of total pore occupancy, θ_t, for adsorption of equmolar water/methanol/ethanol/1-propanol mixtures in CuBTC at 298 K.

Figure 26. Correction factor $\left(1-\exp\left(-C\frac{\pi A}{RT}\right)\right)$ for water/1-propanol mixture adsorption in CuBTC at 298 K. These calculations are based on the equation (20) taking $\Lambda_{12} = 2$; $\Lambda_{21}= 300$; C = 0.1 kg mol^{-1}. These values were obtained by matching the RAST calculations of component loadings with CBMC mixture simulations.

Figure 27. Schematic of a packed bed adsorber.

Figure 28. Transient breakthroughs for equimolar (a) water/methanol, (b) water/ethanol, (c) water/1-propanol, (d) water/methanol/ethanol/1-propanol, and (e) methanol/ethanol mixtures in CuBTC at 298 K, and total fluid phase fugacity of 100 kPa. The *y*-axis represents the concentrations of each component in the exiting fluid phase, normalized with respect to the concentrations in the inlet feed stream. All these simulations use RAST for calculation of mixture adsorption equilibrium.

Figure 29. Transient breakthroughs for 8/92 (a) water/methanol, (b) water/ethanol, and (c) water/1-propanol mixtures in CuBTC at 298 K, and total fluid phase fugacity of 100 kPa. The *y*-axis represents the concentrations of each component in the exiting fluid phase, normalized with respect to the concentrations in the inlet feed stream. All these simulations use RAST for calculation of mixture adsorption equilibrium.

Figure 30. Comparison of the transient breakthroughs for equimolar water/ethanol mixtures in CuBTC at 298 K, and total fluid phase fugacity of (a) 1 kPa, and (b) 100 kPa. For the simulations at 1 kPa, the mixture adsorption equilibrium is determined using the IAST. For 100 kPa operations, we use RAST.

Figure 31. Comparison of the transient breakthroughs for equimolar water/methanol/ethanol/1-propanol mixtures in CuBTC at 298 K, and total fluid phase fugacity of (a) 1 kPa, and (b) 100 kPa. For the

simulations at 1 kPa, the mixture adsorption equilibrium is determined using the IAST. For 100 kPa operations, we use RAST.

Figure 32. Comparison of transient breakthroughs for equimolar water/ethanol mixtures in (a) LTA-4A zeolite at 298 K, and (b) CuBTC. For LTA-4A, the dual-site Langmuir-Freundlich isotherm fit parameters based on re-fitting the experimental data of Pera-Titus[56], are provided in Table 9; further details of the isotherm fits are available in our earlier work.[71] The mixture adsorption equilibrium for LTA-4A is calculated using IAST. For CuBTC, the calculations are based on RAST.

Figure S1

Molar densities of fluids

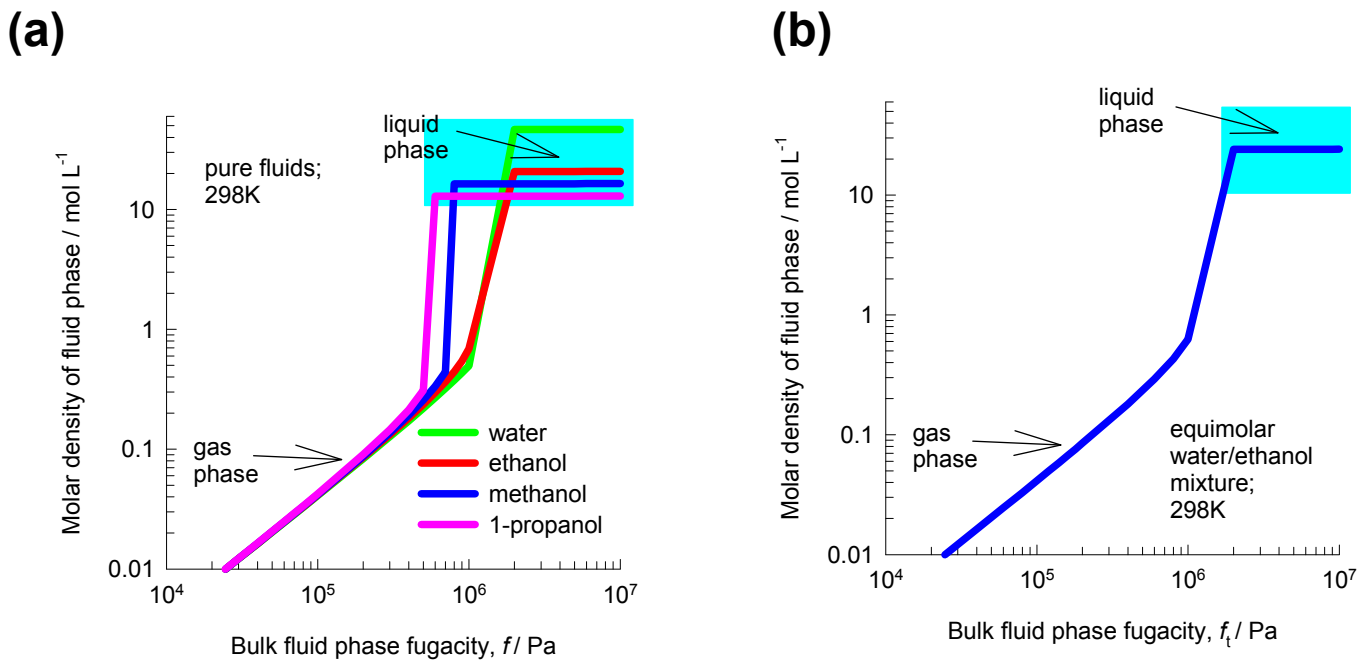

Figure S2

CuBTC framework

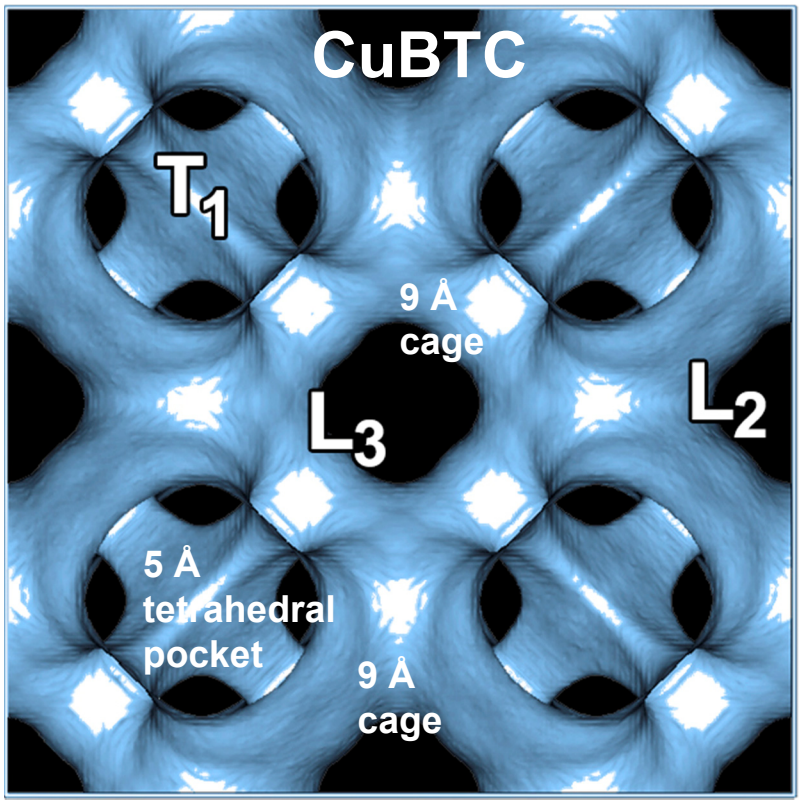

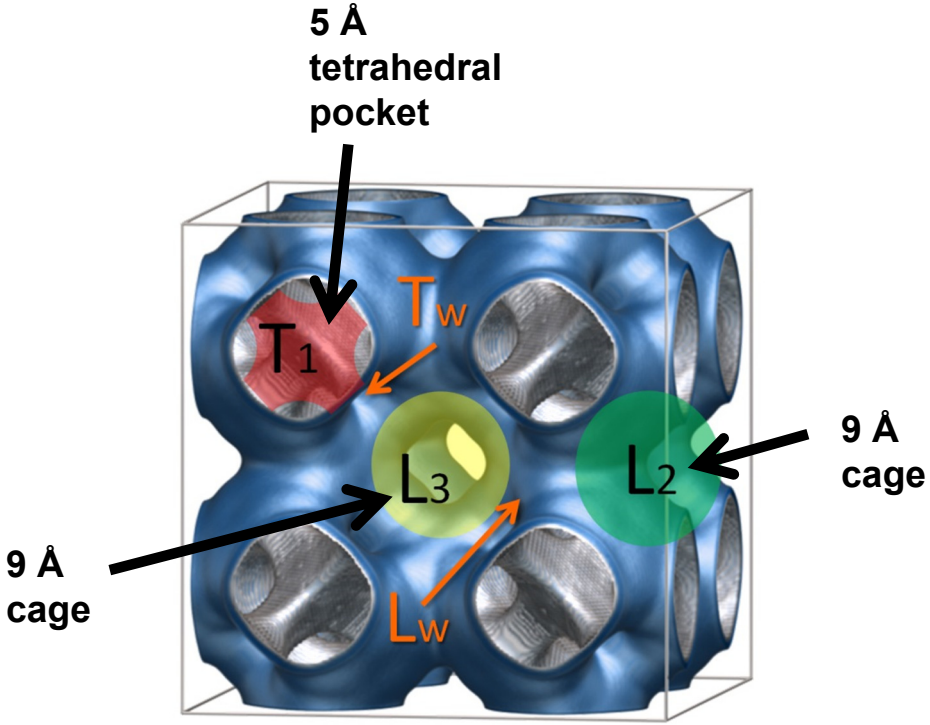

Figure S3

Adsorption of water in CuBTC: validation

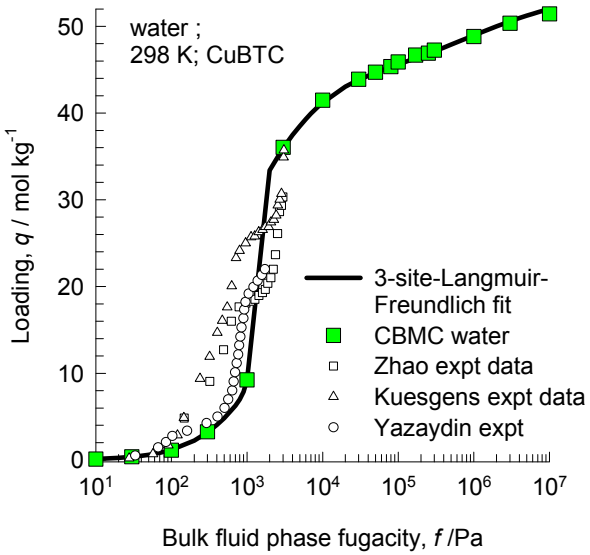

Figure S4

Unary isotherms: water, and 1-alcohols in CuBTC

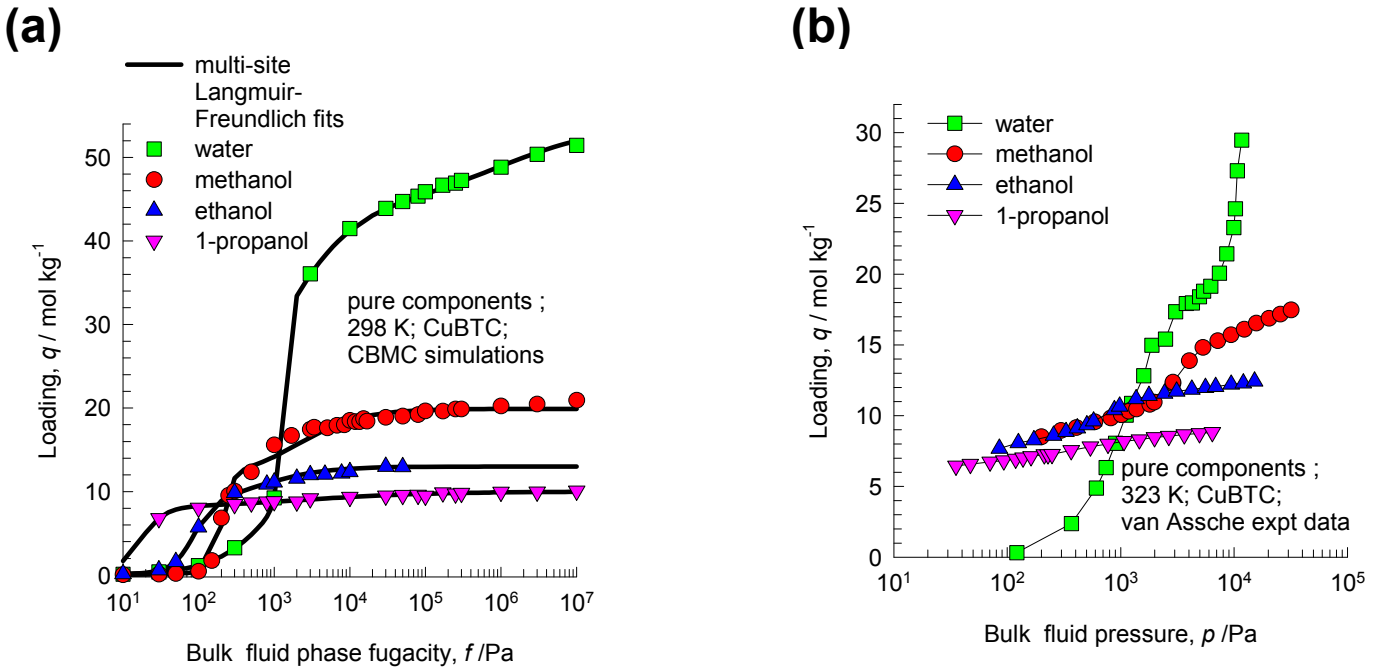

Figure S5

Fractional pore occupancies

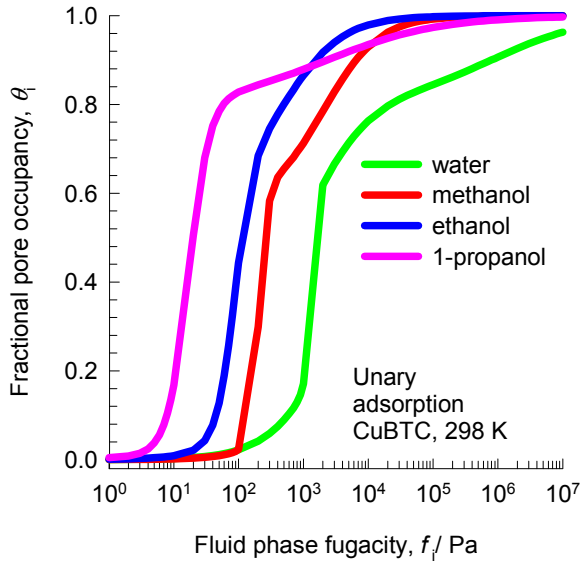

Figure S6

Average occupation profiles (AOP) of alcohols and water in the Cu-BTC. The data correspond to the quaternary mixture at 50 kPa. The AOP are superposed to the isocontour picture of energy landscape of the Cu-BTC framework.

red = methanol

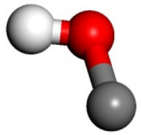

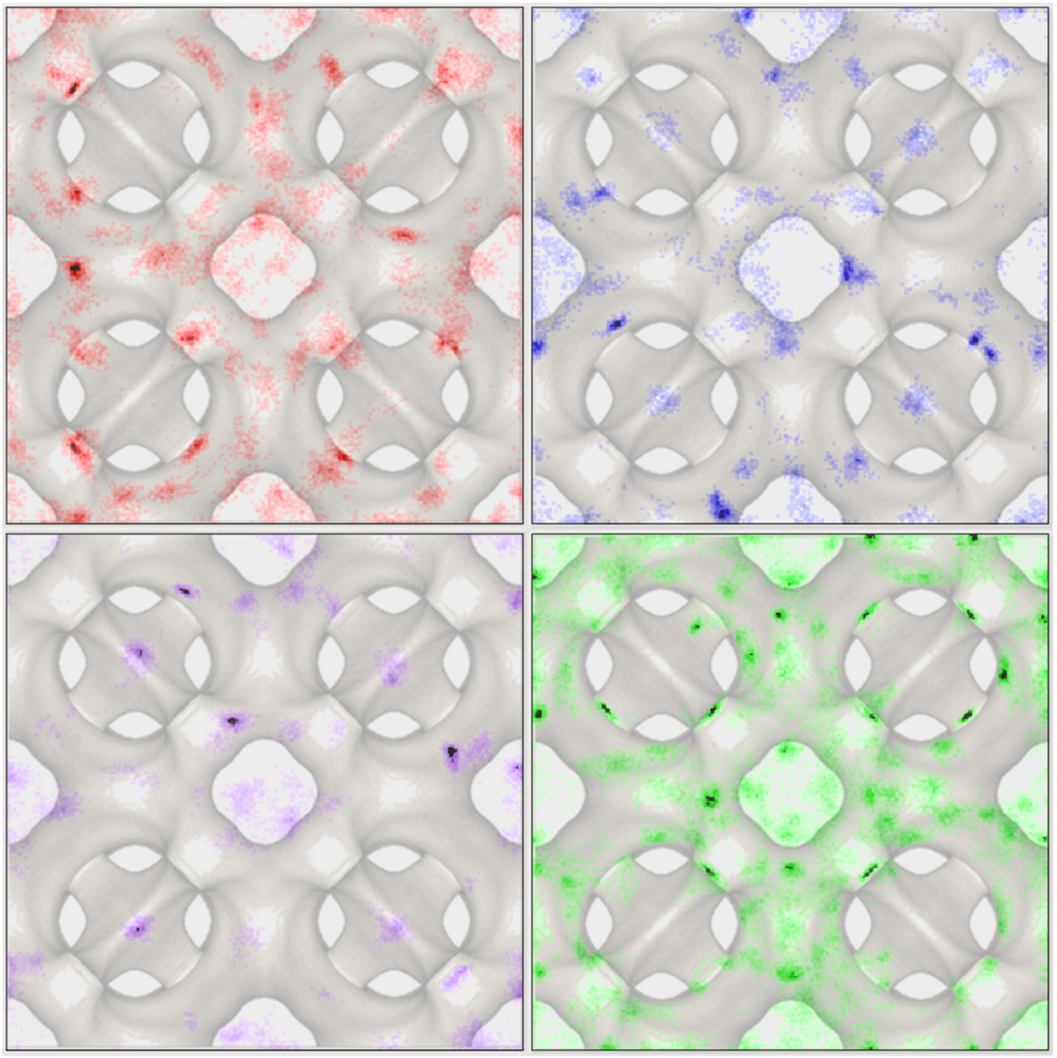

blue = ethanol

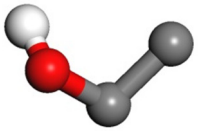

purple = 1-propanol

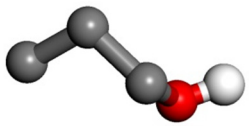

green = water

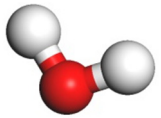

Figure S7

CBMC mixture simulations

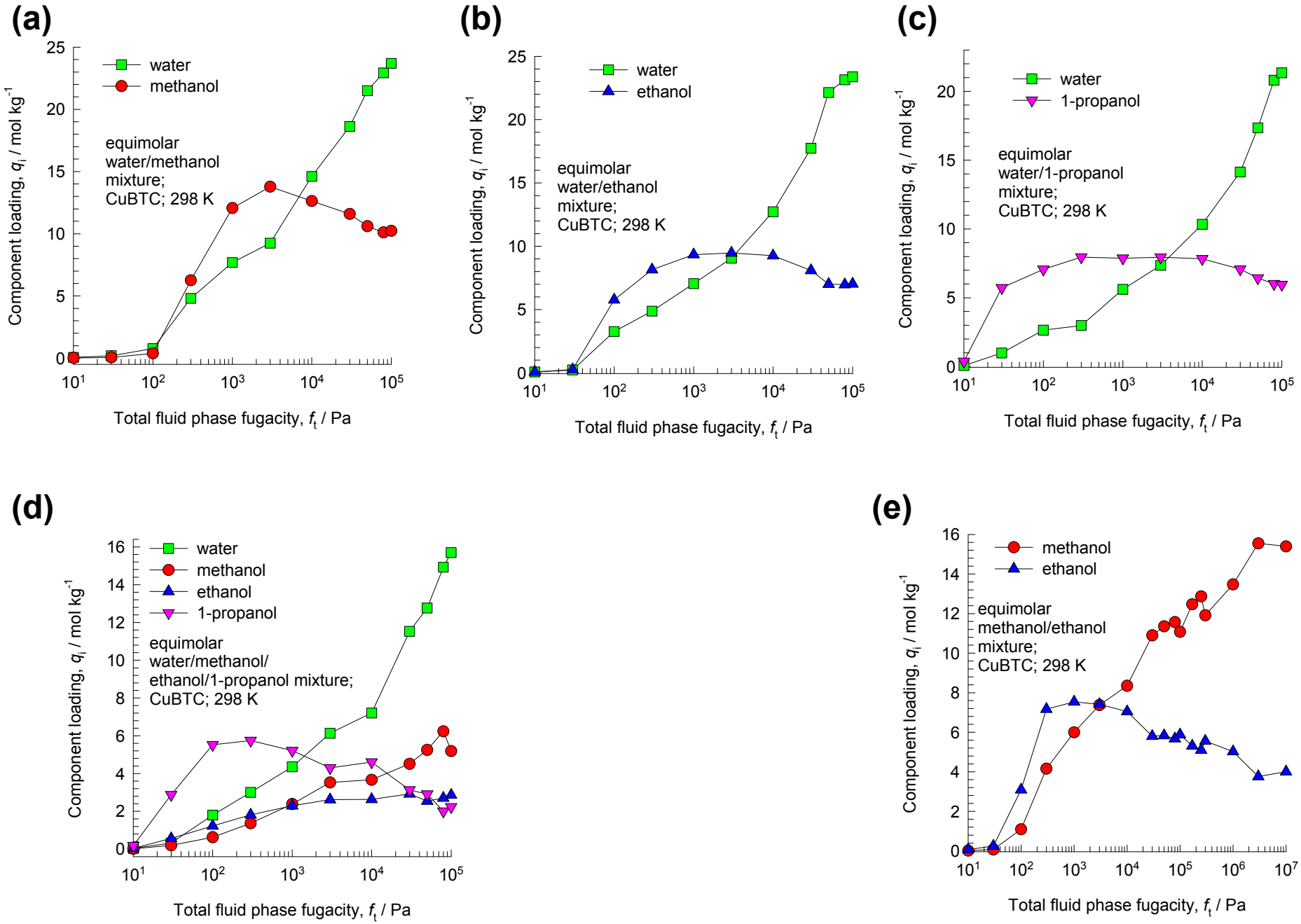

CBMC mixture simulations: Selectivities

Figure S8

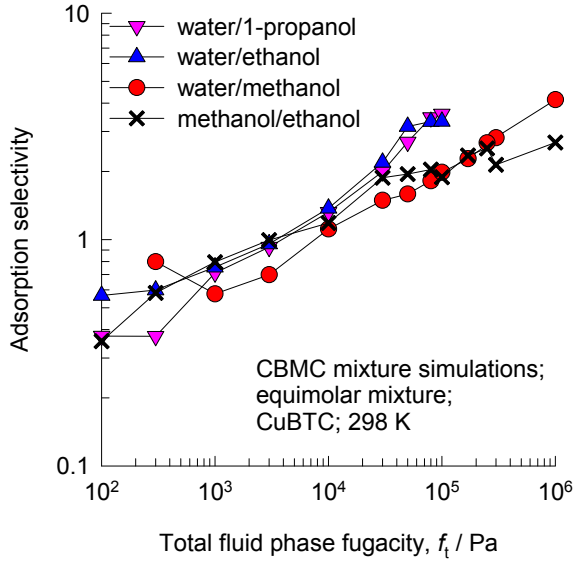

Figure S9

IAST vs CBMC mixture

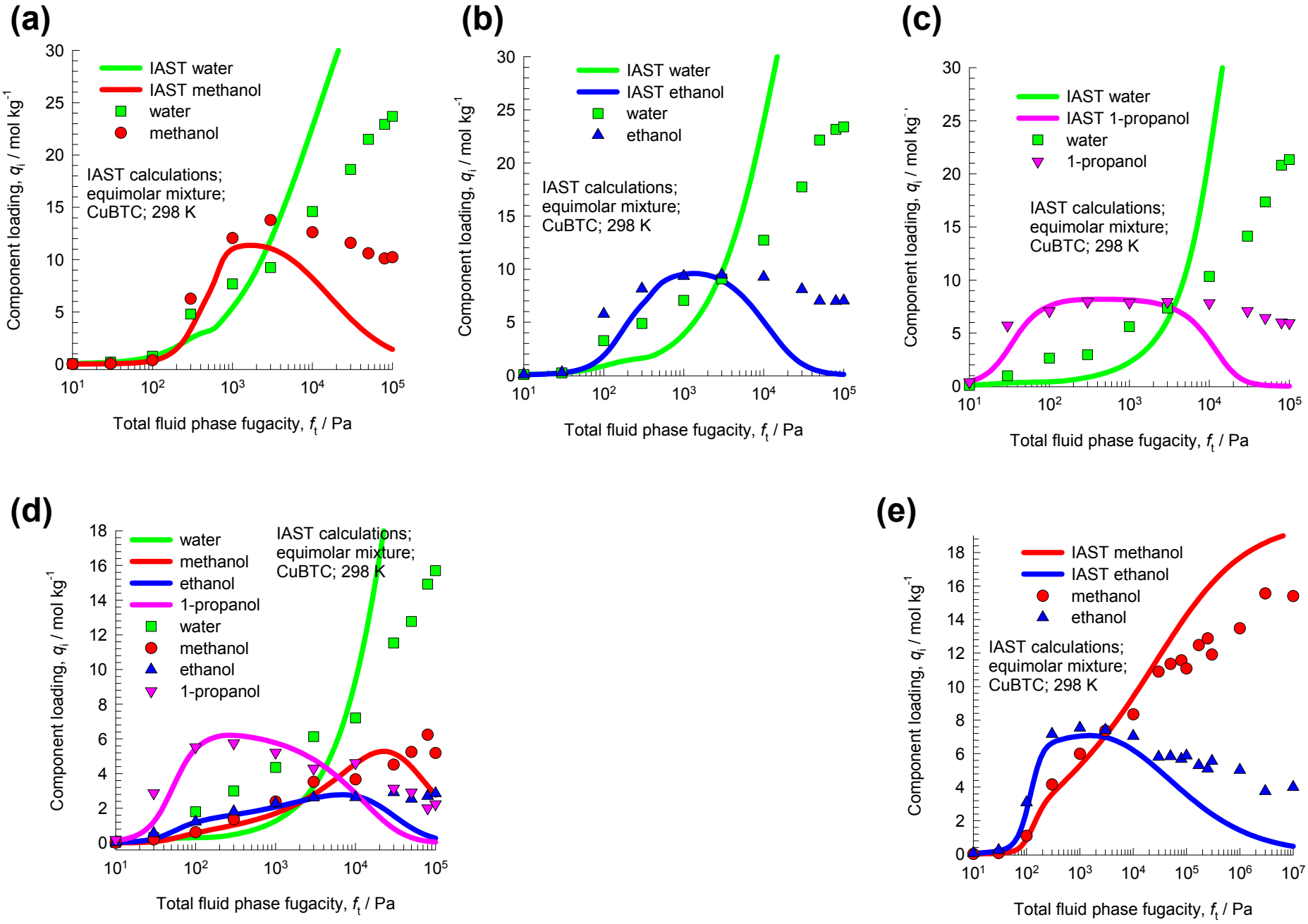

Figure S10

IAST vs CBMC mixture

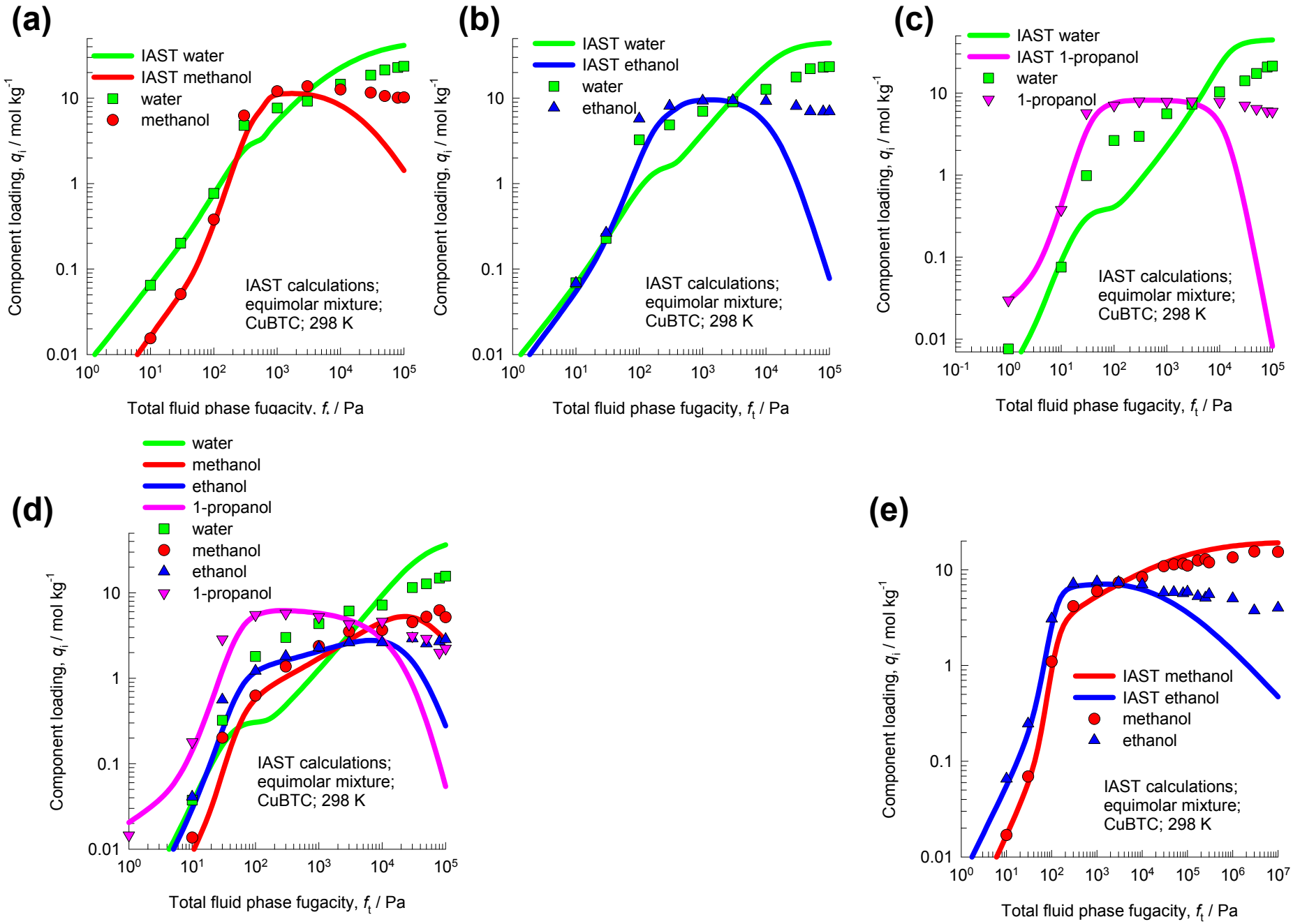

Fitting of CBMC mixture simulation data

Figure S11

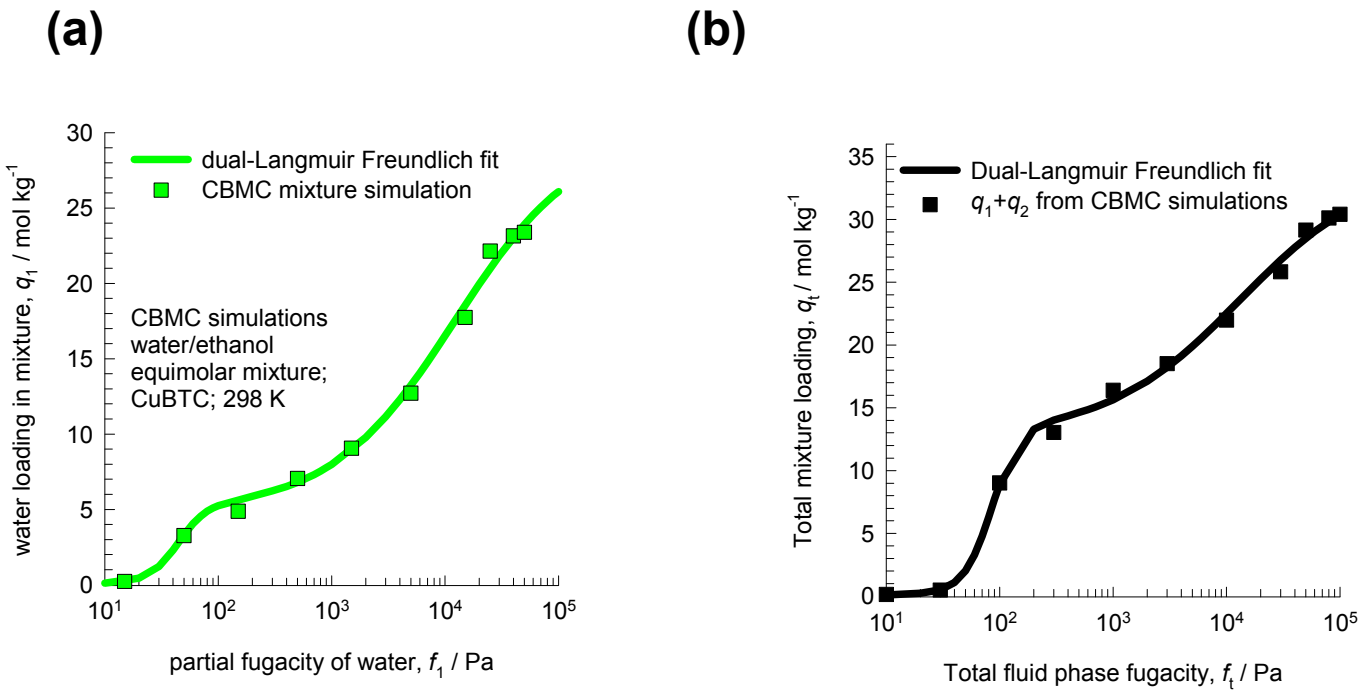

Activity coefficients for water/1-alcohols

Figure S12

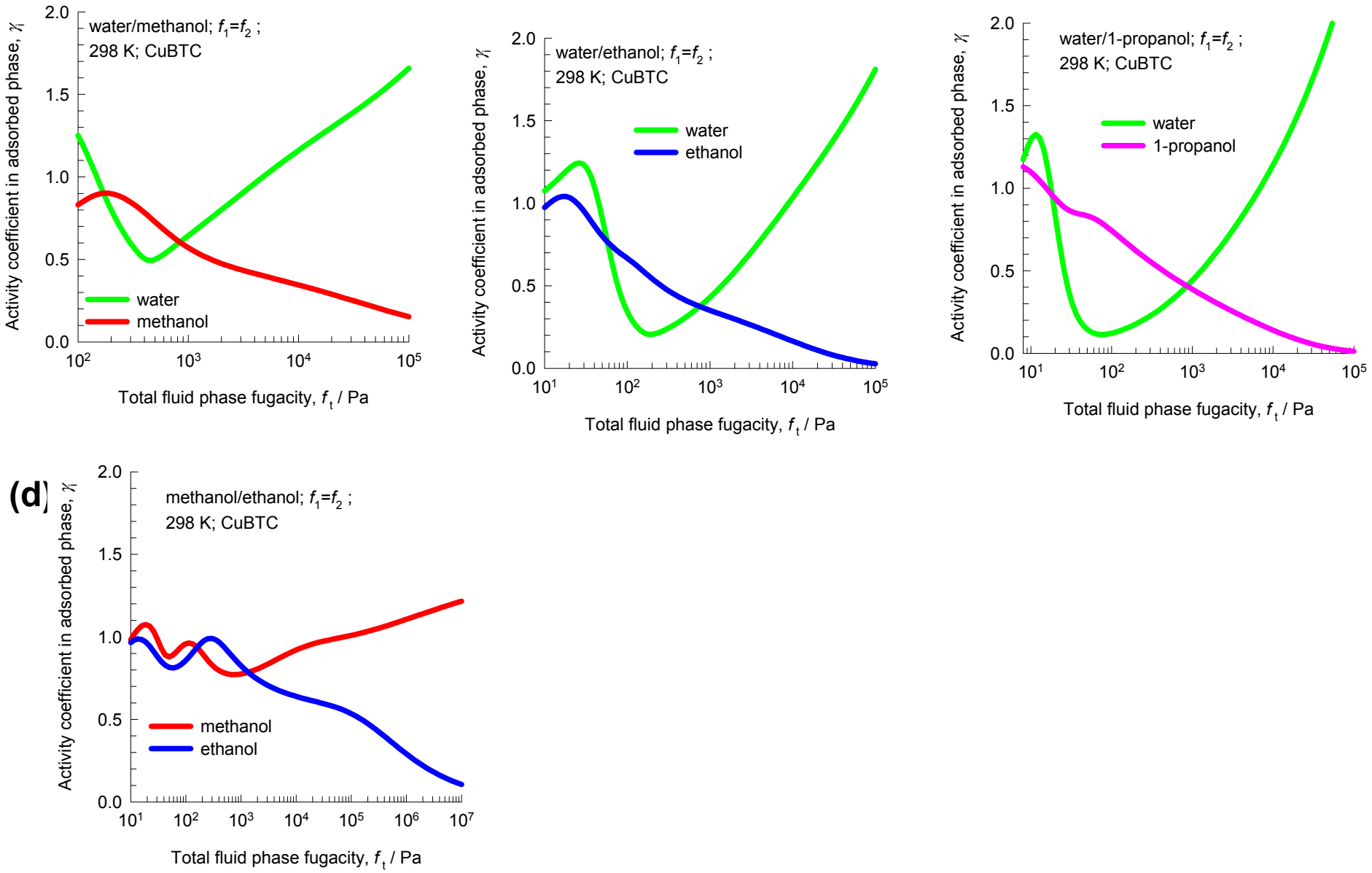

Activity coefficients for water/1-alcohols

Figure S13

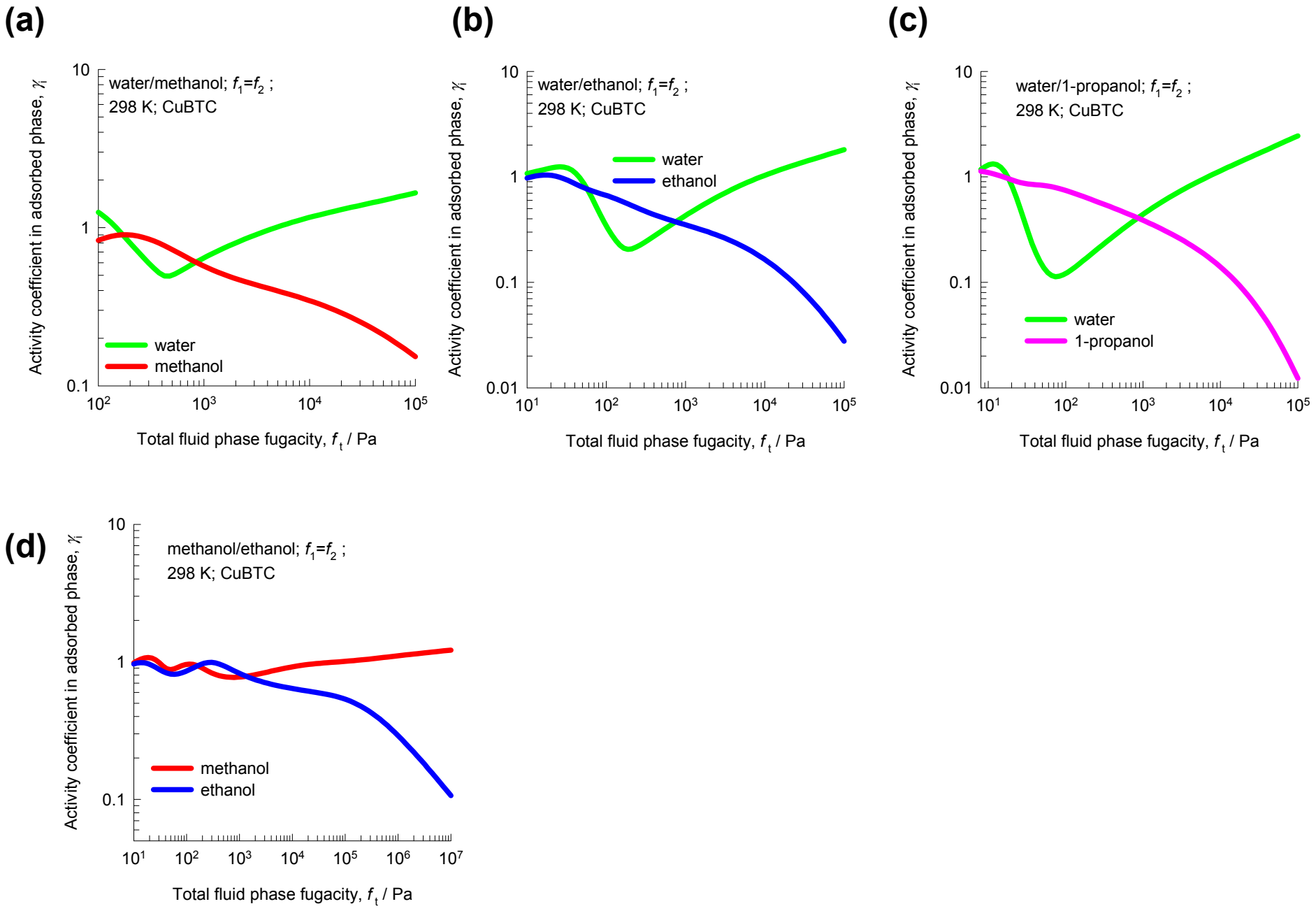

Water, alcohols isotherms in FAU

Figure S14

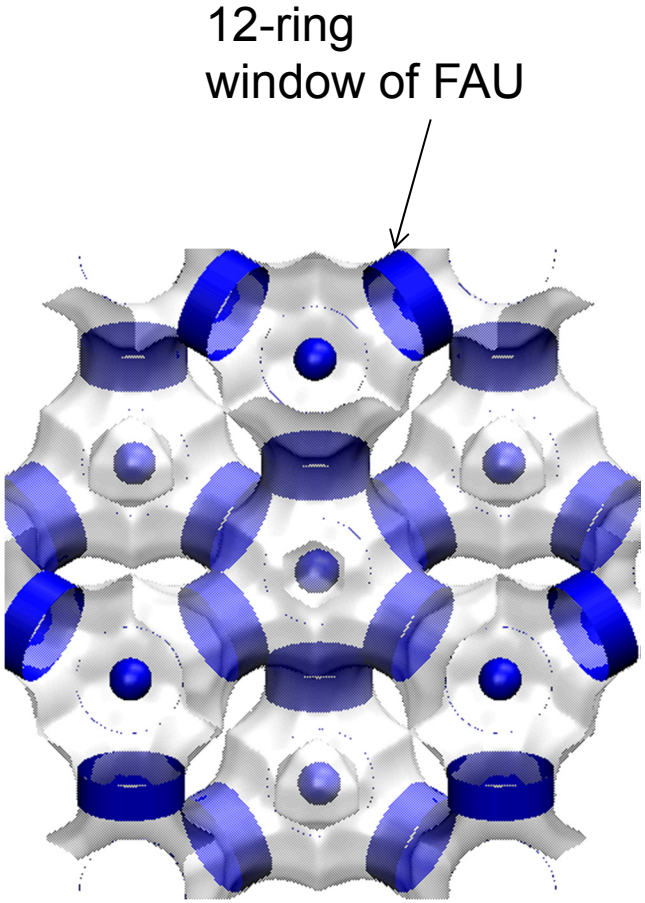

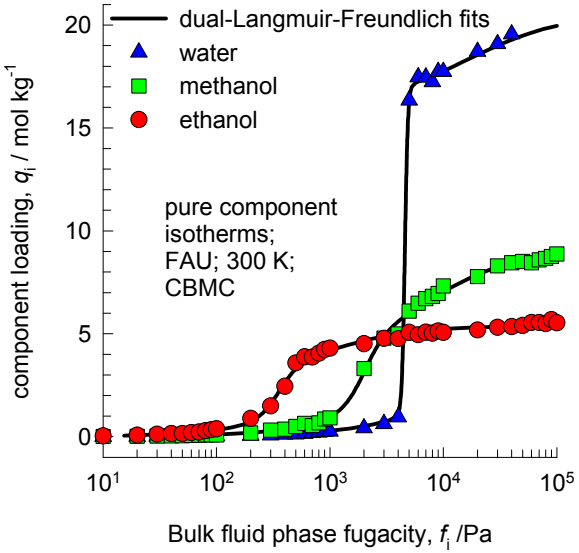

There are 8 cages per unit cell. The volume of one FAU cage is 786 Å^3, larger in size than that of CHA (316.4 Å^3) and DDR (278 Å^3).

Water/alcohols mixture adsorption in FAU

Figure S15

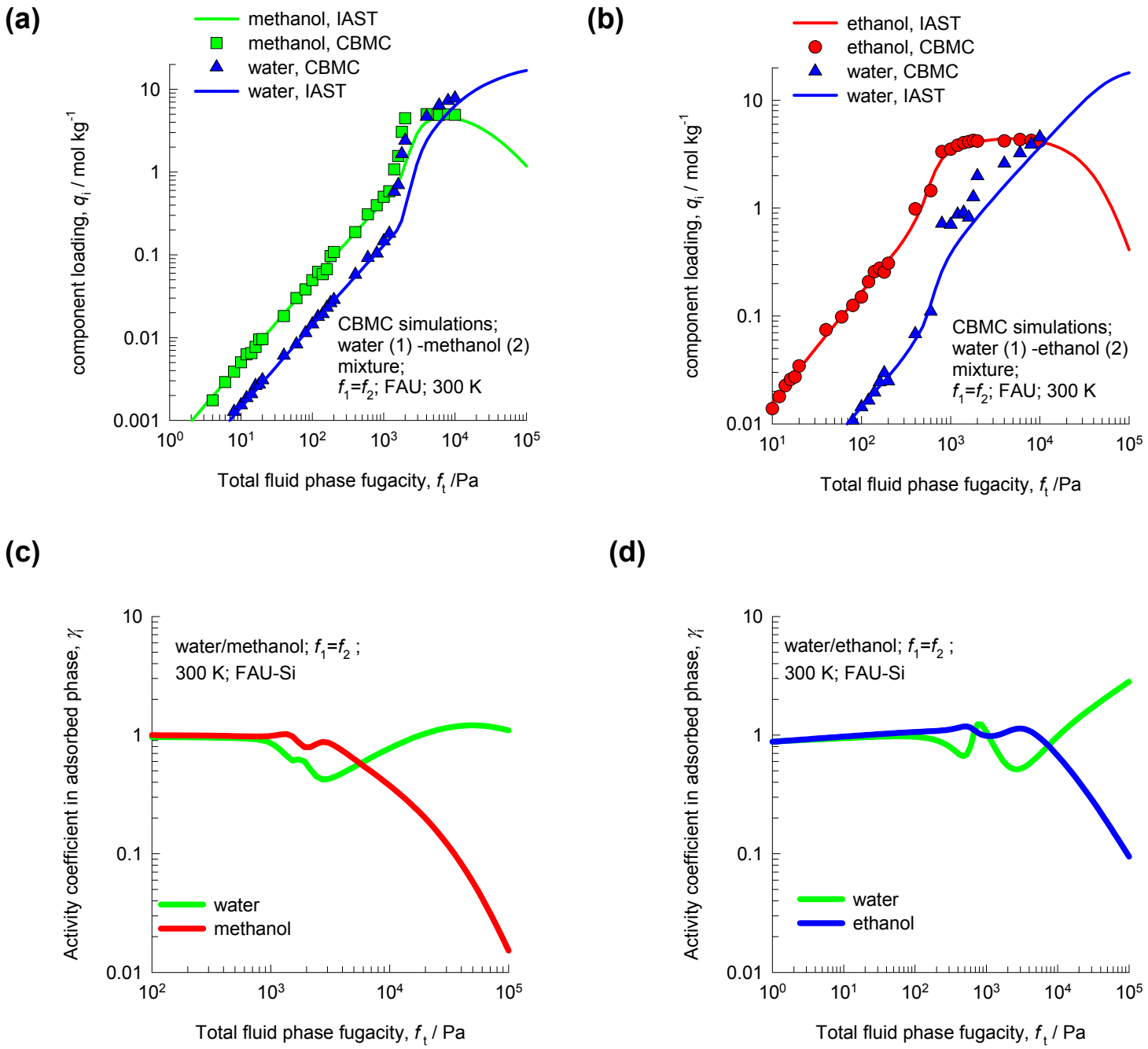

Water/alcohols mixture adsorption in FAU

Figure S16

(a)

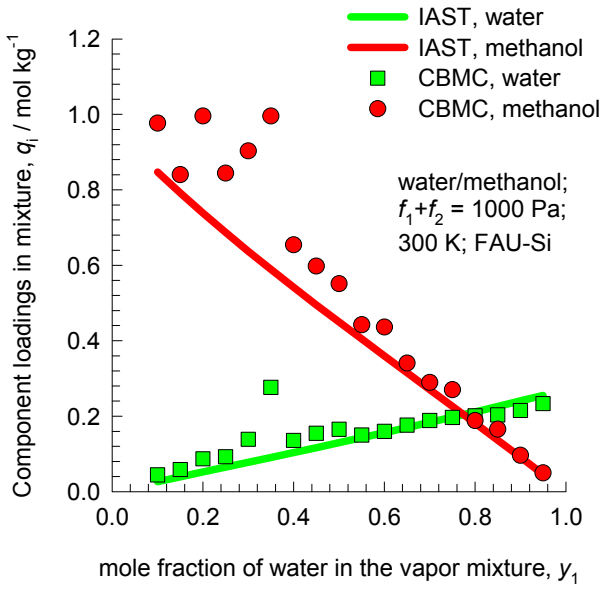

(b)

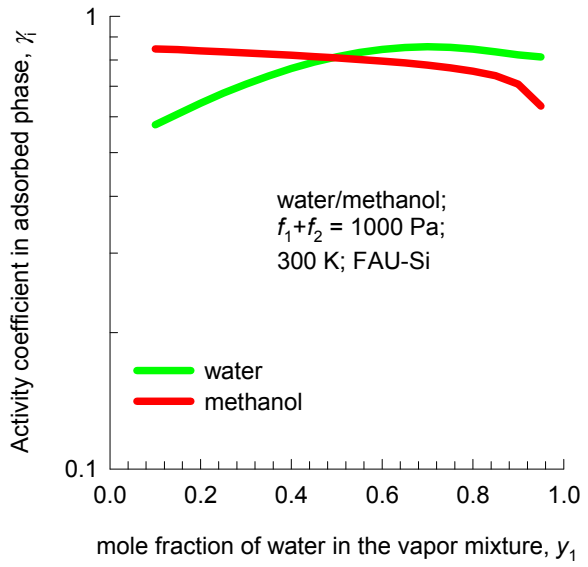

Water, methanol, ethanol isotherms in DDR

Figure S17

There are 12 cages per unit cell. The volume of one DDR cage is 278 Å^3, significantly smaller than that of a single cage of FAU (786 Å^3), or ZIF-8 (1168 Å^3).

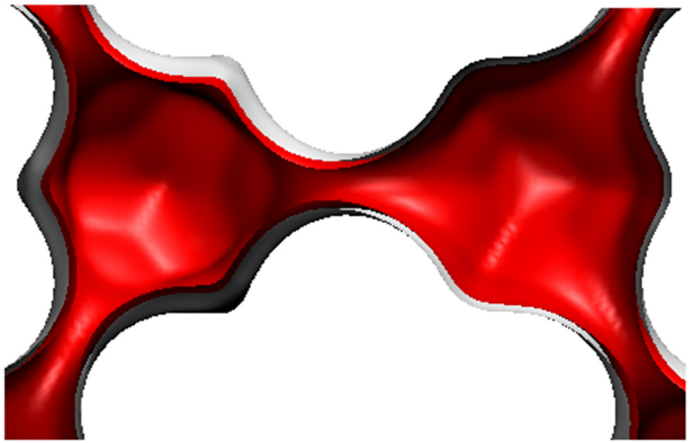

The volume of one DDR cage is 278 Å^3, significantly smaller than that of a single cage of FAU (786 Å^3), or ZIF-8 (1168 Å^3).

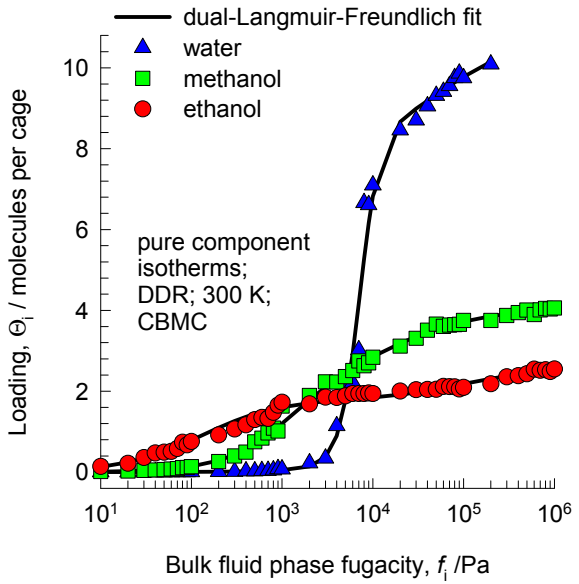

Water/alcohols separations in DDR

Figure S18

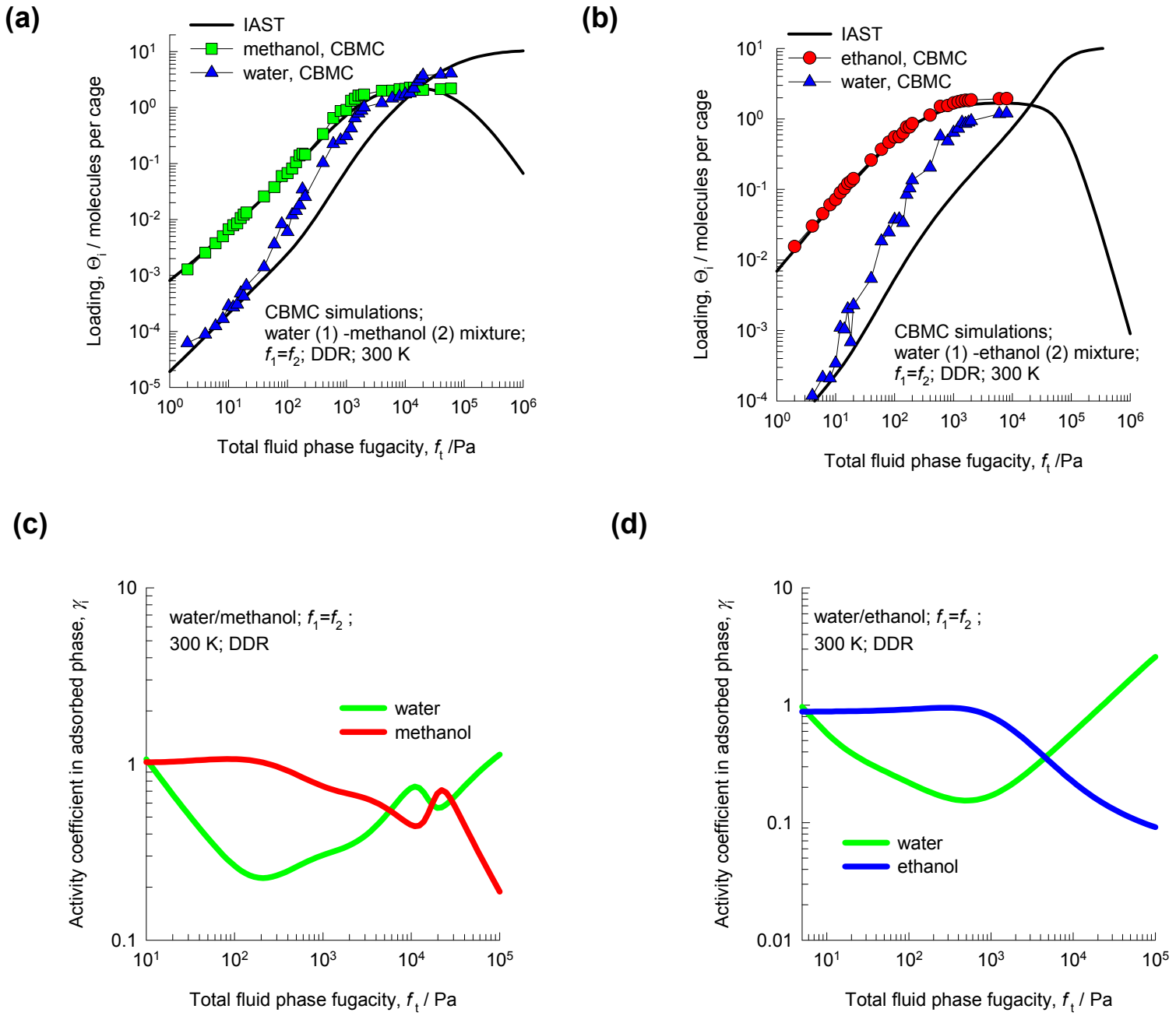

Water, methanol, ethanol isotherms in MFI

Figure S19

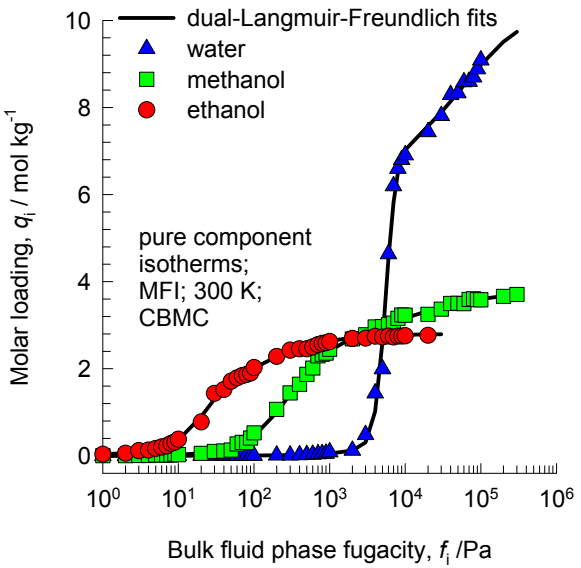

water

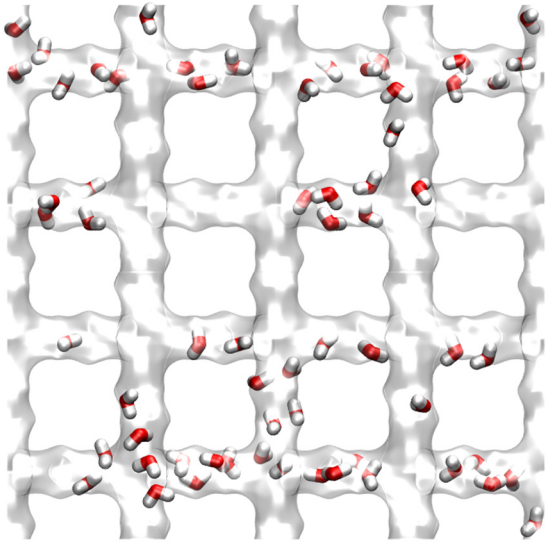

methanol

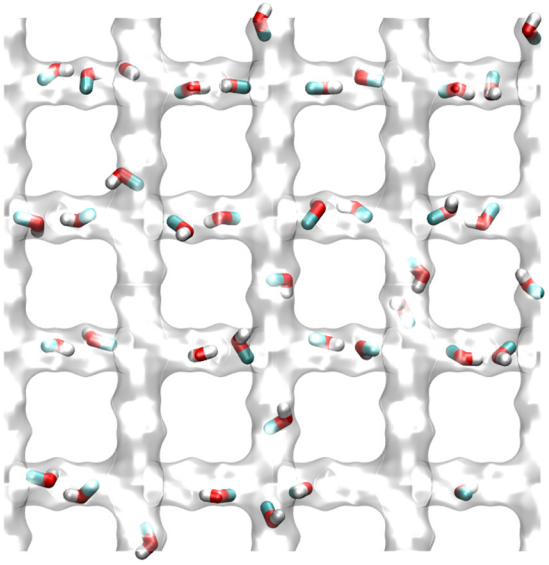

ethanol

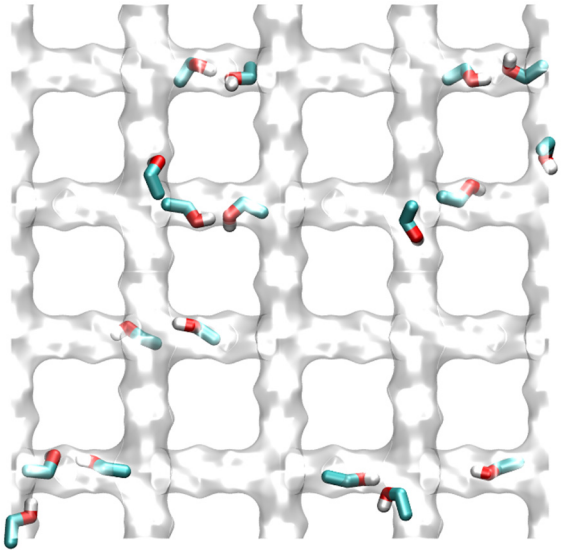

Water/alcohols separations in MFI

Figure S20

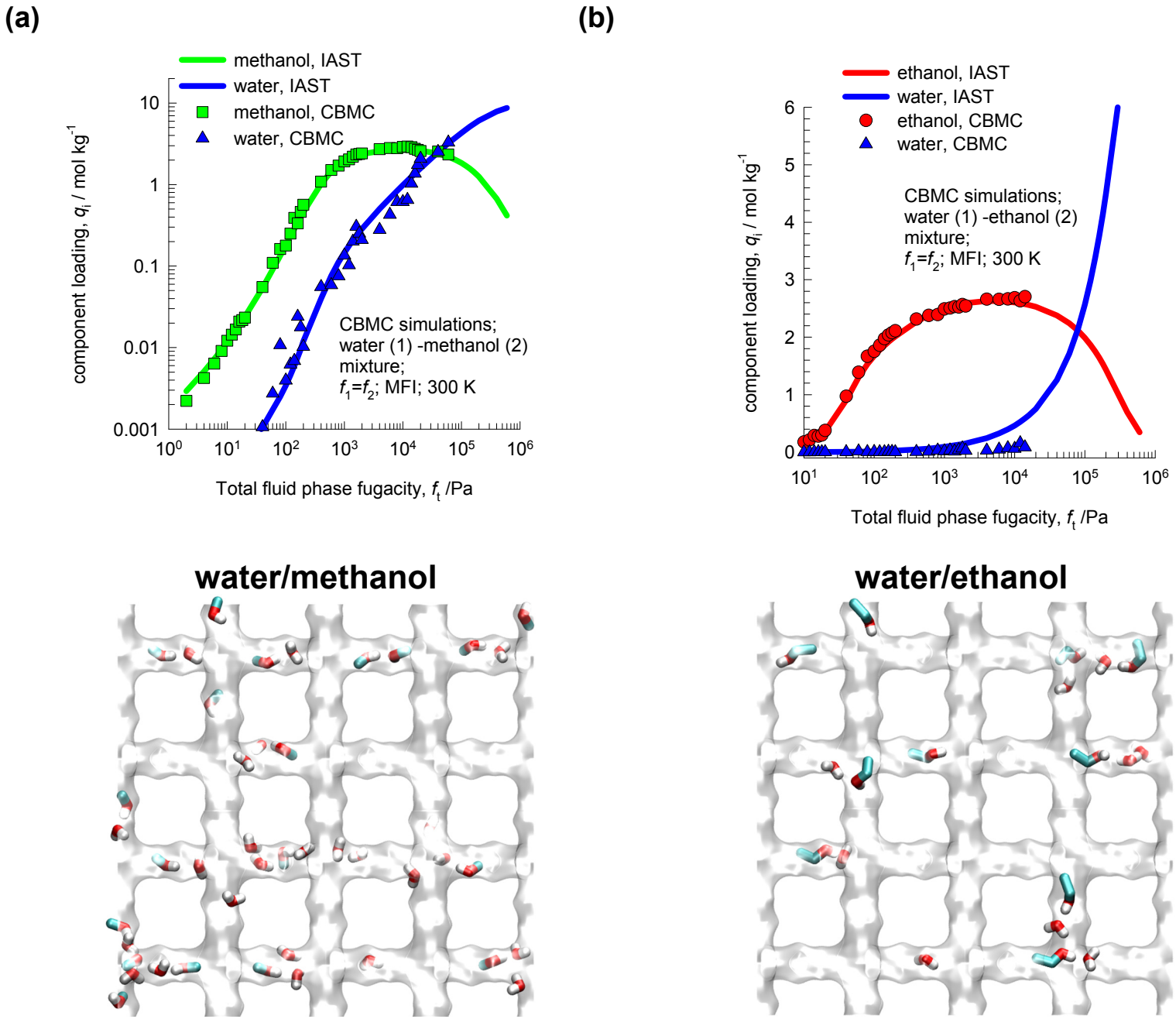

LTA landscape; cation positions

Figure S21

There are 8 cages per unit cell.
The volume of one LTA cage is 743 Å^3, intermediate in size between a single cage of ZIF-8 (1168 Å^3) and of DDR (278 Å^3).

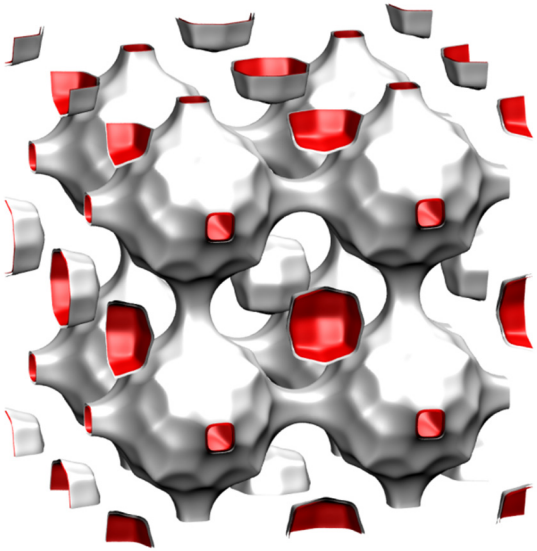

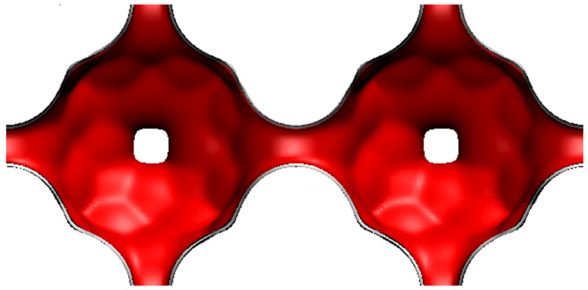

LTA-5A (32 Na^+, 32 Ca^{++})

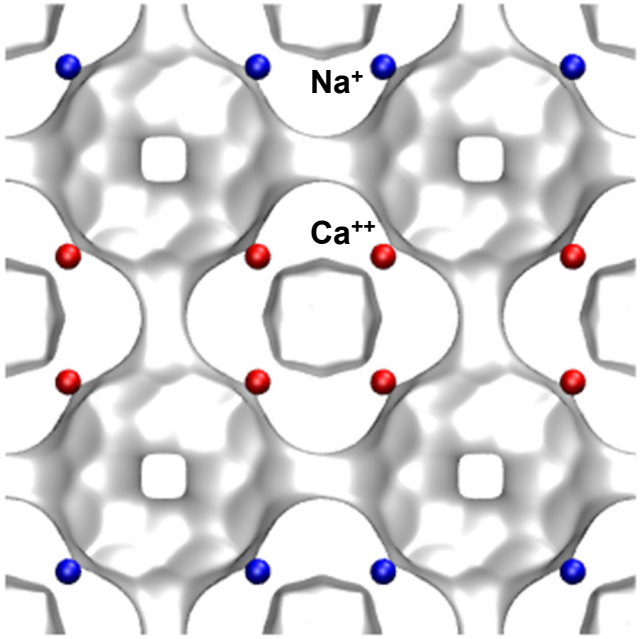

LTA-4A (96 Na^+)

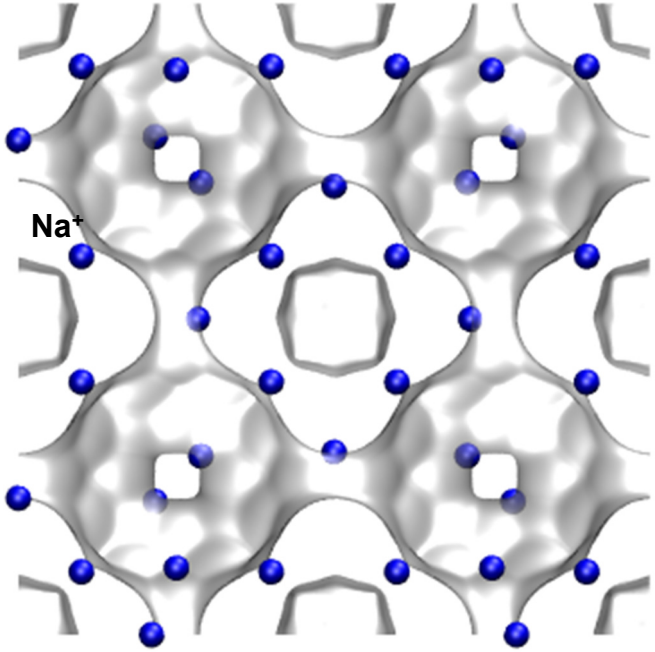

Water, ethanol isotherms in LTA-4A

Figure S22

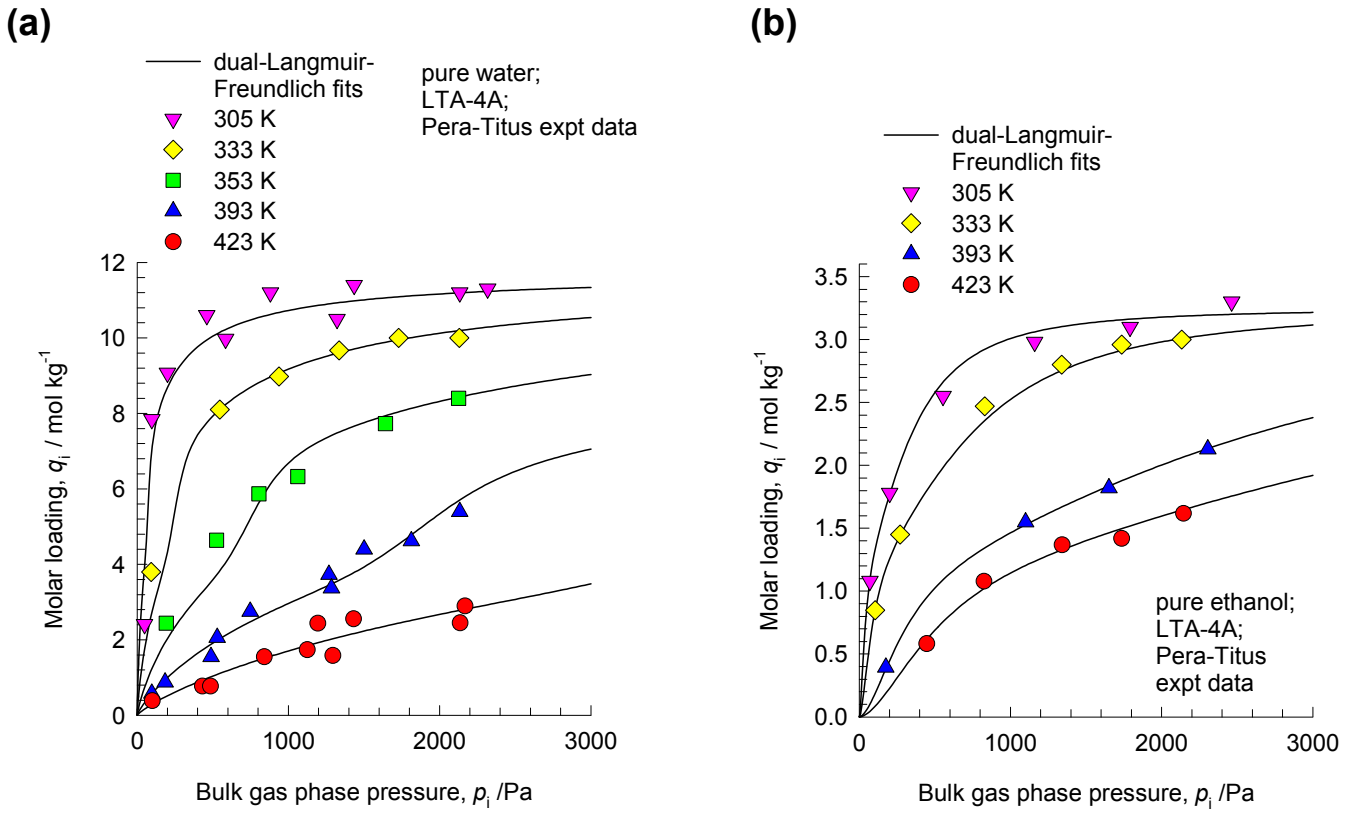

Water/ethanol mixture adsorption in LTA-4A

Figure S23

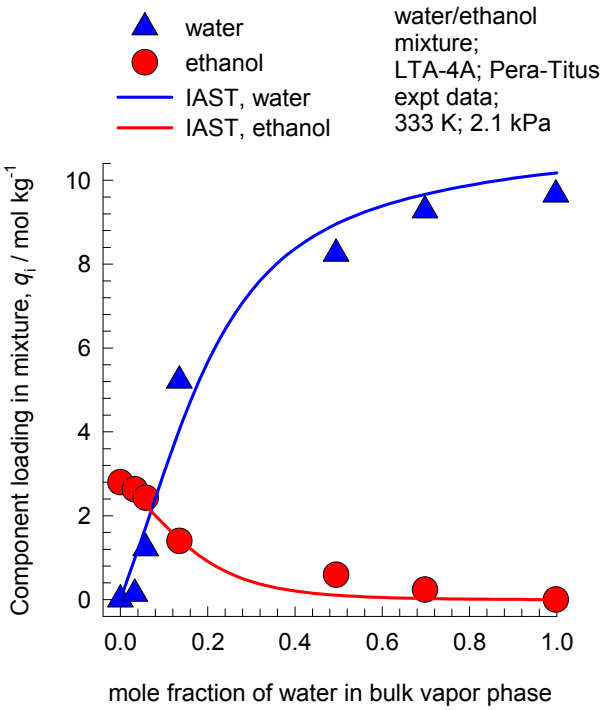

Figure S24

RAST vs CBMC mixture

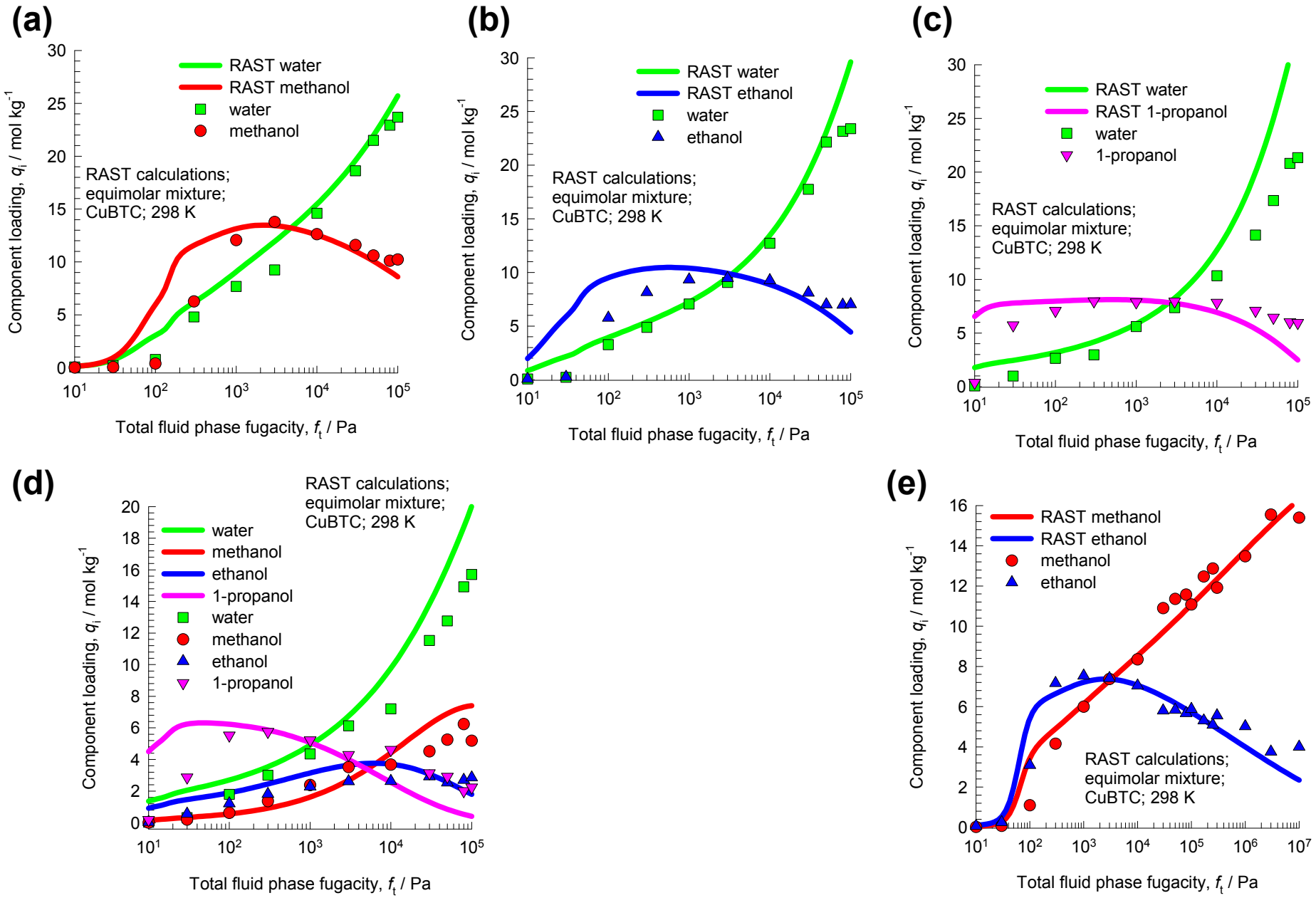

Figure S25

Fractional pore occupancies

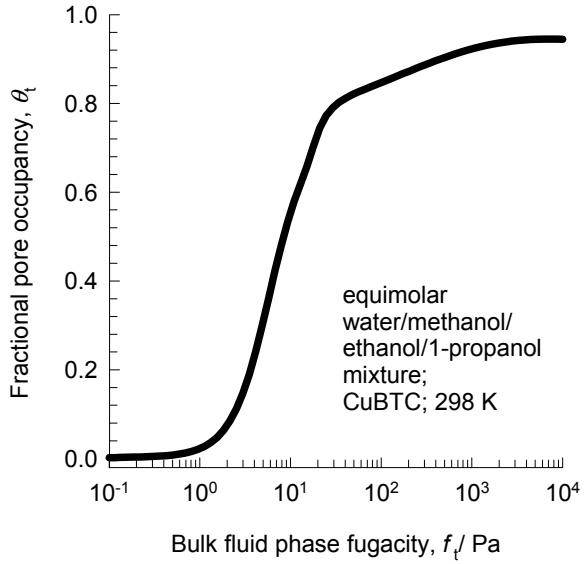

Figure S26

Correction factor for spreading pressure

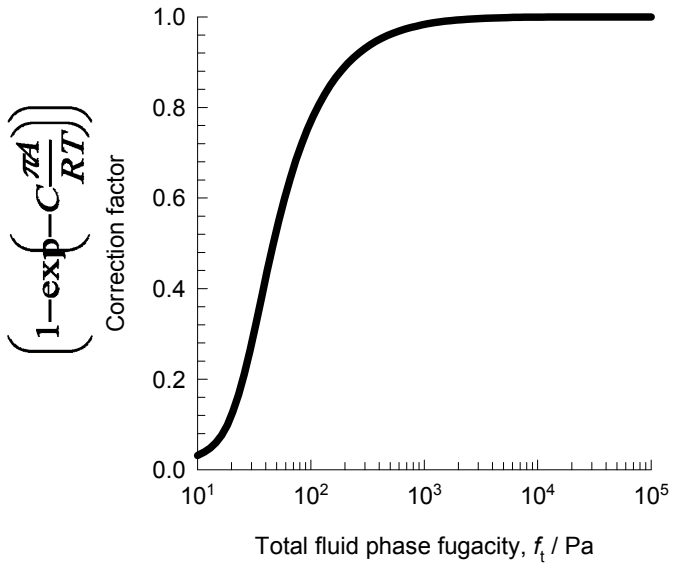

Figure S27

Fixed bed adsorber

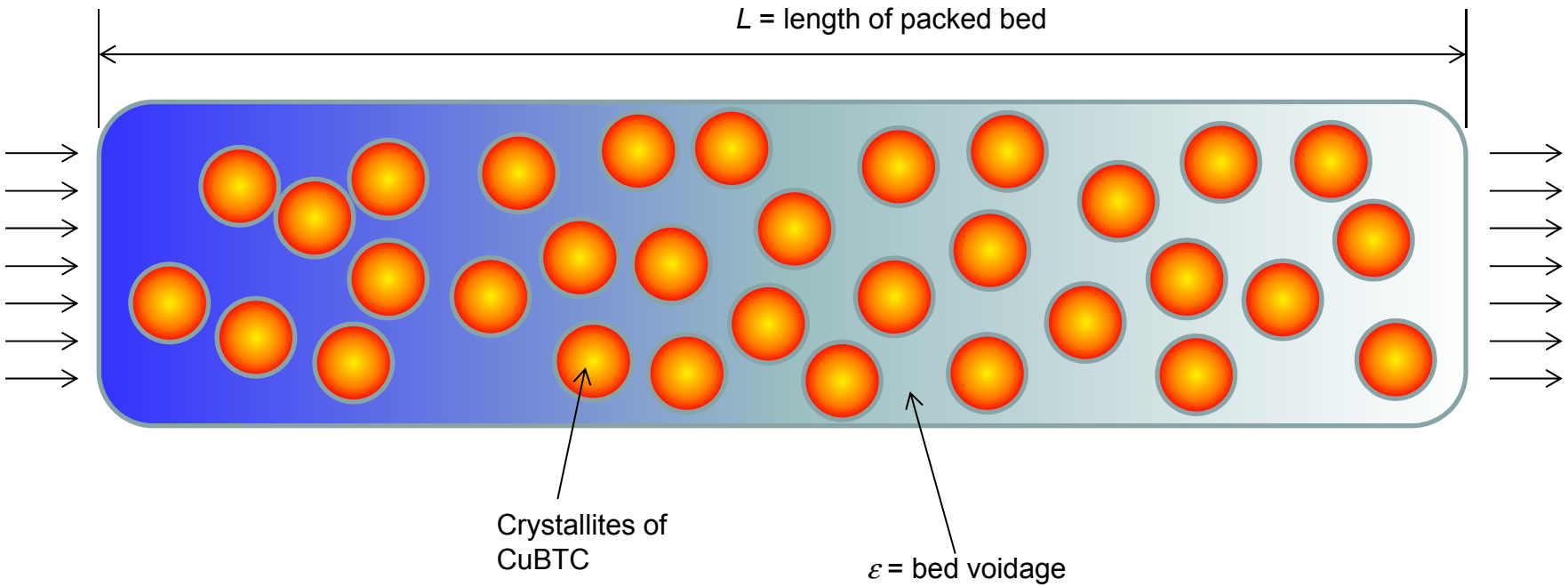

Figure S28

Transient Breakthrough Simulations

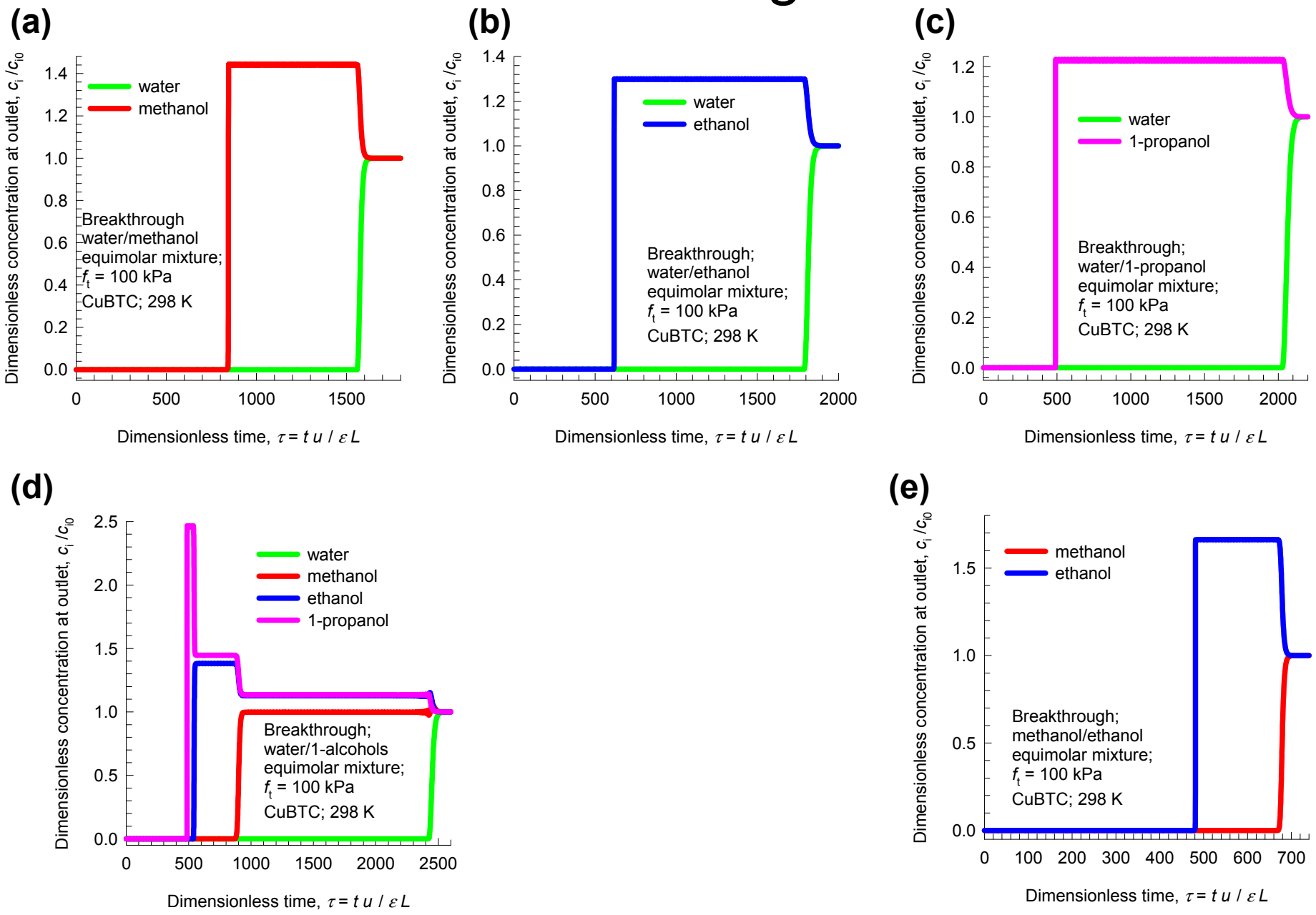

Figure S29

Transient Breakthrough Simulations

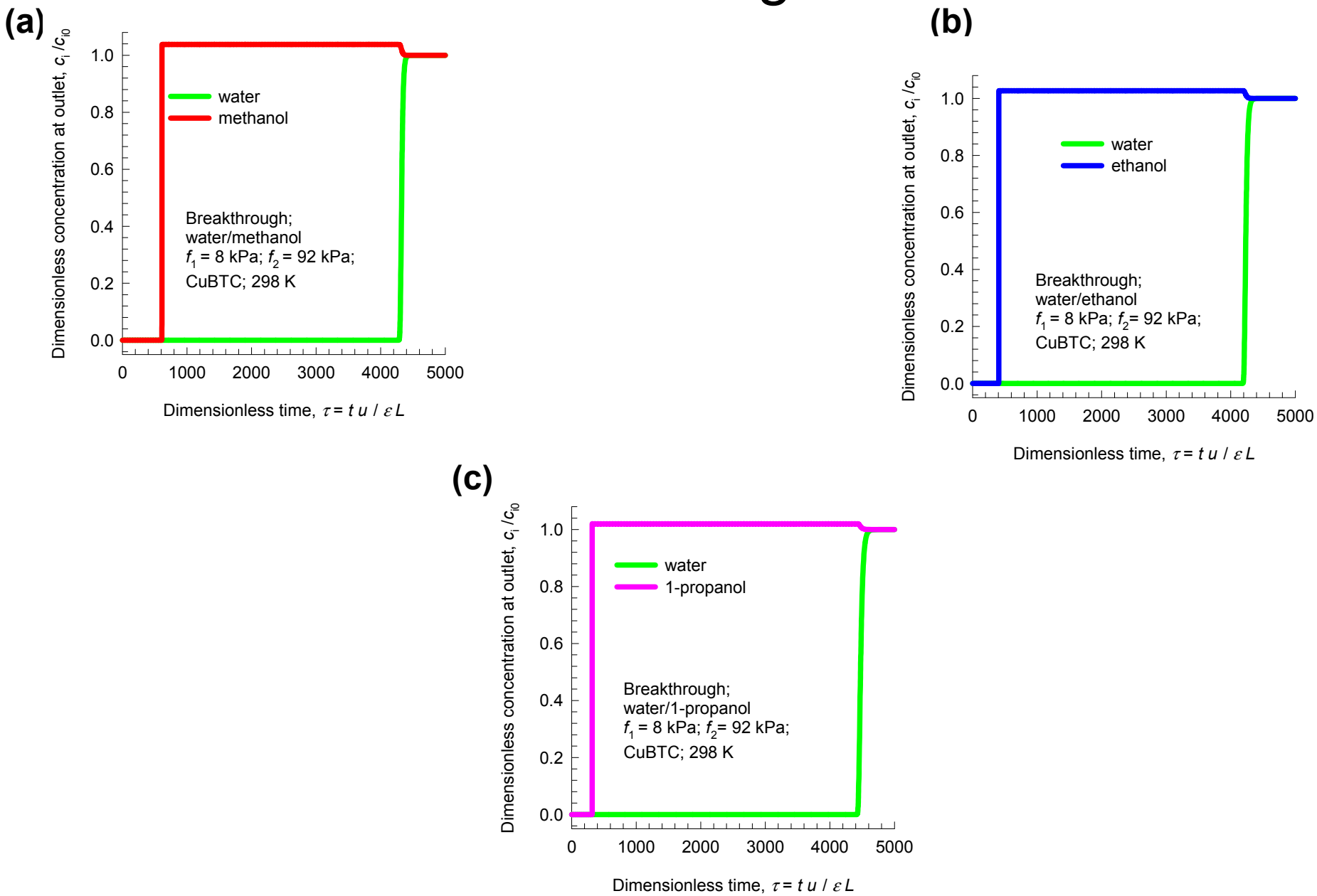

Figure S30

Operations at 1 kPa vs 100 kPa

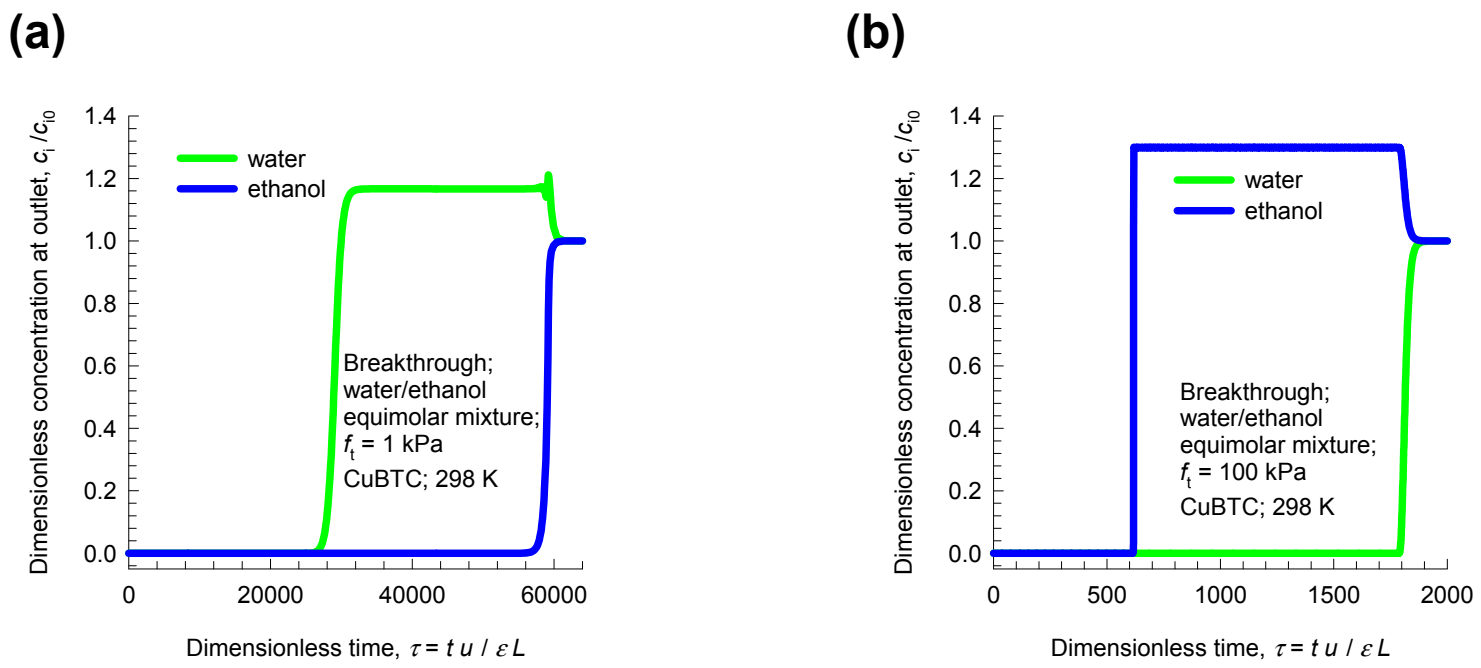

Figure S31

Operations at 1 kPa vs 100 kPa

(a)

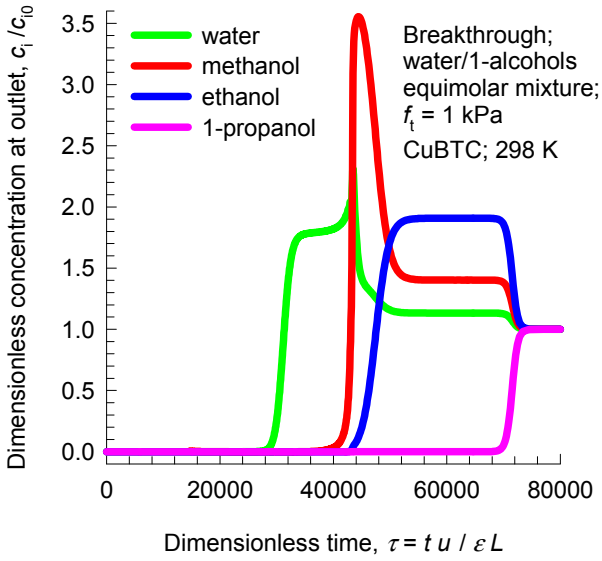

(b)

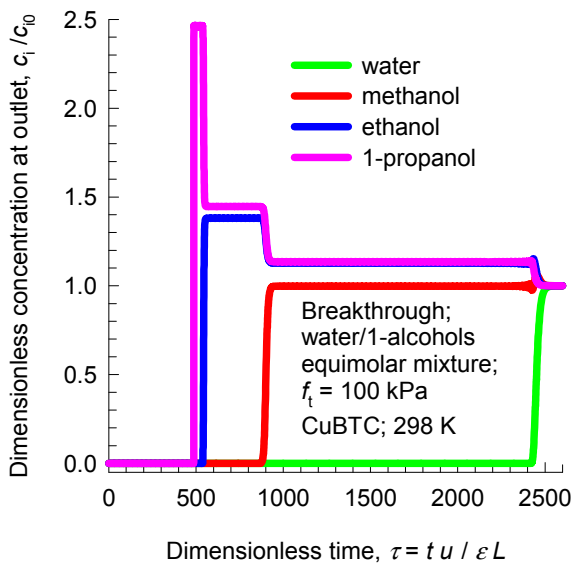

Figure S32

LTA-4A vs CuBTC at 100 kPa